The University of Nottingham

PhD Thesis

One-dimensional Bose gases on an atom chip

Author:
Jorge Ferreras

Principal supervisor:
Prof. Mark Fromhold



Thesis submitted to The University of Nottingham
for the degree of Doctor of Philosophy

in the groups of

Ultracold Atoms Experiments
&
Condensed Matter Theory

School of Physics and Astronomy

June 2018

To my parents

Abstract

Ultracold atomic gases have proven to be an excellent tool for research in quantum systems. A Bose gas can be trapped on an atom chip using very well defined and tunable spatially-dependent potentials. The proximity of the atoms to the chip permits the use of low currents allowing for highly accurate temporal changes.

Excellent experimental apparatus is needed to achieve Bose-Einstein condensation with a sufficient atom number to study low-dimensional physics. The setup described in this document utilises a set of current-carrying structures on top of which an atom chip sits. For improved atom loading rate, a two-dimensional loading stage was added, extending the lifetime of the magnetic trap. From this loading stage to the atom chip, Bose-Einstein condensation of 10^5 Rubidium-87 atoms was achieved in less than 30 s, allowing for a large rate of experimental cycles. The high spatial and temporal tunability of this setup results in the ability to split the atomic cloud and quench the trapping potential geometry.

Maximising the ratio between trapping frequencies for different spatial directions leads to the system presenting features of a one-dimensional gas. Manipulating the coherence dynamics of a one-dimensional Bose-Einstein condensate creates fluctuations in the phase properties of the wavefunction. These fluctuations are observed as atom density perturbations after releasing the trapping potentials, and are a tool for temperature measurements. When the cloud of atoms is positioned at a few tens of micrometres from the surface of the atom chip, corrugations in the microstructures of the chip affect the trapping potentials at very low temperatures $\lesssim 1\,\mu\text{K}$. This effect is simulated and quantified in the thesis, with the aim of improving future setups. Additionally, the effect is explored for microscopy purposes.

The behaviour of a Bose-Einstein condensate, especially the expansion rate, has long been studied. In this thesis, the Gross-Pitaevskii Equation is introduced, finding its numerical solutions to the two-dimensional and three-dimensional forms, using the Split-Step Fourier Method. The results show very good agreement with the experimental results, as well as with other well-established theories of condensates. The creation of such a toolbox opens up the opportunity to further investigate the coherence dynamics of low-dimensional systems.

Acknowledgements

Many people have contributed to this work. I would like to take this opportunity to express my thanks to the following:

- Prof. Mark Fromhold for excellent supervision, giving me the opportunity to work in his group and giving me all the guidance, encouragement and support needed. I have learnt a lot from him, thanks to his passion and dedication. Thank you very much!
- Prof. John Owers-Bradley and Dr. Aidan Arnold for conducting my viva-voce, giving me excellent advice.
- Dr. Lucia Hackermüller for offering me a summer internship and providing help and support ever since.
- Dr. Beatriz Olmos Sánchez, Prof. Igor Lesanovsky, and Dr. Thomas Fernholz for the excellent collaboration and for always being available to help. Prof. Peter Krüger for the opportunity to work in the cold atoms group and all his advice.
- Anton, Gal, Fedja and Tom for the large amount of work made before my arrival and the guidance in the first months in the lab.
- The department's workshops, technicians and administration for an outstanding job keeping the School of Physics at the University of Nottingham running.
- DI. Dr. Christian Koller for being a great physicist, colleague and friend. For all his help and advice, all the discussions in a pub, and teaching me all about cricket. It has been an honour meeting you!
- Asaf for his great approach to life and physics. He guided me in my first steps in the cold atoms labs, and he still is a source of knowledge.
- Dr. Paul Griffin for all his help and advice both with experimental and theoretical physics. Thank you for your career advice.
- Prof. Jan Arlt and Prof. József Fortágh for opening the doors of their labs, and for the advice and discussions.

- All my friends and colleagues from C19 and from the cold atoms labs. It has been a pleasure sharing this time with them all. I want to thank them for all their help and the many invaluable discussions.

- My office colleagues, Nathan Cooper and Nathan Welch, for all the useful discussions and all the English lessons.

- Dom for excellent conversations about aircrafts and tanks! He provides the sanity needed in a physics environment.

- Elisa who is an awesome friend! Her constant help and support has been very important for the completion of this work. She also "voluntarised" to read my thesis and had the patience of giving me advice on it. Her cooking skills have also greatly helped me throughout these years. Thank you!

- Lars always being available for a coffee/beer, with an all-season scarf. I have learnt all about engineering from him, making it almost sound interesting! His determination to learn how to pronounce my name has been very inspirational. He has been a real friend all these years in England, both during my undergraduate and PhD.

- This work would have not been realised without all the good moments, surrounded by the best people one could ever imagine. Fabio, Flavia, Simon, Kostas, Vasiliki, Elena, and all my friends from Aluche (Madrid), thank you very much!

- Finally, I want to thank my parents for the greatest support possible. It is hard to describe how important they have been to me. Their patience and encouragement has been immense. I am deeply indebted to them. ¡Muchas gracias!

Contents

Contents iv

1 Introduction 1

2 Trapping and cooling of neutral atoms 7
2.1 Laser cooling and trapping of neutral atoms . . . 8
2.1.1 Radiation pressure . . . 8
2.1.2 Sub-Doppler cooling and the recoil limit . . . 9
2.1.3 The Magneto-Optical Trap (MOT) . . . 10
2.1.4 U-MOT . . . 11
2.2 Magnetic trap . . . 12
2.2.1 Optical pumping . . . 12
2.2.2 Z-wire trap . . . 13
2.2.3 Evaporative cooling . . . 15
2.3 Bose-Einstein condensation . . . 17
2.3.1 Bose-Einstein distribution . . . 18
2.3.2 Critical temperature . . . 19
2.3.3 Macroscopic wavefunction . . . 21

3 System components development and characterisation 23
3.1 Vacuum system . . . 24
3.1.1 Vacuum components . . . 25
3.1.2 Bakeout procedure . . . 28
3.2 Laser system . . . 29
3.3 Understructure to generate magnetic fields . . . 33
3.4 2D MOT . . . 36
3.4.1 Pressure difference . . . 40
3.4.2 Optics setup . . . 42
3.4.3 Permanent magnets . . . 43
3.5 Magneto-Optical Trap (MOT) . . . 46
3.5.1 Sub-Doppler cooling and compression . . . 49
3.6 Magnetic trap . . . 50
3.6.1 Evaporative cooling . . . 51
3.6.2 Lifetime measurement . . . 56
3.7 Atom chip . . . 57
3.7.1 BEC on the atom chip . . . 59
3.7.2 Trapping frequencies and aspect ratio . . . 61

3.7.3 BEC lifetime in a chip trap . . . 64
3.8 Imaging system . . . 65
3.8.1 Absorption imaging . . . 66
3.8.2 Temperature measurement . . . 70
3.8.3 Resolution focus and magnification . . . 71

4 Low-dimensional Bose gas in an atom chip 73
4.1 Quenching and manipulation of atom clouds in a chip trap . . . 74
4.1.1 Splitting of a cold atom cloud . . . 74
4.1.2 One-dimensional quench . . . 77
4.2 Low-dimensional behaviour of a BEC . . . 79
4.2.1 Phase fluctuations in an elongated 3D BEC . . . 79
4.2.2 Density fluctuations in free expansion of the atom cloud . . . 83
4.3 BEC microscopy and disorder . . . 88

5 Fragmentation of a low-dimensional condensate 91
5.1 Fragmentation of a low-dimensional BEC . . . 92
5.1.1 Formation of sub-clouds in an elongated 3D-BEC . . . 92
5.1.2 Atom chip fabrication . . . 97
5.1.3 Suppression of imperfection effects . . . 98
5.2 Effect of a corrugated current flow . . . 98
5.3 Exploitation of fragmentation for multiple parallel studies . . . 105

6 Expansion of a low-dimensional condensate 108
6.1 Gross-Pitaevskii Equation (GPE) . . . 109
6.1.1 Condensates in anisotropic harmonic potentials . . . 110
6.1.1.1 Weakly interacting regime . . . 111
6.1.1.2 Thomas-Fermi approximation . . . 111
6.2 Split-Step Fourier Method (SSFM) . . . 112
6.3 Expansion of a low-dimensional condensate . . . 117
6.3.1 Expansion speed . . . 117
6.3.2 Aspect ratio . . . 119
6.3.3 Three-dimensional modelling . . . 123

7 Emerging Quantum Technology components 126
7.1 Optimisation of magnetic field generation . . . 127
7.1.1 Battery powered magneto-optical trap . . . 127
7.1.2 Magnetic Induction Tomography (MIT) . . . 129
7.2 Optimisation of the MOT with a dual-colour scheme . . . 131
7.3 Conclusions and Outlook . . . 133

Bibliography 135

Chapter 1

Introduction

In 1924, physicist and Nobel laureate Albert Einstein received a letter from Satyendra Nath Bose deriving quantum radiation without any reference to classical physics. It was describing what are now known as photons. Impressed with this work, he translated it to German and published it in *Zeitschrift für Physik* [1]. Einstein developed these ideas, extending them to matter [2]. Ironically, he did not pursue this any further due to his scepticism about the physical realisation of Bose-Einstein condensation (BEC) [3, 4]. In 1995, Eric Cornell and Carl Wieman, at the NIST-JILA lab, produced the first condensate of an atomic Bose gas, using Rubidium atoms [5]. In the same year, the group of Wolfgang Ketterle, at MIT, achieved the first condensate of sodium atoms [6]. For these achievements, the three of them received the Nobel Prize in Physics in 2001 [7]. This indicates the greatly varying evolution rate of physics, especially quantum physics, and the impossibility of predicting how it will develop. If the great Albert Einstein could not envision the realisation of his own work, where will quantum physics lead us to in the next years?

The study of ultracold atomic physics is a branch of research that is helping greatly to understand the complex world of quantum physics. Its complexity of experimental realisation has fuelled some scepticism amongst physicists ever since the first experiments were built. Nevertheless, it has proven many times to be worthwhile pursuing. Creating ultracold atoms relies on the ability to trap and cool neutral particles, from a room temperature of 300 K to the micro- and nanoKelvin regimes [8]. The versatility of using neutral atoms for the study of quantum physics is immense, and offers a great tool for the realisation and investigation of

quantum models. Systems can be easily tuned by modifying their environment. For example, the application of external magnetic fields modifies the splitting of the atomic energy levels, changing the photon-atom interaction. One of the main uses of this technology has been in the field of interferometry [9–11]. In the same way that light can be used as an interferometer, matter can also be used for interferometry, addressing the phase and spin of the atoms [12].

Laser cooling uses the principle of radiation pressure to cool atoms, in conjunction with the Doppler effect [13, 14]. Additionally, magnetic fields split the energy levels of the atom due to the Zeeman effect [15]. A stable laser source is required to resonantly excite specific atomic transitions. An atom sitting still in a space-dependent magnetic field potential will absorb a photon from a laser beam with circularly polarised light, inducing an atomic transition. Immediately after, a photon will be emitted in a random direction. For a large number of absorption-emission processes, there will be a net force in the direction of the oncoming beam. Using the same procedure in all three coordinates will cause the atoms to be confined and cooled at the minimum of the magnetic field [16, 17]. The Doppler effect states that if the atom is moving, the observed resonance frequency will vary. This makes the trapping and cooling process velocity dependent, meaning that, by tuning the frequency of the photons, slower or faster atoms can be selectively addressed [18, 19]. So far, over thirty different elements and molecules have been successfully cooled down using this technique. Each element has a different energy level scheme, which will result in pros and cons for different experiments. Alkali atoms are the most common elements for ultracold atom experiments. They are easier to manipulate and have a relatively simple atomic level structure [20, 21]. This simplicity in the energy levels results in fewer dark transitions and, therefore, fewer repumping lasers are required to mantain the atoms in the cooling transition. Additionally, the cooling transitions in alkali atoms are typically at frequencies for which lasers are easier to fabricate. The typically repulsive nature of the interactions in alkali atoms leads to more stable clouds of cold atoms. Experiments with Erbium, for example, show the complexity of energy levels of some atoms [22, 23], which makes trapping and cooling harder.

Louis Victor Pierre Raymond de Broglie proposed early in the twentieth century that matter behaves like waves, with its characteristic wavelength inversely proportional to the momentum of the particle [24]. An ensemble of neutral atoms at a temperature T of mass m has an associated *de Broglie* wavelength

$$\lambda_{dB} = \sqrt{\frac{2\pi\hbar^2}{mk_BT}}. \tag{1.1}$$

As the temperature is reduced this wavelength becomes larger. Bose-Einstein condensation can then be achieved, with a macroscopic fraction of the atomic cloud gathered in the ground state of the system.

The experimental setup described in this document was designed and built to reach a Bose-Einstein condensate of Rubidium-87 atoms on a chip. Atom chips are great tools for manipulation of ultracold atomic gases, especially in a condensed state. Their close proximity to the sample means that the currents can be reduced, and therefore the magnetic field potentials can be carefully manipulated, achieving fine control of the system [25]. Micro-fabrication techniques, like the "lift-off proccess" used for the chip in this setup, ensure a level of precision better than any previous technique [26]. In the last few years, additive manufacturing groups have started to show the potential of 3D printing in atom cooling [27, 28]. The presence of a large number of different current-carrying wires on the chip allows for a wide experimental parameter space, from shaping of energy potentials to the application of Radio-Frequency (RF) signals on the atoms for evaporative cooling or dressing of states.

The presence of the atom chip poses also some disadvantages, especially during the first stage of the experimental cycle. An ideal Magneto-Optical Trap (MOT) configuration for laser cooling would be a six-beam configuration with light shone symmetrically onto the central region of the trapping potential. The typical configuration in an atom chip experiment is a mirror-MOT, where there are two counter-propagating beams parallel to the surface of the chip, and another two beams that are shone at an angle on the reflective surface of the chip. The efficiency of this configuration is reduced due to its lower capture volume. Nevertheless, a MOT containing 5×10^8 atoms can be reproducibly obtained in the experiment, and cooled down to a few tens of micro-Kelvin. After this point and due to the Doppler cooling limit, quantum degeneracy can only be achieved using a different technique, called evaporative cooling. In this setup, evaporative cooling is realised by applying a frequency and amplitude-varying RF magnetic signal that will induce a resonance between atomic levels. Carefully controlling this resonance will see the hottest atoms being removed from the trap, leaving only the colder atoms and, therefore, lowering the overall temperature of the sample [29].

The work presented in this thesis is a combination of experimental and theoretical work. The experimental part is a continuation of the work done by previous members of the laboratory, Dr. Gal Aviv [30], Dr. Anton Piccardo-Selg [31], Dr. Fedja Orucevic and Dr. Thomas Barrett [32]. Bose-Einstein condensation on the atom chip was achieved shortly after the start of the work here presented. After the first realisation of a ^{87}Rb BEC in Nottingham, the setup was modified significantly to ensure a stable and reliable performance, with the optical setup re-designed, and a pre-cooling stage added. This pre-cooling stage was designed and assembled as part of a project prior to the start of this thesis work [33]. It greatly improved the lifetime in the evaporative cooling stage, ensuring a reproducible BEC of 10^5 atoms.

This setup allowed the study of dynamics in an elongated BEC. Aspect ratios of up to 120 are easily obtained, with the system presenting characteristics of one-dimensional Bose gases. In this limit, the phase of the system can fluctuate randomly along the weak direction of the BEC, but remains unaltered in the strongly confined radial component [34]. When the system is released from the trapping potential, these fluctuations in the phase result in density modulations. The system interferes with itself. The analysis of this pattern reveals dependence on the time-of-flight and temperature. Additionally, rapid changes on the trapping geometries can infer a "breathing" of the system, characteristic of BECs and presented in this document. With the Bose gas trapped at distances of a few tens of micrometres, a fragmentation can be observed. The reason for this fragmentation is still unknown, although it motivated a theoretical investigation on the role of lithography defects. Nanoscale imperfections on the wires of the chip can alter the electron distribution in the gold wires, modifying the flow of current and, therefore, the trapping potentials at very low temperatures. The effect of the proximity of the cloud to the surface of the chip serves as a proof of the potential of these systems for magnetic microscopy [35].

In order to fully understand the behaviour of BECs, one has to investigate the solutions to the Gross-Pitaevskii Equation (GPE) that defines the macroscopic wavefunction of the system when $T = 0$ [36]. Numerical solutions were found using the Split-Step Fourier Method (SSFM) for both a two-dimensional GPE and a three-dimensional GPE. Comparison with experimental results showed very good agreement, as did when comparing to the well known analytical derivations of Dalfovo et al. [37, 38].

Quantum physics has been revolutionary in the last century, with great contributions to the understanding of it, but it has only been in the last decade that practical applications have started to be considered. This last decade has seen a dramatic shrinking in the size of the setups, with the first experiments leaving the labs [39], and companies selling fully-operational apparatus. The United Kingdom government is investing £270m for the first stage in development of a UK Quantum Technologies program (2014-2019). The University of Nottingham is part of a group of universities that have received this funding. As part of this work, a collaboration was established with the University of Strathclyde, creating the first single-beam grating MOT with 9 V battery powered optimised coils. Optimisation of magnetic field generating structures is one of the key components in this new era of Quantum Technologies, with applications such as Magnetic Induction Tomography (MIT) [40].

The work carried out and presented in this thesis can help with further studies regarding atom-surface interactions, as well as low-dimensional physics. The laboratory is now in a fully functional, stable and reliable operating state. Additionally, the work on the GPE can be used to further understand the quantum behaviour of the atoms, with the potential of exploring other phenomena like solitons [41, 42], vortices or quantum reflection [43]. The outline of the chapters in this thesis is as follows:

Chapter 2 This initial chapter starts with an overview of laser cooling techniques and their limits, followed by the evaporative cooling technique. The magnetic trapping systems used are explained. The final part of this chapter derives the fundamental physics of Bose-Einstein condensation.

Chapter 3 The description of the experimental setup employed, along with the characterisation of it, are presented in this chapter. The experimental method to achieve condensation is explained in detail, describing the improvements made to the setup and characterising the experimental performance.

Chapter 4 In this chapter, the experiments realised in the laboratory are explained and analysed. These include splitting of the cloud, one-dimensional quenching generating "breathing" of the BEC, analysis of the density modulations arising from in-trap phase fluctuations and microscopy in the proximity of surfaces.

Chapter 5 Motivated by the fragmentation observed in the experiment, this chapter attempts to explain the cause of it, simulating the effect that nano-scale current flow corrugations in the chip have on low temperature systems.

Chapter 6 This chapter presents the numerical solutions for the two-dimensional and three-dimensional Gross-Pitaevskii equation, using the Split-Step Fourier Method, comparing it with the experimental results.

Chapter 7 Some additional experiments are presented as a proof-of-principle of the miniaturisation and optimisation of components, and how this will affect the future of Quantum Technologies. An outlook of the ultracold atoms field, in particular suggestions for further work building on that presented in the thesis, is given in the last chapter.

Chapter 2

Trapping and cooling of neutral atoms

In order to achieve the Bose-Einstein condensation of a sample of bosons, the sample must first be trapped and cooled down to hundreds of nano-Kelvin regime. This cooling process can be divided into two main steps, laser cooling in a Magneto-Optical Trap (MOT) and evaporative cooling in a conservative trap.

The first step in this process is the MOT, in which the sample is illuminated by appropriately circularly polarised laser beams, inducing atomic transitions and reaching temperatures of a few tens of micro-Kelvin. After this, the evaporative cooling technique is then used to further cool and reach condensation. This technique consists of removing the hottest atoms from the sample, letting the sample re-thermalise and therefore acquire a lower temperature. It results in temperatures at which Bose-Einstein condensation occurs, and can be experimentally realised in either a magnetic trap or an optical dipole trap [29, 44–46].

The experiment described in this document takes advantage of a mirror-MOT, followed by two stages of evaporative cooling inside a magnetic trap: one using a large magnetic trap structure and a final one generating the magnetic trapping potential using an atom chip.

2.1 Laser cooling and trapping of neutral atoms

Laser cooling and trapping techniques have been around for over three decades now. Several breakthrough developments have happened along the way. In 1997, Steven Chu, Claude Cohen-Tannoudji and William D. Phillips, received the Nobel Prize in Physics for their developments of methods to cool and trap atoms with laser light [47–49].

2.1.1 Radiation pressure

Cooling atoms requires shining laser light with the right frequency. In our case, this frequency is determined by the energy level transition between the $5^2S_{1/2}$ and $5^2P_{3/2}$ energy levels. For Rubidium-87, this transition has a wavelength of 780.244 nm. Photons coming from a laser beam with this wavelength will be absorbed by ^{87}Rb atoms, inducing an excitation of the atom to the $5^2P_{3/2}$ level. The atom will then spontaneously emit a photon with the same frequency, decaying back to the $5^2S_{1/2}$ level.

The force exerted by a laser beam is called radiation pressure. Considering a static atom in a two-level system, with a natural linewidth of Γ, a laser is shone with an angular frequency ω_L that is nearly resonant with the atomic transition frequency ω_A. The atom absorbs photons with momentum $\hbar k$ from this laser beam and emits them spontaneously in random directions, meaning that the force originating from this emission will be in a different random direction for each emission process. Each absorbed photon gives the atom a kick in the direction of the oncoming beam. Averaging over a large number of absorption-emission processes, the net force will push the atom in the direction of the laser beam. The rate of these absorption-emission cycles is defined by the Rabi frequency, Ω. This force saturates to a maximum value of $\hbar k\Gamma/2$ because at high intensities the populations in the two-level atom system are equally distributed between the upper and lower states. It is worth noting that this force is several orders of magnitude higher than the force resulting from gravity. The Doppler effect is then exploited to address moving atoms.

If the atom is travelling at velocity $\mathbf{v}$ towards the laser beam, the frequency of the laser must be shifted such that $\omega_L < \omega_A$. This is referred to as a red detuned

frequency. Due to the Doppler effect, the effective frequency will be resonant with the atomic transition of the atoms travelling towards the laser beam. With a laser intensity I this force will be given by:

$$\mathbf{F} = \hbar k \frac{\Gamma}{2} \frac{I/I_{sat}}{1 + I/I_{sat} + 4\delta^2/\Gamma^2}. \tag{2.1}$$

where the saturation intensity, I_{sat}, is defined as $I/I_{sat} = 2\Omega^2/\Gamma^2$.

When this process is extended to three spatial dimensions, atoms in the system become effectively cooled. This cooling, commonly referred to as Doppler cooling, is the overall result of all the absorption and emission processes. However, during each absorption-emission process, the atom is heated, undergoing a random walk. This effect occurs for each and every emission, independently of the number of processes, resulting in a constant random motion of the atom. Due to this constant motion, there is a theoretical lower temperature limit for Doppler cooling

$$T_D = \frac{\hbar\Gamma}{2k_B} \tag{2.2}$$

which, for ^{87}Rb, corresponds to $T_D = 146\,\mu\text{K}$ [50]. Here, k_B is the Boltzmann constant.

2.1.2 Sub-Doppler cooling and the recoil limit

Experimental realisations with ^{87}Rb have shown that laser cooling is capable of reaching temperatures below the theoretical Doppler cooling limit described in eq. (2.2) [19]. The mechanism behind this effect was later explained in detail by Jean Dalibard [18] and Harold J. Metcalf [16], among others.

The counter-propagating pairs of laser beams, with opposing polarisation with respect to the lab frame (same handedness), generate a polarisation gradient that induces a sinusoidal variation of the hyperfine structure of the atoms in the ground state. By stimulating the cooling transitions when atoms are at their maximum energy configuration in this sinusoidal variation, energy is removed from the sample, effectively cooling down the cloud of atoms to temperatures of the order of tens of micro-Kelvin. The temperature can potentially be further reduced using

this mechanism at the expense of loss of atoms, resulting in a trade-off between the number of atoms and temperature of the cloud. For this mechanism to work, a large frequency detuning of the order of several Γ is needed for a short period of time.

2.1.3 The Magneto-Optical Trap (MOT)

The process previously explained cools the atoms down but is not sufficient to trap atoms. In order to efficiently trap and cool hot atoms, a magnetic field must be introduced.

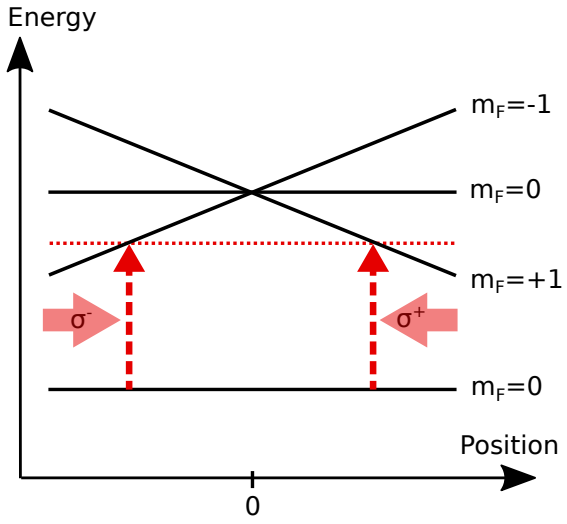


FIGURE 2.1: Energy level scheme for describing laser cooling and trapping. The energy levels of the atom (solid black lines) are separated by applying spatially varying magnetic fields. Clockwise and anti-clockwise circularly polarised light (σ^+ and σ^- with respect to the lab frame) is shone onto the atoms from opposite directions. Atoms absorb photons in a resonant transition (dashed red lines) and re-emit them in a random direction, effectively creating a force in the direction of the travelling laser beam.

The MOT was first proposed by Jean Dalibard in the 1980s, and later realised experimentally with Sodium atoms in the group of David Pritchard [14]. Figure 2.1 shows the energy level scheme of the atoms along the propagation line of one of the laser beams. A linearly varying magnetic field is added, splitting the energy levels of the atoms differently depending on the spatial position. Laser light is shone from both sides of the sample, inducing the required cooling transitions. Since the energy levels are split due to the Zeeman effect, the exact frequency required to illuminate the atoms with, will differ from the resonant frequency

with $m_F = 0$. The higher the magnetic field magnitude, the larger the splitting between the $m_F = 0$, $m_F = -1$ and $m_F = +1$ levels will become. To excite the atoms to one of these $m_F = -1$ or $m_F = +1$ states, it is necessary to shine circularly polarized light, as shown with the horizontal red arrows in fig. 2.1. The σ^+ polarised light excites $\Delta m = +1$ transitions and the σ^- polarised light excites $\Delta m = -1$ transitions.

2.1.4 U-MOT

The are several different ways to create the desired magnetic fields in order to split the atomic levels of the atoms and contribute to the laser trapping and cooling process. Arguably, the simplest and most widely used technique is to create a quadrupole field, where the fields are symmetric around each axis. Typically, this is achieved using two simple coils in anti-Helmholtz configuration. This has disadvantages, especially due to Eddy currents in the larger coils when trapping potentials need to be rapidly modified. Additionally, in the setup described in this thesis, the system was designed to be more compact. For these reasons, the magnetic potentials are created by passing currents through copper structures underneath the atom chip.

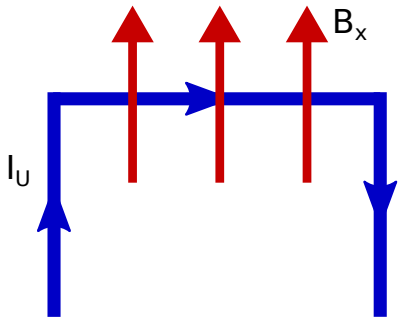


FIGURE 2.2: Diagram of a U shaped conductor structure used for a MOT. The thick blue line indicates the current carrying structure and the direction in which the current travels. The red thin lines indicate the direction of the bias magnetic field. The addition of both fields creates a spatially dependent magnetic potential, with a minimum $|\mathbf{B}| = 0$ above the central region of the U. See [25] for more details.

When a MOT is created in this way, a "U" shaped copper current conductor is implemented. With the aid of an external bias magnetic field, a minimum of magnetic field potential is created above the central region of the U. This is graphically shown in fig. 2.2 and described in detail in [25]. This configuration

allows for a large MOT to be created, compressing the trap and varying its position in time. The bias field is usually created using external coils in a Helmholtz configuration. In the setup described here, the bias field can also be created with the use of a metallic sheet placed underneath the U structure, which produces a homogeneous bias magnetic field above the central trapping region.

2.2 Magnetic trap

Once the atoms are trapped and cooled to their sub-Doppler cooling limit, they are transferred to a pure magnetic trap. Atoms are trapped in the $|F = 2, m_F = +2\rangle$ state, being subjected to a spatially dependent potential energy. This trap is first created by passing currents through the copper structures underneath the atom chip, and then created by passing currents through the gold wires embedded in the atom chip.

The trapping potential is generated by the position dependent shift of the energy levels of the atoms. This is called Zeeman shift and is given by

$$U = \mu_B m_F g_F |\mathbf{B}| \tag{2.3}$$

where μ_B is the Bohr magneton constant and g_F is the g-factor or gyromagnetic ratio. The potential will then be stronger for higher m_F values, and will change sign between positive and negative m_F states.

2.2.1 Optical pumping

For the atom transfer between the MOT and the magnetic trap to be efficient, both the U shaped MOT and the magnetic trap potentials have to be aligned in the same position and have similar energy depth. Additionally, only atoms in the $|F = 2, m_F = +1\rangle$ and $|F = 2, m_F = +2\rangle$ states will be trapped. A technique called optical pumping is then used to transfer all atoms into this $|F = 2, m_F = +2\rangle$ state. A magnetic field to split the $F = 2$ state into its hyperfine structure is applied. Circularly polarised (σ^+ with respect to the lab frame) light induces transitions in which $\Delta m_F = +1$, represented by dashed orange lines in fig. 2.3.

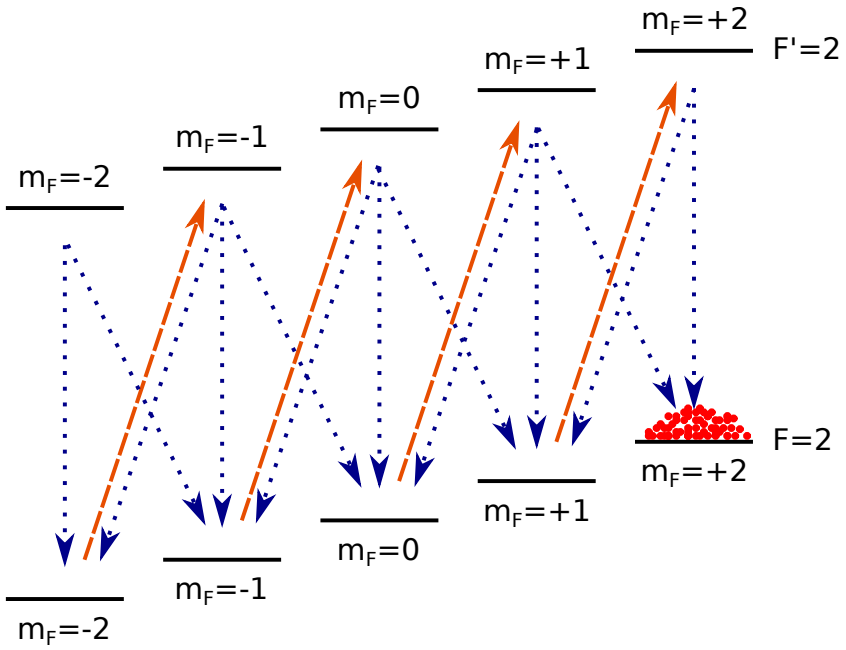


FIGURE 2.3: Optical pumping scheme designed for pumping atoms into a specific hyperfine state. Due to the orientation of the spin of the atom, only atoms in $m_F \geq 1$ states are magnetically trappable. With a magnetic field splitting the hyperfine structure, a circularly polarised (σ^+) laser beam is shone onto the atoms, inducing transitions where $\Delta m_F = +1$, effectively pushing all the atoms into the $|F = 2, m_F = +2\rangle$ state. Orange dashed lines show the absorption processes, and blue dotted lines show the emission processes.

The atoms will spontaneously decay via $\Delta m_F = 0, +1, -1$ transitions, represented by dotted blue lines in fig. 2.3. This process will end with the atoms pumped into the trappable $|F = 2, m_F = +2\rangle$ state.

2.2.2 Z-wire trap

Similar to a MOT, in a magnetic trap a spatially dependent energy potential is needed, with a potential minimum in the centre of the trap. In principle, one could think of a U shaped wire, creating the same energy potential as in the MOT. Unfortunately, when atoms move through a region in which the magnetic field vector rotates, their spin has to follow this rotation. For the relatively large temperatures present in the MOT, atoms are not affected by the minimum of the U shaped trapping well, where the magnetic field equals zero. However, as the temperature is reduced in the magnetic trap, atoms can travel through this magnetic field zero. At this exact point, there is no defined spin of the atoms due to the absence of magnetic field. When the atom returns to a region of finite

magnetic field, it can adopt the opposite spin orientation, resulting in the atom not longer being trappable. This is the so-called Majorana spin flip [51, 52]. The way to avoid this effect, is to ensure that atoms are always subject to a magnetic field potential.

A Z shaped wire [25] can be used in a similar way to the U-MOT presented in the previous section. In addition to the current flowing through the wire, there are two other bias fields. One of them locally cancels out the field produced by the wire (vertical red lines in fig. 2.4), effectively creating the trapping potential in the central region of the structure. The second bias field (horizontal green lines in fig. 2.4), perpendicular to this and parallel to the chip surface, will counteract the effect from the legs of the Z-wire. Modifying the strength of this last field is very useful during the process of evaporative cooling to carefully control the final temperature of the system by tuning the trap depth. Similarly to the U-MOT, the external bias magnetic fields in the Z-wire trap are usually generated using coils in Helmholtz configuration. In an atom chip, these coils can be replaced by other wires to produce a BEC, thus greatly reducing power consumption, and being a unique feature of this experimental setup, explained in detail in section 5.1.1.

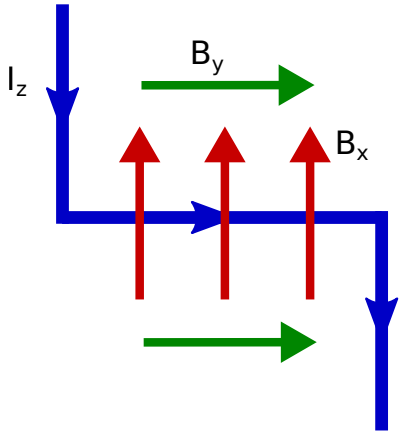


FIGURE 2.4: Diagram of a Z shaped conductor structure used for a magnetic trap. The thick blue line indicates the current carrying structure and the direction in which the current travels. The vertical red lines indicate the direction of the main bias magnetic field B_x. The addition of both fields creates a spatially dependent magnetic potential, with a minimum $|\mathbf{B}| > 0$ above the central region of the Z wire. The additional bias field B_y, represented by horizontal green lines, counteracts the effect of the (upper and lower) legs of the Z-wire, controlling the height of the trap bottom. This configuration eliminates losses due to the Majorana spin flips occuring when an atom travels through a region of zero magnetic field.

The magnetic fields generated from this configuration will be further investigated in chapter 5, where the magnetic trapping potentials are simulated and analysed in detail.

2.2.3 Evaporative cooling

After achieving sub-Doppler cooling in a magneto-optical trap, atoms are further cooled using a different technique. This technique, called evaporative cooling, will see the hottest atoms selectively removed from the trap, leaving only the colder ones, effectively reducing the overall temperature of the sample. This technique can be achieved in an optical dipole trap [46] or in a magnetic trap [51]. The latter is the technique used in the experiment described in this thesis. Radio-Frequency (RF) signals can be used to drive transitions between the m_F levels of the atoms. Optical dipole traps are often used in experiments where the tuning of external magnetic fields is necessary for other reasons, such as Feshbach resonances. Evaporative cooling was first proposed by the group of Prof. Kleppner [44, 45] in 1986, for cooling polarised hydrogen. It was a key step towards achieving Bose-Einstein condensation in alkali metals a decade later.

The ultimate purpose of evaporative cooling is to achieve the reduction in temperature faster than the loss of atoms. The efficiency of evaporative cooling relies entirely on the ratio between elastic and inelastic collisions in the system. For it to be an effective cooling tool, 'good' elastic collisions must be predominant over 'bad' inelastic collisions by a factor of ≈ 150 [53]. Inelastic collisions occur when two atoms collide with each other and induce a change in the internal state of the atoms, such as a change of spin or change in the hyperfine structure. Inelastic collisions often result in atoms being expelled from the trap. On the other hand, elastic collisions result in an exchange of kinetic energy, but do not infer a change in the internal state of the atoms. Such collisions are responsible for the re-thermalisation process, which happens when the hottest atoms have left the trap. The re-thermalisation speed will determine the efficiency of the whole evaporative cooling process.

Consider an atom with energy E, which is part of an atom cloud of temperature T, inside a harmonic potential of depth U. The energy required for this atom to leave the trap is given by

$$E_{ev} = (\eta + \kappa) k_B T, \tag{2.4}$$

where $0 \leq \kappa \leq 1$ determines the fraction of energy that is carried away by the atom and η is the truncation parameter, given by

$$\eta = \frac{U}{k_B T}. \tag{2.5}$$

The energy reduction due to an atom leaving the trap is given by [54]

$$\left(\frac{\mathrm{d}E}{\mathrm{d}t}\right)_{ev} = \left(\frac{\mathrm{d}N}{\mathrm{d}t}\right)_{ev} (\eta + \kappa) k_B T, \tag{2.6}$$

where N is the total number of atoms. The loss of atoms during evaporation is found to be [55]

$$\left(\frac{\mathrm{d}N}{\mathrm{d}t}\right)_{ev} = -n_0 \sigma \overline{v} e^{-\eta} N, \tag{2.7}$$

with $\overline{v} = \sqrt{8 k_B T / \pi m}$ being the thermal velocity, n_0 the density and σ the atom-atom scattering cross-section.

The total variation of energy during the evaporation process is

$$\left(\frac{\mathrm{d}E}{\mathrm{d}t}\right)_{ev} = 3 \left(\frac{\mathrm{d}N}{\mathrm{d}t}\right)_{ev} k_B T + 3 \left(\frac{\mathrm{d}T}{\mathrm{d}t}\right)_{ev} k_B N. \tag{2.8}$$

This, together with eq. (2.6), leads to

$$\frac{\left(\frac{\mathrm{d}T}{\mathrm{d}t}\right)}{T} = \frac{1}{3}(\eta + \kappa - 3) \frac{\left(\frac{\mathrm{d}N}{\mathrm{d}t}\right)}{N}. \tag{2.9}$$

Quantum degeneracy in a three-dimensional harmonic oscillator occurs when the Phase-Space Density (PSD), which is the number of atoms in a volume of size λ_{dB}^3, reaches a value of 1.202 [56]. The de Broglie wavelength, λ_{dB}, is given by

$$\lambda_{dB} = \sqrt{\frac{2\pi\hbar^2}{m k_B T}}, \tag{2.10}$$

where T is the temperature of the sample, and m is the mass of the atom.

The evolution from an initial PSD_i to a final PSD_f is given by

$$\frac{\mathrm{PSD}_f}{\mathrm{PSD}_i} = \left(\frac{N_f}{N_i}\right)^{1-3\alpha}, \tag{2.11}$$

where N_i and N_f are the initial and final number of atoms, and $\alpha = (\eta + \kappa - 3)/3$.

Following this derivation, it can be concluded that the larger the truncation parameter, η, is, the more efficient the evaporative cooling will be. The lifetime of the vacuum will also affect this truncation parameter. A new system (section 3.4) was implemented in order to reduce the collisions of the atoms with the background gas. Experimentally, it was found that the optimum value for the truncation parameter is $\eta = 7$ (section 3.6.1) for the experiment described here. Keeping this truncation parameter constant throughout the whole process is important in order to maintain a predominant ratio of elastic collisions over inelastic collisions.

2.3 Bose-Einstein condensation

In 2001, Eric A. Cornell, Wolfgang Ketterle and Carl E. Wieman received the Nobel Prize in Physics for the achievement of Bose-Eintein condensation in dilute gases of alkali atoms, and for early fundamental studies of the properties of the condensates [57, 58].

Bose-Einstein condensation occurs when a large number of particles occupy the ground state of a sample of integer spin atoms, i.e. bosons. The wavefunctions of the atoms overlap when the de Broglie wavelength λ_{dB} is comparable to the inter-atomic distance, $\lambda_{dB} = n^{-1/3}$, and the atoms are then described by a single wavefunction. The quantum properties of a condensate differ from those of a classical gas.

From eq. (2.10), the temperature at which condensation occurs is

$$T_C = \frac{2\pi\hbar^2 n^{2/3}}{m k_B}. \tag{2.12}$$

This is true as long as there are no other size or shape constraints in the system. The exact details depend on the potential [56].

2.3.1 Bose-Einstein distribution

Consider a Bose gas of identical particles, confined in a harmonic oscillator potential, V_{ext}, at a temperature T. In three-dimensions, this harmonic trap is of the form

$$V_{ext}(\mathbf{r}) = \frac{1}{2}m\left(\omega_x^2 x^2 + \omega_y^2 y^2 + \omega_z^2 z^2\right). \tag{2.13}$$

The quantum energy levels of the system can be written as

$$E_{n_x,n_y,n_z} = \left(n_x + \frac{1}{2}\right)\hbar\omega_x + \left(n_y + \frac{1}{2}\right)\hbar\omega_y + \left(n_z + \frac{1}{2}\right)\hbar\omega_z, \tag{2.14}$$

where n_x, n_y and n_z are the quantum numbers corresponding to the motion of the particles in the three-dimensions. These quantum numbers are integer values greater than or equal to zero.

The average number of particles in a certain energy state (n_x, n_y, n_z) is given by the Bose-Einstein distribution,

$$f(E_{n_x,n_y,n_z}) = \frac{1}{e^{\beta(E_{n_x,n_y,n_z}-\mu)} - 1}, \tag{2.15}$$

where $\beta = 1/k_B T$, E_{n_x,n_y,n_z} is the energy of the state, and μ is the chemical potential. Additionally, the total number of particles must be equal to the sum of the average number of particles in each state, i.e.

$$N = \sum_{n_x,n_y,n_z} \frac{1}{e^{\beta(E_{n_x,n_y,n_z}-\mu)} - 1}. \tag{2.16}$$

For high temperatures, the chemical potential tends to very negative values. When lowering the temperature, while keeping the number of atoms constant, the chemical potential tends to $E_{0,0,0}$. In this case, it is convenient to split the total number of atoms as follows

$$N = N_0 + \sum_{n_x,n_y,n_z \neq 0} \frac{1}{e^{\beta(E_{n_x,n_y,n_z}-\mu)} - 1}. \tag{2.17}$$

In the thermodynamic limit, the large size of the system means that the excitation energy $k_B T$ is much larger than the separation between two consecutive energy levels. This allows replacing the summation for an integral,

$$N = N_0 + \int_0^\infty \frac{\mathrm{d}n_x \mathrm{d}n_y \mathrm{d}n_z}{e^{\beta(E_{n_x,n_y,n_z}-\mu)} - 1}. \tag{2.18}$$

This integral converges to a finite value, meaning that the excited states will be saturated and, therefore, there will be a macroscopic occupation of the ground state of the system, forming a Bose-Einstein condensate.

2.3.2 Critical temperature

At high temperatures, the atoms populate the excited energy levels. This means that $N_0 \ll N$, and the chemical potential takes negative values much larger than the energy of the ground state, $\mu \ll E_0$. As the temperature lowers, the chemical potential approaches the value of E_0. condensation occurs at a critical temperature T_C, when particles macroscopically occupy the ground state. This is the result of the chemical potential being equal to the value of the energy in the ground state. As the temperature goes below T_C, the chemical potential stays constant at that value. The ground state of the system will not have any restriction on the number of bosonic particles it can take, unlike in the case of a Fermi gas.

The critical temperature is the lowest temperature at which the total number of particles is equal to the number of particles in the excited states. Knowing that

$$\mathrm{d}N = D(E)\mathrm{d}E, \tag{2.19}$$

where $D(E)$ is the density of states, and assuming $E_0 = \mu = 0$, eq. (2.18) can be rewritten as

$$N = \int_0^\infty \frac{D(E)}{e^{\beta E} - 1} \mathrm{d}E, \tag{2.20}$$

where $\beta = 1/k_B T_C$. For a large system, the zero-point energy, when $n_x = n_y = n_z = 0$, can be ignored and n_i expressed as a continuous variable. Additionally, the number of quantum states will be large enough so that the total energy E of the system may be also expressed as a continuous variable. This total energy can be linked to a coordinate system and defined by $E_i = \hbar\omega_i n_i$, for the energy in each dimension. In such a system, the number of states with energy less than E is given by

$$N(E) = \frac{1}{\hbar^3\omega_x\omega_y\omega_z}\int_0^E \int_0^{E-E_x} \int_0^{E-E_x-E_y} \mathrm{d}E_z \mathrm{d}E_y \mathrm{d}E_x. \tag{2.21}$$

Integrating eq. (2.21) gives

$$N(E) = \frac{E^3}{6\hbar^3\omega_x\omega_y\omega_z}. \tag{2.22}$$

From eq. (2.19), the density of states can be obtained from the derivative of eq. (2.21)

$$D(E) = \frac{E^2}{2\hbar^3\omega_x\omega_y\omega_z}. \tag{2.23}$$

Substituting this result in eq. (2.20), the number of particles is then given by

$$N = \frac{1}{2\hbar^3\omega_x\omega_y\omega_z}\int_0^\infty \frac{E^2}{e^{\beta E}-1}\mathrm{d}E. \tag{2.24}$$

Using $x = \frac{E}{k_B T_C}$, eq. (2.24) can be rewritten as

$$N = \frac{1}{2\hbar^3\omega_x\omega_y\omega_z}(k_B T_C)^\alpha \int_0^\infty \frac{x^{\alpha-1}}{e^x-1}\mathrm{d}x, \tag{2.25}$$

where $\alpha = 3$ for the three-dimensional harmonic oscillator case. The integral can then be solved using the general result [59]

$$\int_0^\infty \frac{x^{\alpha-1}}{e^x-1}\mathrm{d}x = \Gamma(\alpha)\zeta(\alpha), \tag{2.26}$$

with $\Gamma(\alpha)$ being the Gamma function and $\zeta(\alpha)$ the Riemann zeta function.

In the case of the three-dimensional harmonic oscillator, $\alpha = 3$, $\Gamma(\alpha) = 2$ and $\zeta(\alpha) \approx 1.202$, resulting in a critical temperature of

$$T_C = 0.94 \frac{\hbar}{k_B} \overline{\omega} N^{1/3}, \tag{2.27}$$

where $\overline{\omega} = (\omega_x \omega_y \omega_z)^{1/3}$.

For quick reference, eq. (2.27) can be approximated to

$$T_C \approx 0.045 \frac{\overline{\omega}}{2\pi} N^{1/3} \text{nK}. \tag{2.28}$$

This, for the experiment described later in this document, gives a condensation temperature of the order of a few hundred nano-Kelvin, which is in perfect agreement with the experimental results.

Knowing the critical temperature, the condensation fraction can then be extracted using eq. (2.17),

$$\frac{N_0}{N} = 1 - \left(\frac{T}{T_C} \right)^3. \tag{2.29}$$

2.3.3 Macroscopic wavefunction

The wavefunction of a system without interactions composed of N particles is given by the product of its individual single-particle wavefunctions,

$$\Psi(\mathbf{r}_1, ..., \mathbf{r}_N) = \prod_{i=1}^{N} \psi(\mathbf{r}_i), \tag{2.30}$$

and the wavefunction of a particle in its ground state is given by

$$\psi_i(\mathbf{r}) = \left(\frac{m\overline{\omega}}{\pi\hbar} \right)^{3/4} e^{-\frac{m}{2\hbar}(\omega_x x^2 + \omega_y y^2 + \omega_z z^2)}. \tag{2.31}$$

The spatial density is $N|\psi_0(\mathbf{r})|^2$. For a pure condensate, at $T = 0$, the number of atoms will only alter the height of this distribution, but not its width.

For temperatures $0 < T < T_C$, there will be two distinct distributions, with a condensed fraction appearing in the central peak. This is often used as a tool to confirm the formation of a Bose-Einstein condensate in an experiment, and has been used since the very first observations of BEC [5].

So far, the phenomena of condensation has been described assuming no interatomic interactions were present. This is not the case in a real condensate and, although often weak, interactions are not negligible. Interactions play a very important role in the stability of condensates, and can be attractive or repulsive. The Hamiltonian has to be changed to accommodate the effect of the interactions. This is addressed in detail in chapter 6, where a BEC system with interactions is described using the Gross-Pitaevskii Equation (GPE) [36], and numerical solutions developed.

So far, the chemical potential has been described as a negative quantity that tends to zero as the temperature drops below the critical temperature [60]. The inclusion of interactions in the description of the system leads to a positive value of the chemical potential, raising the effective potential that the thermal atoms experience [61].

Chapter 3

System components development and characterisation

The production of a Bose-Einstein condensate (BEC) requires a complex experimental setup placed in a controlled environment. The laboratory comprises a large room with controlled humidity and temperature conditions, and a control room adjacent to it, from which the experiment is run. The experimental apparatus is controlled via a National Instruments PXIe-1065 with a PXIe-8130 controller, feeding four PXI-6733 analogue output cards. These components are run using Python-based software developed by Dr. Matthew Jones and Dr. Asaf Paris-Mandoki [62, 63]. The camera is controlled with a Matlab script developed specifically for this experiment.

A cold atoms setup requires three main aspects to be addressed: vacuum, optics, and magnetic fields. These are described in detail in the first three sections of this chapter. The vacuum system is explained first, giving a brief description of the components of it, and summarising the procedure followed in order to achieve the required Ultra-High Vacuum (UHV) with a pressure of $< 10^{-9}$ mbar needed for a BEC. The cooling and trapping of the atoms is achieved with the use of laser light. The associated optical bench setup and the cooling and repumping transitions are described in this chapter. The energy levels of the atoms are addressed by the implementation of magnetic confinement potentials, which are produced by an understructure and an atom chip, together with external coils creating homogeneous magnetic bias fields.

The rest of the chapter focusses on the description of the procedure required to reach BEC, showing the performance of the setup. The addition of a pre-cooling 2D MOT stage is explained in detail, showing the advantages of the implementation of such a system in an atom chip experiment.

A functioning cold atom experiment was already present at the start of the work described in this thesis. However, several changes were made to the setup in order to improve its reliability and performance. The author was responsible for the addition of a 2D MOT (section 3.4), the implementation of a new imaging system (section 3.8), and the measurements that characterise the performance of the experiment (sections 3.5 to 3.8). At the same time, the author participated in improving the vacuum system (section 3.1), preparing and mounting the atom chip (section 3.7), and modifying the optics setup (section 3.2).

3.1 Vacuum system

One of the key components of a cold atoms experiment is the vacuum system. UHV is vital in order to perform such experiments. Typically, a Magneto-Optical Trap (MOT) type of experiment can only be performed with a pressure below $\approx 1 \times 10^{-6}$ mbar. The MOT is very robust in this aspect, although much lower pressures are required to perform experiments in the quantum degeneracy regime. When the cloud is transferred to a magnetic trap, the background collisions have a greater effect on the lifetime of the trap, resulting in larger losses as the pressure increases. The nature of the experiment will determine the vacuum needs. For example, a simple experiment performed at temperatures of tens of µK, can work at pressures as high as $\approx 1 \times 10^{-9}$ mbar. On the other hand, experiments that require lower temperatures, or even condensation, have to be performed in pressures lower than $\approx 1 \times 10^{-9}$ mbar (depending on the collision rate) in order to increase the lifetime of the atoms in the trap, as required to implement the evaporative cooling technique.

For the experiment described in this document, the pressure in the main chamber is $\approx 1 \times 10^{-11}$ mbar, making condensation of ^{87}Rb possible. In a MOT stage of a cold atoms experiment, the aim is to collect the largest possible number of trappable particles, whilst maintaining the lowest number of non-trappable particles in the background. This means having a good UHV system with a fully functioning ion

pump working constantly and having alkali dispensers running at relatively high currents. In the magnetic trap stage, the aim is to have the lowest possible number of particles in the background, including trappable particles. The reason for this is that since atoms can only be captured in the MOT stage, any non-captured atoms present in the background will produce background collisions and result in loss of atoms from the magnetic trap. At this stage, a balance between achieving a good level of UHV and a large enough number of ^{87}Rb atoms in the MOT is essential.

The way ^{87}Rb is outgassed into the experimental chamber is by passing some current through what is called a "dispenser". A dispenser is a metal rod covered by a coat of the desired alkali element. On top of it, a sealant cover is also applied to avoid oxidation of the alkali when in contact with air, before placing it in UHV. Once the dispensers are mounted in the vacuum, and UHV achieved, a large current is passed temporarily to break this seal, which will then be absorbed by the ion pump. After this procedure, ^{87}Rb will be outgassed in a larger or lower quantity, depending on the current applied. Too little current will not heat up the rod enough for the Rubidium to evaporate. Too much current and the dispenser can break. Usually the dispensers are run at constant current all day long. In some experiments, like the one described here, it is common practice to run the dispensers pulsed, having them on at larger currents than usual during the MOT stage to achieve a large capture ratio, and off during the magnetic trap to reduce background collisions. Unfortunately, this practice poses a high risk to the dispensers, since the current during the MOT stage has to be larger than usual to compensate for the time they are off during the magnetic trap stage. A broken dispenser no longer functions and can also cause extensive damage to other vacuum components, such as the atom chip, which can result in a need for replacement. This is one of the reasons why a 2D MOT system was implemented in this setup, as explained in detail later in this chapter.

3.1.1 Vacuum components

The main vacuum components of the setup described in this document are shown in fig. 3.1. The functionality of each of them and the pumping procedure is as follows:

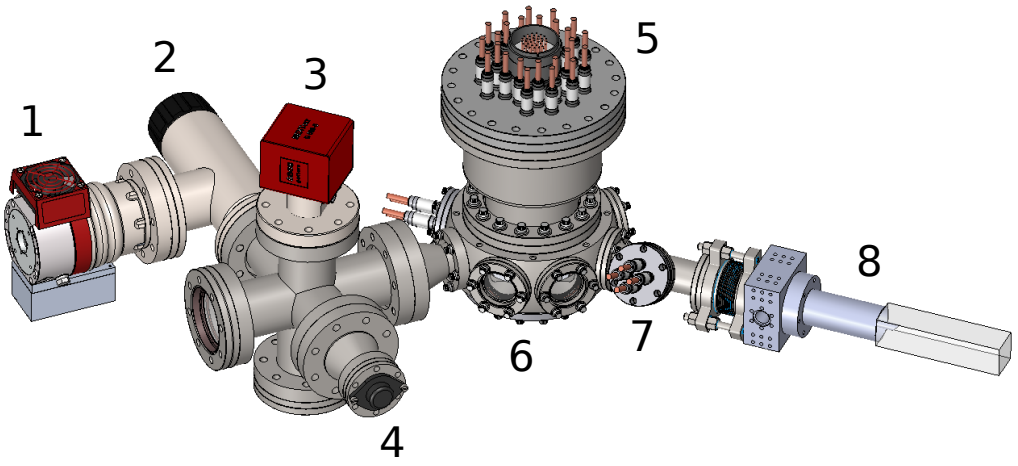


FIGURE 3.1: Schematic of the vacuum system. 1. External pump port and turbo pump. 2. Vent valve. 3. Sputter Ion Pump (SIP) with integrated Non Evaporable Getter (NEG). 4. Hot-filament ion gauge. 5. Electrical feedthroughs. 6. Main chamber. 7. Dispensers feedthrough. 8. 2D MOT. The schematics shown have been developed by various members of the laboratory over the years.

1. *External pump port and turbo pump.* The first stage for achieving UHV is done using an external "roughing pump", connected to the system via a small Klein Flange (KF), which allows for easy fitting and replacement. The are many types of roughing pumps, all of which are based on the same principle: mechanically pumping air out of the system. A "turbo pump" is seen attached to the system. The turbo pump has a set of rotary blades inside and the purpose of it is to aid the roughing pump by forcing more air out of the system and into it.

2. *Vent valve.* After using the roughing pump in conjunction with the turbo pump, and following a bakeout procedure (section 3.1.2), Ultra-High Vacuum (UHV) is achieved in the chamber. A vent valve is then closed to isolate these pumps from the rest of the system.

3. *Sputter Ion Pump (SIP) with integrated Non Evaporable Getter (NEG).* Sputter Ion Pumps are essential in order to reach a good level of UHV. They are composed of a large permanent magnet which hosts a multicell anode and titanium cathode plates. The basic principle of them is to use ions to sputter titanium off the cathode. The particles present in the background are then pumped into the walls of the cathode, and slowly buried into it as

the titanium is sputtered. Inert gases such as helium are also removed by ionisation. An SIP can only be switched on at HV pressures to avoid damage. Non Evaporable Getter (NEG) pumps work in a similar way to SIP, without ionisation. Active gases adhere to a metal substrate. NEG pumps require re-activation by heating. This NEXTorr pump achieves a pumping speed of $500\,\mathrm{l\,s^{-1}}$ for the NEG and a $6\,\mathrm{l\,s^{-1}}$ for the SIP. This system was implemented to replace a previous Titanium Sublimation Pump and a much larger and old-fashioned Sputter Ion Pump, greatly reducing the size of the setup and allowing for better optical access, as well as reducing the effective volume of air to be pumped out.

4. *Hot-filament ion gauge.* In order to read pressures at a UHV level, an ion gauge is needed. The ion gauge is formed of an anode rod surrounded by a cathode grid. Electrons are accelerated in the enclosed volume of the gauge, colliding with gas particles and ionising them. The ionised particles then hit the cathode, inducing an emission of more electrons. An ionization current is formed, which is proportional to the density of the gas and, therefore, proportional to the pressure. A tungsten filament is heated to ensure a constant controlled rate of free electrons leaving the metal, making ionisation work at lower pressures. Readings of pressures below $\approx 1 \times 10^{-10}\,\mathrm{mbar}$ are not very accurate. Similarly to SIP, ion gauges can only be switched on at HV to avoid damage.

5. *Electrical feedthroughs.* This part of the vacuum system allows electrical connections to be made from the outside to the inside of the system. Such feedthroughs are attached to a port of standard size DN100CF. The central part is used for the atom chip connections, while the larger connectors are used for the understructure, both of which are explained later in this chapter.

6. *Main chamber.* The main chamber is the space where the understructure and the atom chip sit, trapping and cooling the atoms in the central region of this component. Optical access to this chamber is realised by the use of vacuum windows, usually of a standard size DN40CF or DN63CF. The material used to construct this chamber, and most of the vacuum components, is stainless steel 316LN, which is a special non-magnetic steel. Connections such as flanges and windows are sealed in between with a thin gasket that adopts the shape of any possible imperfections. Vacuum ports also have a knife edge where the gasket sits, improving the sealing. Gaskets are typically

made out of copper, but can be made of other metals. Lithium experiments sometimes have nickel gaskets to avoid the copper reacting when in contact with lithium.

7. *Dispensers feedthrough.* The alkali gas is released into the chamber by passing a current through a dispenser. Several dispensers are mounted in different locations of the system in case one of them runs out, or breaks. Since a dispenser breaking can damage adjacent pieces of equipment, the dispensers were installed in different locations within the system, avoiding direct line of sight with the atom chip.

8. *2D MOT.* Atoms in the experiment are first trapped and pre-cooled in the 2D MOT. It contains two dispensers, and is connected to the main chamber through a small differential pumping tube, thus ensuring larger loading rates of the MOT and longer lifetimes in the magnetic trap. It is explained in detail in section 3.4.

3.1.2 Bakeout procedure

Achieving Ultra-High Vacuum is a very methodical procedure, often referred to as "bakeout". Figure 3.2 shows the pressure measurements made with the ion gauge at different stages of the pumping procedure. As explained above, the ion gauge can only be switched on at High Vacuum (HV) pressures. Therefore, the first pumping stage is not displayed in the graph.

HV is obtained with the sole use of a roughing pump and a turbo pump. After this is achieved, the chamber is covered in heating belts that will heat up the whole system evenly to 200 °C. The reason for this is to remove all of the particles that have adhered to inside walls of the vacuum components. This heating has to be done progressively to avoid any major differences in temperature along different parts of the system, since this can cause damage to them or leaks to appear. The pressure will increase as the temperature of the air inside increases. After the temperature of 200 °C is reached, the roughing pump, in conjunction with the turbo pump, will pump away these particles. Once the pressure starts levelling out, the temperature is gradually reduced to room temperature, with the pressure dropping once again during this cooling time. After pressure stabilises again, the Non Evaporable Getter (see section 3.1.1) is re-activated, producing a short

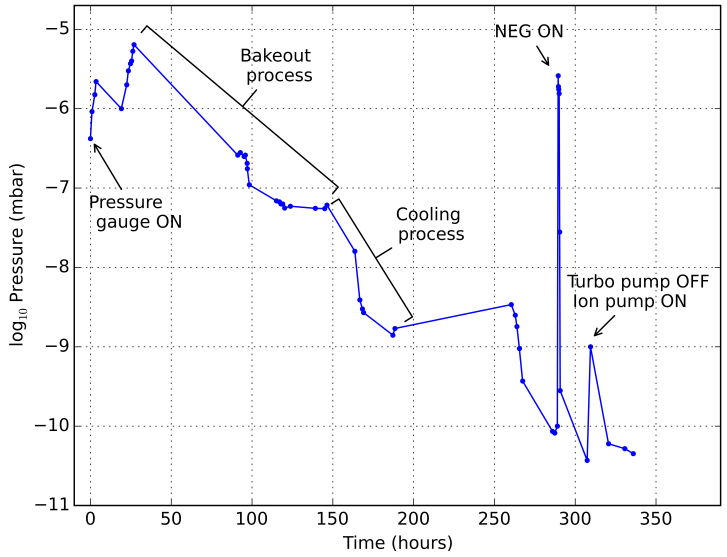


FIGURE 3.2: Bakeout procedure to achieve Ultra-High Vacuum (UHV) $< 1 \times 10^{-10}$ mbar. The hot-filament ion gauge can only be switched on in High Vacuum. After this, the bakeout procedure is represented in this graph, showing the pressure in the chamber throughout each step in the process.

peak in pressure, and quickly dropping the pressure below previous values. The roughing pump and turbo pump are switched off and the Sputter Ion Pump (see section 3.1.1) is then switched on, helping to reach and maintain a UHV.

The last step before the vacuum system is ready is to flash the dispensers at very high current for short periods of time, until the coating has evaporated. These currents are specified in the datasheet of each dispenser. Once the pressure stabilises again, the vacuum system is ready to use. The whole procedure described here took approximately two weeks to complete for this setup.

3.2 Laser system

As with the vacuum system, the laser system is also one of the key aspects of a cold atom experiment. Laser light is used in many different fields of experimental physics. It is needed to trap and cool atoms, and to image and probe the samples while carrying out experiments. Lasers are also essential to manipulate the internal state of the atoms. For this reason, the frequency and power of the laser light have to be meticulously controlled. The 780 nm D_2 cycling transition in ^{87}Rb is responsible for laser cooling. The natural linewidth of this transition is 6.1 MHz

[64]. Therefore the laser used has to have a linewidth of ≈ 1 MHz. For this reason, commercial lasers with external cavities are used in this setup.

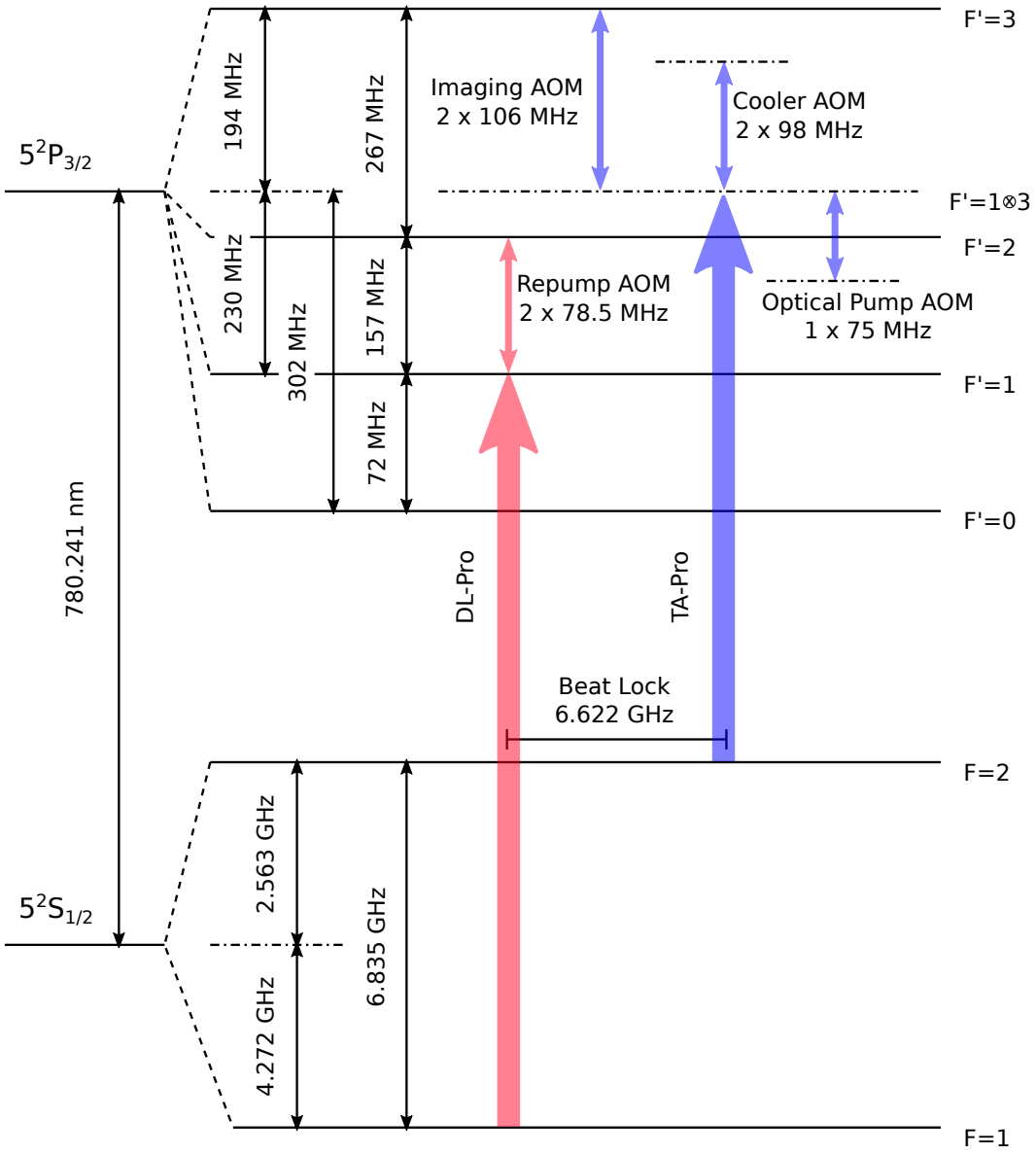


FIGURE 3.3: Level scheme of ^{87}Rb [64], with the cooling and repumping transitions. Acousto-Optical Modulator (AOM) showing the smaller frequency detunings needed for cooling, imaging, repumping and optical pumping. In blue are the lines generated with the TA-Pro laser and in red the ones generated with the DL-Pro laser.

Figure 3.3 shows the employed transitions. The repump laser is stabilised, or locked, to the $|F = 1\rangle \rightarrow |F' = 1\rangle$ transition using standard frequency modulation spectroscopy [65] to avoid any long-term frequency drift. Any change in the laser's current results in a change in the laser's frequency and power. The

atomic frequency reference to which the laser is locked is provided using Doppler-free saturation spectroscopy with a rubidium vapour glass-cell [66]. The cooling laser is stabilised with an offset of 6.622 GHz to the repump laser. This is done using a digital beat-locking technique, which constantly compares the difference to a reference frequency provided by an external frequency generator [67]. The cooling laser is then locked to the $|F = 2\rangle \rightarrow |F' = 1 \otimes 3\rangle$ crossover peak. With these two lasers stabilised, the frequencies needed for cooling, repumping, imaging and optical pumping can easily be tuned using Acousto-Optical Modulators (AOM). The AOM will shift the frequency by a determined amount. It is common practice to reflect the beam after this, to send it back to the AOM, thus doubling the frequency shift. This so-called double-pass AOM is used to avoid any spatial drifts of the light path caused by different settings in the AOM, allowing smooth frequency scanning. Additionally, the laser frequencies needed for the 2D MOT setup are also extracted from these two lasers.

Laser frequency stability is of high importance in experiments like this one. All the optics are mounted on a floating optical table to avoid any vibrations, and enclosed in a laser box, which helps to maintain stable temperature and humidity conditions, as well as keeping dust out of the optics. For this reason, very stable commercial lasers are used. In particular, there is one cooling laser (Toptica TA-Pro), one repumping laser (Toptica DL-Pro) and one tapered amplifier BoosTA for the repump line. The optics setup is shown in the schematics in fig. 3.4, with the red lines representing the light used for the main experiment. The green lines represent the light used for the pre-cooling 2D MOT stage.

The repumping light is seeded into the tapered amplifier before being split into a 3D MOT repumping AOM and a 2D MOT repumping AOM. The repumping AOM is used with double-pass at 78.5 MHz to achieve the desired repumping transition that will act on two of the 3D MOT beams and on two of the 2D MOT beams. The intensities of each of them can be independently modified.

The cooling light is split into several AOMs for 3D MOT cooling (double-pass at 98 MHz), 2D MOT cooling (double-pass at 98 MHz), 2D MOT pushing beam (double-pass with variable frequency - see section 3.4), imaging (double-pass at 106 MHz) and optical pumping (single-pass at 75 MHz).

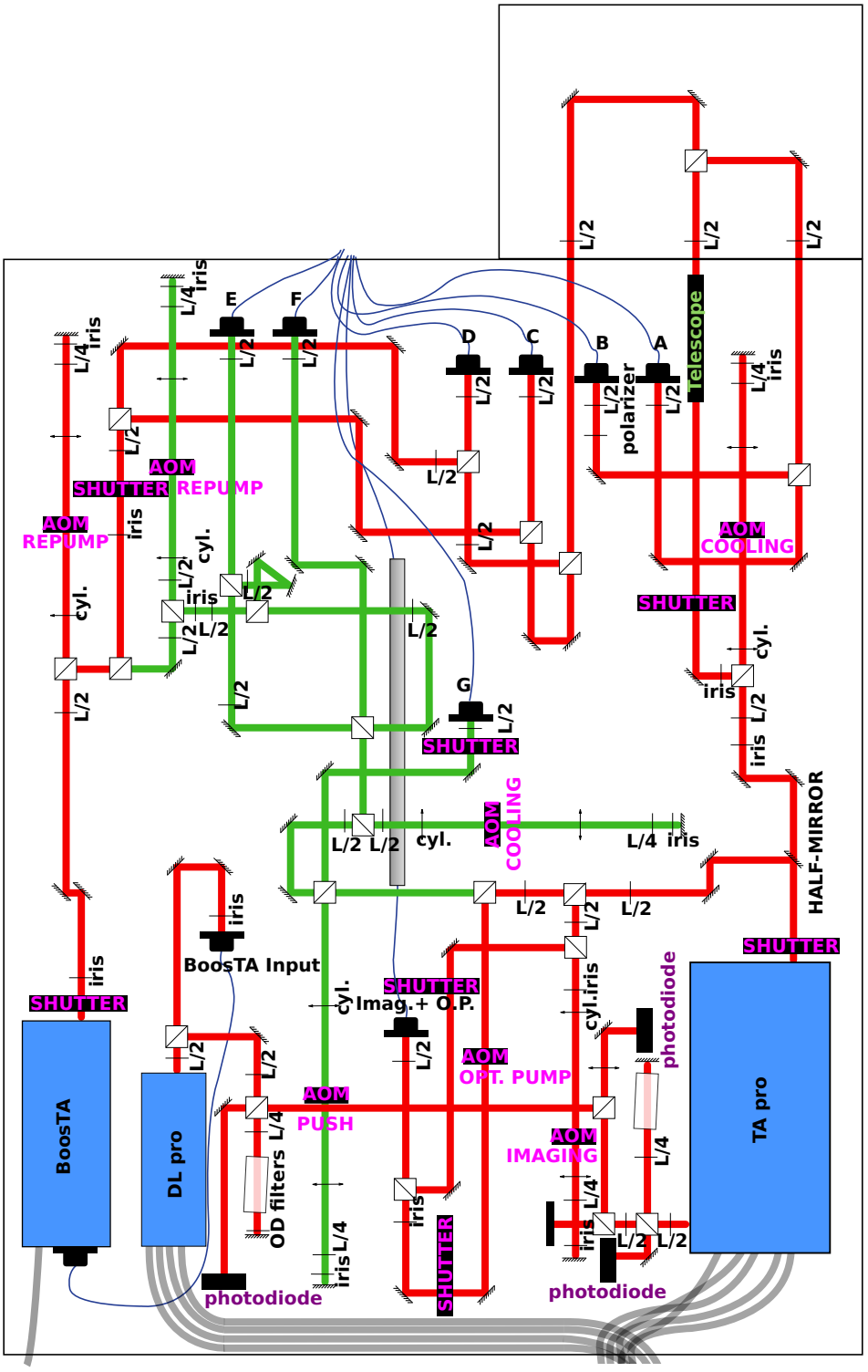


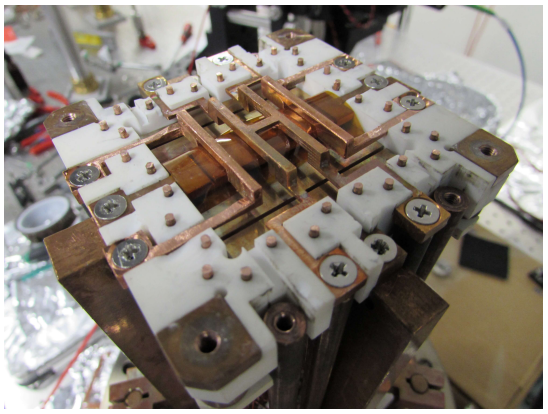
FIGURE 3.4: Schematic of the optics setup used in the atom chip experiment. Green paths indicate the optics needed to achieve the pre-cooling stage, or 2D MOT. Red paths indicate the main laser paths to create a 3D Magneto-Optical Trap, including cooling, repumper, spectroscopy, imaging and optical pumping. Schematics have been done to a scale 1:10 of the real dimensions.

3.3 Understructure to generate magnetic fields

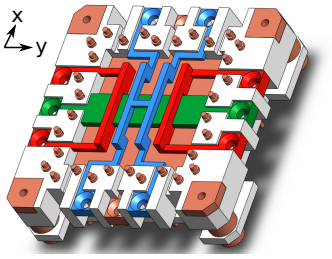
The magnetic field is needed to split the energy levels of rubidium so that the atoms can then be trapped and cooled to near-absolute zero. The most widespread way of generating magnetic fields is by using coils. Typically, a MOT type experiment will have a set of coils to create a quadrupole. In our setup, the magnetic fields responsible for trapping and cooling are generated by an "understructure", containing different shapes of copper tracks (see fig. 3.5). This was designed primarily by a previous PhD student Dr. Anton Piccardo-Selg [31]. The understructure allows for different configurations of trapping potentials, depending on the paths and directions of the current, allowing it to perform well in both the MOT stage and magnetic trap stage. Additionally, with the use of different tracks, the trapping potential can easily be modified, changing its shape, gradients and/or position. The understructure allows for fine control when performing experiments.

The understructure, shown in fig. 3.5b, consists of a central copper sheet (brown) covering the whole region, on top of which a thinner sheet (green) runs orthogonal to it. An "H" shaped track (blue) and two "sidebars" (red) are present on top of the sheets. This is all embedded in a boron nitride piece, which keeps the structure in place. The copper tracks are then connected via copper rods to the feedthrough. The atom chip is screwed on top, using four screws on the corners of the understructure, and its connections are realised using spring-loaded rods. This technique, although tricky to first set up, provides a very fast and user friendly way of swapping chips. The whole understructure and chip are placed upside down inside the chamber to be able to let the cloud of atoms undergo a ballistic expansion.

Planar structures are capable of producing the necessary magnetic fields for a MOT and magnetic trap, although for convenience a bias field is sometimes generated with coils. This ensures a more homogeneous bias field. In this setup, the MOT is created with a U-MOT type of trap, which consists of a planar U shaped copper structure accompanied by a bias field. In our setup, this can be achieved in several ways. The first alternative is to use the "H" shaped central piece (blue tracks in fig. 3.5b) with current flowing between either the top two or the bottom two contacts. This gives a simple and relatively low power consumption MOT when an additional bias field is generated by using two external coils in Helmholtz configuration. This setup was later changed to be able to control the height and



(a) Understructure photograph.



(b) Understructure CAD drawing.

FIGURE 3.5: Understructure of size 70 × 70 mm for creating the magnetic field for a Magneto-Optical Trap (MOT) and a magnetic trap. The red and green tracks in (b) are used together in the MOT stage creating an effective U-MOT. The blue track is used for the magnetic trap stage with current flowing in a Z shaped configuration. The atom chip is mounted on top of this understructure, using a screw in each corner. The electrical connections for the chip are realised with spring loaded push rods.

shape of the potentials independently. In this case, the green sheet in fig. 3.5b was activated, in conjunction with the red sidebars and the external coils to create the bias field. The currents through both of the structures are driven with independent power supplies. The magnetic trap stage is generated by connecting the "H" shaped track to form a Z shaped current path, and the bias field is again generated with external coils in the Helmholtz configuration. The reason to not use the same configuration as in the MOT stage is due to the Majorana spin flips, described in the previous chapter. It is very important that this Z shaped current path flows in the same direction as the Z shaped wires of the atom chip, to ensure a fast and efficient transition between the understructure magnetic trap stage to the atom chip magnetic trap stage. The bias field can be created by the bottom sheet of the understructure if desired, although the resulting magnetic bias field is not as homogeneous, leading to shorter lifetimes of the trap and a less efficient evaporative cooling process.

In addition to the understructure, the chamber is surrounded by five pairs of coils. With the x and y coordinates as shown in fig. 3.5b and the z coordinate being away from the surface of the chip, there are two pairs of X-Bias (with the coil plane parallel to the yz plane) coils, two pairs of Y-Bias (with the coil plane parallel to the xz plane) coils and another pair of Z-Bias (with the coil plane parallel to the xy plane) coils. One of the X-Bias pair of coils is used in the formation of the

MOT trap and the other pair in the formation of the magnetic trap, as described in the previous paragraph. The first Y-Bias pair of coils is used to modify the bottom of the magnetic trapping potential in the magnetic trap stage, as well as in the atom chip trap. The other two pairs of coils, with the help of the X-Bias used in the MOT, are used to compensate for external unwanted magnetic fields in all three spatial coordinates, as well as to move and position the cloud in certain regions of the chamber. The X-Bias pair of coils used for the MOT is also used in the optical pumping stage. Although the compensation coils are not needed for trapping and cooling, they are essential to position the cloud of atoms in the correct place to perform transitions between the MOT and the magnetic trap and between the magnetic trap and the atom chip magnetic trap.

To ensure a precise magnetic field, the current flowing through the understructure, as well as through the coils, should ideally be constant. Typically, the current coming out of a power supply is of constant voltage, with the current being dependent on the resistance of the load. If the resistance of the load changes, the current changes and, in an experiment of this kind, the magnetic field changes. Since large currents are driven, the temperature on the understructure and coils will change dramatically from when it is first switched on to when it is fully warmed up. This causes a long term drift that will stabilise faster or slower depending on the current, the material, and the cross-section of the conductor. In some experiments, hollow-core water-cooled coils are employed to avoid excessive heating. The best way of controlling the current out of a source is to constantly drive a larger current and build a circuit with a feedback that transforms the excess current into heat and dissipates it with a large heat-sink. For the majority of the magnetic field generating devices in this experiment, running the power supplies in voltage controlled mode results in a long term drift that stabilises in some thirty minutes, thus eliminating the need for current regulation. In the case of the power supply employed for the Z shaped track, this effect is more dramatic due to the use of larger currents, and the magnetic fields drift even during each experimental cycle. For this reason, this power supply had a large current controlling box, built by the electronics workshop of School of Physics and Astronomy, University of Nottingham.

3.4 2D MOT

The use of a pre-cooling stage has been mentioned several times before in this thesis. In this section, the design and implementation of such a system is explained in detail. The reasons that lead to this modification are also stated. The basic design of the apparatus has been taken from the author's final year M.Sci. project [33] done prior to the work described in this document, and based on a design from the University of Heidelberg [68, 69]. This design is characterised by the use of three or four independent trapping and cooling regions, as opposed to the most common version with only one elongated region [70]. The three regions setup has proven to be equally effective and, at the same time, cheaper to build, due to the use of standard optics instead of the more expensive custom made elongated lenses and mirrors.

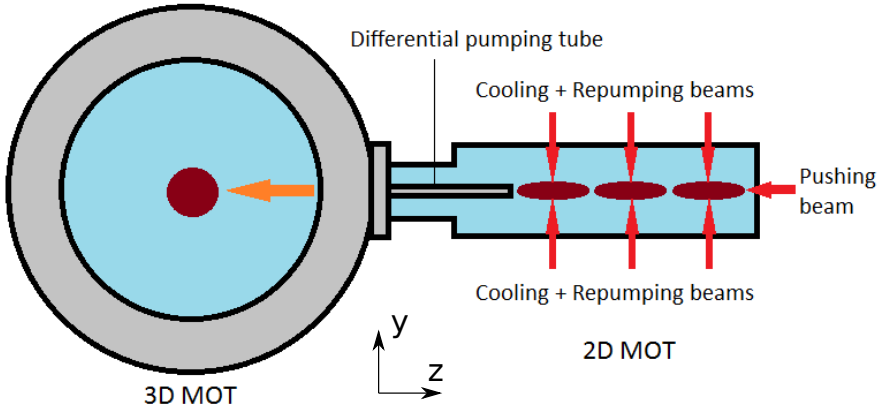


FIGURE 3.6: Simplified diagram showing the main chamber on the left, with a cloud of atoms (red disk) trapped inside, and the 2D MOT attached to it on the right. The orange arrow shows the trajectory that the atoms will take from one chamber to the other, passing through a differential pumping tube. In the 2D MOT, atoms are trapped within three different cooling regions to produce three elongated clouds of ^{87}Rb (red ellipses) [33].

Bose-Einstein condensation was achieved prior to the implementation of this device. Unfortunately though, the background pressure instability during the magnetic trap stage meant that condensation was only achieved for a few hours per day. When the dispensers are first switched on after several hours of being switched off and with the pumps working, the density of trappable particles increases rapidly, making condensation possible. After a few hours, the background pressure of non-trappable particles slowly increases, incrementing the rate of ^{87}Rb atom collisions with background particles. Additionally, the cycle of the dispensers had to be

run pulsed, driving larger than usual currents during the MOT stage but none during the evaporative cooling cycle, thus risking damage to the dispensers. For this reason, the implementation of the previously designed pre-cooling stage was necessary. A pre-cooling stage, such as the 2D MOT, is of great importance for two main reasons;

- Dispensers are outside the main experiment chamber, which helps to control the background pressure in the experiment thanks to a differential pumping tube dividing both chambers.
- Atoms are trapped and pre-cooled before being sent into the 3D Magneto-Optical Trap increasing the loading rate of it. This effectively acts as a velocity selector, as well as ensuring that only trappable ^{87}Rb is sent into the main chamber, leaving unwanted particles in the 2D MOT glass cell. Normal commercial rubidium dispensers are generally composed of 72 % of the ^{85}Rb isotope, and only 28 % of the ^{87}Rb isotope.

This type of pre-cooling stage is called a 2D MOT simply because it follows the same principle of trapping and cooling as the well known MOT, but only acts on two dimensions instead of three, generating a quadrupole field along one axis [50]. A basic diagram on the principle of this 2D MOT stage is shown in fig. 3.6, where atoms are first trapped in the 2D MOT glass cell along three different regions of space, and then pushed with the aid of a pushing beam towards the 3D MOT chamber. Figure 3.7 is a photograph of the fully implemented and functioning 2D MOT running in the experiment. The components of it are as follows:

1. *Glass cell.* The vacuum is generated inside this glass cell type of chamber, which is custom made to the desired size by company Japan Cell. It is made out of Schott Tempax Borofloat glass with a 780 nm anti-reflection coating on the outside. The size of this cell is $245 \times 35 \times 35$ mm with the flat-sided usable length of 140 mm. This glass cell design was carried out prior to the work presented in this document [33].
2. *Permanent magnets.* Two aluminium rectangles with permanent magnets placed inside are positioned flat to the diagonal of the glass cell, at a 45° angle from the xz plane. Polarity of the magnets is opposite in each bar, creating the necessary quadrupole field inside the glass cell to trap and cool ^{87}Rb. The magnets are explained in more detail in section 3.4.3.

3. *Compensation coils.* Two pairs of compensation coils were wound to better control the position of the cloud with respect to the differential pumping tube that connects the two chambers.

4. *Optics cubes.* These cubes, containing a Polarising Beam Splitter (PBS), a $\lambda/2$ plate and a $\lambda/4$ plate, are responsible for the correct splitting and polarisation of the light distributed among the three trapping regions. This optics cubes design was carried out by the author, prior to the work presented in this thesis [33].

5. *Cooling and repumping guns.* These tubes contain the optical fibre outcouplers, and the collimating optics, directing cooler and repumper light to the optics cubes.

6. *Pushing beam.* Optical fibre outcoupler for the pushing beam, responsible for aiding in the transfer of atoms to the main chamber of the experiment.

7. *Vacuum flange with differential pumping tube.* The whole structure and glass cell are supported by this custom made DN40CF vacuum flange, which includes the differential pumping tube that connects the two chambers. It was built by company LewVac out of 316LN stainless steel. Feedthroughs for dispensers are connected through a standard CF16 vacuum port. This flange design was carried out by the author, prior to the work presented in this document [33].

8. *Dispensers.* Rubidium is evaporated inside the 2D MOT chamber using two dispensers, placed on either side of the differential pumping tube. Small connectors had to be carefully designed to make sure they fit inside the narrow part of the glass cell, without touching other components. Any contact with other components can result in damage from the high temperatures produced by the dispensers and/or short-circuiting of the electrical connections.

9. *Port aligner.* The port aligner bellow, purchased from company Lesker, is placed between the 2D MOT and the rest of the vacuum system. It is used to align the stream of atoms exiting the 2D MOT with the centre of the trapping potential in the 3D MOT. Gravity has to be accounted for when aligning the 2D MOT stage.

Figure 3.8 is a fluorescence image taken at the position of the pushing beam outcoupler, looking straight into the differential pumping tube. Atoms can be

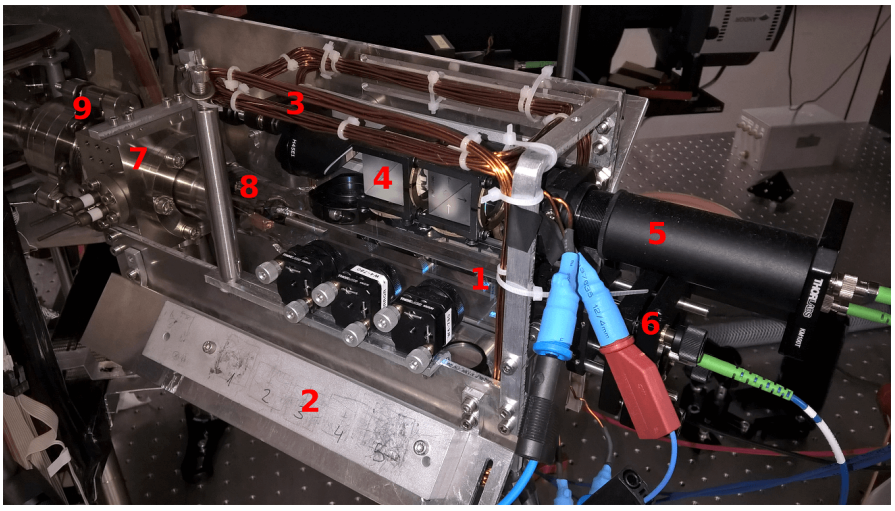


FIGURE 3.7: Photograph of the 2D MOT pre-cooling stage implemented in the setup. 1. Glass cell. 2. Permanent magnets bar. 3. Compensation coils. 4. Optics cubes to split light for the three independent regions. 5. Cooling and repumping beam guns. 6. Pushing beam outcoupler. 7. Custom built flange with integrated differential pumping tube and support for the structure. 8. Dispensers inside the glass cell mounted to feedthrough with home-made connectors. 9. Port aligner bellow connecting 2D MOT with 3D MOT main chamber. See text for details.

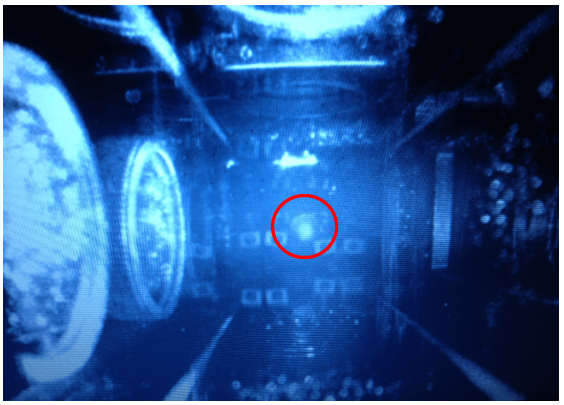


FIGURE 3.8: Fluorescence of ^{87}Rb atoms inside the 2D MOT along the longitudinal axis of the trap (marked with a red circle). Picture taken with a finger camera without IR filter.

seen trapped in the centre of the glass cell, marked with a red circle. This image was taken in this direction since the Optical Density (OD) is not sufficient for the atoms to be seen along the longitudinal axis. The camera is a cheap "finger" camera that does not contain any IR filter.

A different method for slowing down atoms, that is also commonly used, is the "Zeeman slower" [71]. It consists of a large tube surrounded by different coils that generate different magnetic fields. Atoms travelling at high speed through

the tube are slowed down before they reach the main chamber. The slowed down atoms are effectively cooled down and increase the chances of getting trapped in the MOT. This type of slower is also used for other types of particles, such as lithium, that needs to be preheated in an oven and leave the oven at high speeds [72]. It is also common in mixture experiments, in which different species of atoms can be slowed down using the same Zeeman slower with different currents running through the coils for each species [62]. Some versions use permanent magnets that are placed closer or further away from the tube depending on the desired magnetic field [73]. For ^{87}Rb atoms, the 2D MOT setup has proven to be very reliable over the years [74, 75].

3.4.1 Pressure difference

The greatest advantage of using a different chamber to first trap and cool the atoms is to be able to maintain a different pressure in different stages of the experiment. As discussed before in this document, the MOT stage of the experiment benefits from a large background pressure of trappable particles, as opposed to the magnetic trap stage where the higher background pressure results in losses. With a 2D MOT setup, the dispensers run only in the separated chamber, increasing the pressure in this chamber. Once the atoms are trapped, they can be transferred into the main chamber, which contains the Sputter Ion Pump (SIP) and sits at a lower pressure.

The difference in pressure between two chambers is given by the dimensions of the connecting tube. A thinner and longer tube will maintain a larger pressure difference than a shorter and wider one. This flow resistance occurs as a result of friction among the gas particles themselves and with the wall surface. In vacuum technology, it is common to refer to the conductance, which is the reciprocal of the flow resistance. Given a tube with length L and internal diameter D, both in centimetres, the conductance when $L \gg D$ scales as [76]

$$C = \frac{12.1 D^3}{L}. \tag{3.1}$$

If several geometries inside the connecting tube are present, the total conductance is

$$\frac{1}{C_T} = \frac{1}{C_1} + \frac{1}{C_2} + ... \tag{3.2}$$

The pressure difference between the two chambers will then be given by the effective pumping speed S_{UHV} of the vacuum system [76]

$$\frac{P_{2D}}{P_{3D}} = \frac{C_T}{S_{UHV}}. \tag{3.3}$$

The setup presented in this document has a differential pumping tube with two different stages, the larger one with $L = 153\,\text{mm}$ and $D = 5.6\,\text{mm}$, and a smaller tube on the 2D MOT side with $L = 8\,\text{mm}$ and $D = 0.8\,\text{mm}$. Figure 3.9 shows the internal geometry of the differential pumping tube. The vacuum pumping system has an efficiency of $500\,\text{l}\,\text{s}^{-1}$. Due to its location, far from the main chamber, the effective pumping speed will be reduced to a few tens of $\text{l}\,\text{s}^{-1}$. This leads to a pressure difference between the chambers of $P_{2D} \approx 10^3 P_{3D}$. Therefore, the pressure in the 2D MOT can be raised up to $10^{-7}\,\text{mbar}$ without experiencing dramatic losses in the experiment's magnetic trap lifetime.

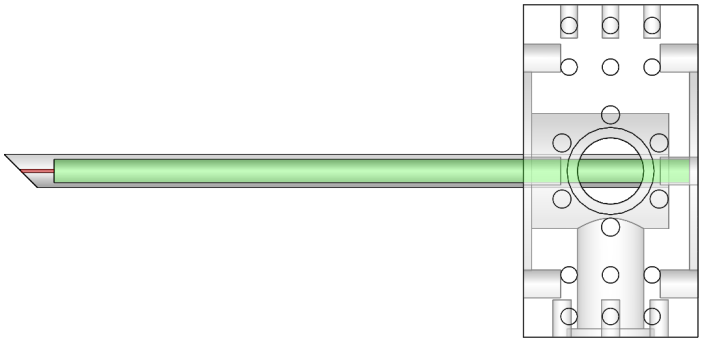


FIGURE 3.9: CAD drawing to scale of the flange with transparency showing the two stages of the differential pumping tube (red and green) integrated in the custom made vacuum flange, viewed from the side. The total length of the tube is 165 mm.

At the same time, as well as keeping the desired difference in pressure, the physical angle at which the atoms can enter the main chamber has to be as large as possible. This is the reason why some setups contain a set of differential pumping tubes that progressively increase in diameter. In the setup described here, this angle is

limited by the shorter piece of tube, which gives a solid angle of 36.6 mrad. The Heidelberg setup [68] gives a solid angle of 64 mrad at the cost of a lower efficiency of the differential pumping tube.

3.4.2 Optics setup

The trapping and cooling technique in a 2D MOT does not differ from the technique used in a 3D MOT. Cooling and repumping transitions have to be induced with laser light. In this setup, the cooling and repumping beams come from the same set of lasers used for the main experiment. The frequency shift is achieved using different AOMs since the timings are different from the 3D MOT. The 2D MOT light can be left constantly on so that atoms are already trapped and cooled before the 3D MOT loading even starts. To achieve a good radiation pressure balance, both cooling and repumping light are combined and sent in the two spatial components of the 2D MOT. The optics setup to prepare the light is shown in green in fig. 3.4. Each of the two beams is then split into three different regions, and sent into the glass cell, as shown in fig. 3.10. The light is then retro-reflected to achieve the two dimensional trapping. Some experiments contain four trapping regions [77], and claim no significant improvement from the three regions setup. The detuning of the cooling and repumping beams employed is similar to the one for the 3D MOT. The cooling light was found to saturate at ≈ 100 mW of total combined power, where the repumping was saturating at ≈ 10 mW. This light is then split into six retroreflected beams using 1" optics.

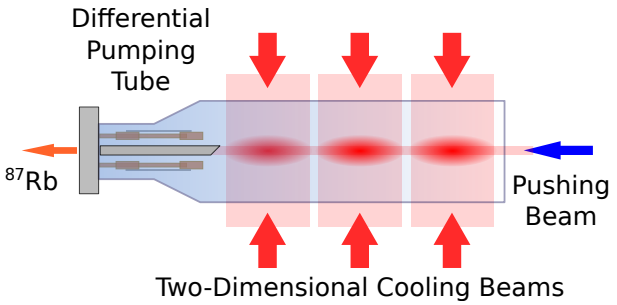


FIGURE 3.10: Schematic of the optics employed on the 2D MOT apparatus, showing the splitting of cooling and repumping light into the three regions. Two rubidium dispensers can be seen inside the glass cell, adjacent to the differential pumping tube. Image for visualisation purposes, not to scale.

Once atoms are successfully trapped and cooled inside the 2D MOT glass cell, they have to be transported to the main chamber, through the differential pumping tube. For this, an additional beam is set up, called the pushing beam (see fig. 3.10). The optimal power for this beam was found to be $\approx 480\,\mu W$. Regarding the detuning, the setup was found to work to a good standard with both red-detuned (negative detuned) light and blue-detuned (positive detuned) light over the cooling transition. A red-detuned beam would act on the atoms travelling towards the oncoming beam, effectively pushing them and turning them around. A blue-detuned beam, on the other hand, would act on the atoms travelling in the same direction as the beam, effectively giving a further kick to the atoms already travelling towards the differential pumping tube. Even though both detunings worked well, and a lot of groups claim red-detuning to work better [68], in this experiment having the pushing beam blue-detuned seemed to be the optimum setup. The pushing beam also greatly helped with the alignment of the bellow, since the beam could be seen passing through the differential pumping tube and reflected on the internal surface of the main chamber, giving an idea as to where the stream of atoms would point.

Several groups have implemented the so-called 2D+ MOT. It is based on the same principle of two-dimensional trapping and cooling but, additionally, some light is sent in the third spatial dimension along the longitudinal direction [78]. For this purpose, the tip of the differential pumping tube of the setup described here was designed to be at a 45° angle to the walls (see fig. 3.9) and polished to be reflective. In this way, a beam can be sent from the bottom of the apparatus, reflecting onto this surface, and acting as an additional trapping component together with a red-detuned pushing beam. Although some groups claim an advantage with this setup [68], a quick test in the laboratory showed no visible improvement on the behaviour of the 2D MOT. A blue-detuned pushing beam without the additional reflecting beam was found to be more efficient than the implementation of the 2D+ MOT system.

3.4.3 Permanent magnets

When designing magnetic field generating structures for atom trapping and cooling, several factors have to be accounted for. Typically, the MOT magnetic field is created using large coils sitting outside the UHV chamber. The reason for this

choice is that coils are reliable, relatively simple to design and build, if great accuracy of the field is not needed, and are very inexpensive. The major disadvantage of the use of coils is the power consumption, which, in a laboratory, is not usually a handicap. It is also important to take into account whether there is a need to eventually switch off these magnetic fields, e.g. for imaging purposes. In the case of a 2D MOT, permanent magnets seemed to provide the best balance between the pros and cons. Magnetic fields do not need to be turned off at any stage of the experiment, and the apparatus is far away enough to not interact dramatically with the main experiment.

A set of aluminium bars was designed to host the permanent magnets. In this way, the whole set of magnets can be moved around and positioned altogether with ease. Each aluminium bar was placed at each end of the diagonal of the cross-section of the glass cell (see fig. 3.7), forming a 45° angle with the horizontal xz plane. The magnets, of size $25 \times 25 \times 5$ mm, were acquired from company "First4Magnets", and are made out of N42 Neodymium, with 11 kg of pull. Initially, weaker magnets were acquired, relying on the results of the simulations but, after experimental testing, it was discovered that magnets quickly lose $\approx 25\,\%$ of their magnetisation. A quadrupole field is then generated in the glass cell. The simulation of the quadrupole field, shown in fig. 3.11, was done using Finite Element Method Magnetic (FEMM) software, which is open-source software specifically meant for simulating fields generated by permanent magnets. The red arrows in the picture show the opposite polarisation of the magnets. The set of magnets are placed at different distances from the edge of the aluminium holder, as seen in fig. 3.12. In this way, the field created along the longitudinal z axis is more linear in space, and slightly stronger on the tip of the tube, ensuring that atoms are squeezed towards the hole. The bars can be displaced freely along the xy plane, ensuring that the correct magnetic field gradient is achieved, and that the centre of the quadrupole field aligns with the hole in the differential pumping tube.

The external coils seen in fig. 3.7 were added to better control the positioning of the atom cloud with respect to the hole in the differential pumping tube. They are not necessary, since this can be optimised via the positioning of the permanent magnets aluminium bars alone. Nevertheless, the ability to precisely control the position without physically moving components, give these coils a great advantage. The coils were home-built, optimised primarily for the shape of the structure and to allow access to manipulate and align the optical components of the system. A

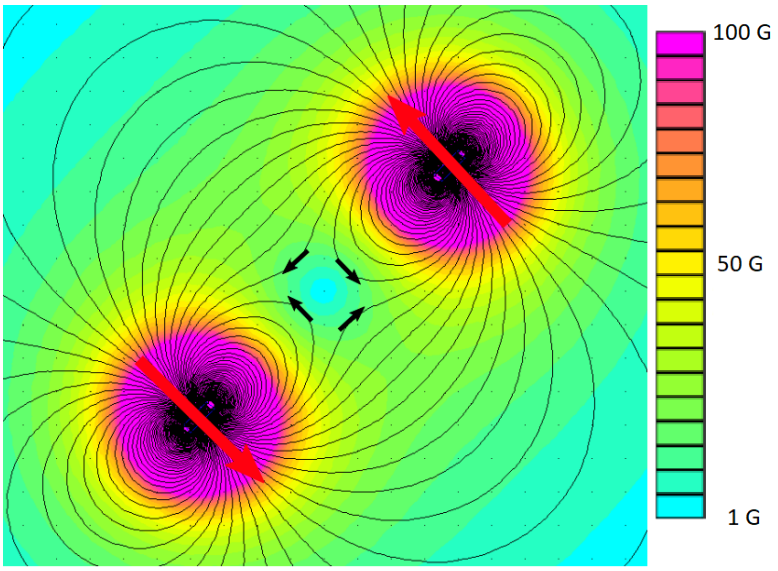


FIGURE 3.11: Colour map showing the quadrupole magnetic field generated by two permanent magnets at a distance of 100 mm from each other in the xy plane cross-section of the 2D MOT. Orientation of the poles of the permanent magnets is shown with red arrows. Simulation carried out using opensource Finite Element Method Magnetics (FEMM) software.

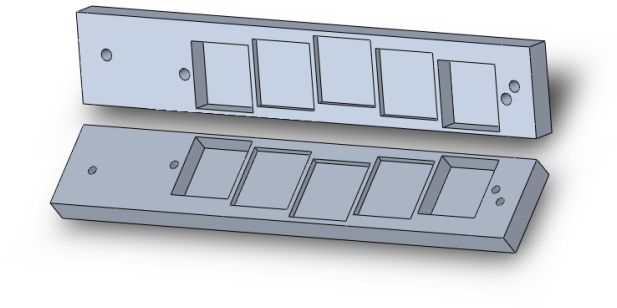


FIGURE 3.12: SolidWorks drawings of the permanent magnet bars designed and built in-house. Different number of magnets are placed in each slot, which are at different distances from the edge, to create the desired magnetic field. The base and the lid are screwed together and then fixed to the 2D MOT structure using two screws.

great benefit of having external compensation coils in a 2D MOT stage, is that the cloud of atoms can be pushed far away from the hole after the 3D MOT is loaded. This avoids any possible leak of atoms into the 3D MOT chamber.

Overall, the improvement on the experimental cycle has been excellent. The 3D MOT loads to a few hundred millions of atoms in 10 s, whilst maintaining a vacuum pressure between 1×10^{-10} mbar and 1×10^{-11} mbar. For practical purposes, this resulted in repeatable and stable Bose-Einstein condensate (BEC) production.

Even after having the system off for a long time, BEC is achieved in the first minute after switching on the apparatus. This fact, when compared to other setups, indicates the high performance of this apparatus.

Aside from the great improvement for this experiment, the successful realisation of trapping and cooling atoms using permanent magnets is a big step towards low power consumption portable devices. In such devices, one can think of a MOT stage with permanent magnets, and the field can be cancelled temporarily for science or imaging purposes, with the use of optimised coil design techniques. These devices would benefit from a very low power consumption and reduced size. Colleagues in Nottingham are currently designing and making such structures.

3.5 Magneto-Optical Trap (MOT)

In order to carry out experiments with cold atom, the first step is to trap and cool the atoms in the experimental chamber. The MOT is a very powerful and robust system, not very sensitive to misalignment of the optics, changes in detunings or changes in background pressure. At this point of the cycle, ^{87}Rb atoms at a few hundred degrees Celsius are captured and cooled down to a few tens of micro-Kelvin. In the case of the experiment described in this document, the loading of the 3D MOT is done from a stream of already cooled atoms emerging from the 2D MOT stage, making the capture efficiency of the 3D MOT even greater. The theory behind the MOT has been addressed in section 2.1, where it is explained how the MOT relies on a combination of splitting of atomic energy levels with external magnetic fields and a set of laser beams with the correct detuning and polarisation acting on all three spatial dimensions.

The production of the desired quadrupole magnetic fields is done using an understructure, described previously in this chapter. Current flows along the green sheet bar and along the red sidebars (see fig. 3.5b) forming a U shaped pattern. This is accompanied by a homogeneous external bias field generated by X-Bias coils that surround the chamber. The sheet bar is typically run at 80 A, the sidebars at 20 A and the X-Bias coil at 3.2 A, the latter producing a homogeneous bias field of magnitude 5.5 G. It is important to take into account the heating and consequent expansion of the copper understructure due to large currents. The long rods connecting the feedthrough to the understructure have a large thermal

expansion and can lead to short-circuiting of the different elements of the understructure, and even push the atom chip which sits on top. Electrical isolating and vacuum compatible Kapton tape was added in the newest version to avoid any short-circuiting. Nevertheless, damage on the chip can still happen if the expansion of the rods is excessive. To avoid this, the sheet bar is only driven at 80 A, instead of the larger currents with which the MOT increases its performance. The distance of the atoms to the surface during the loading stage is typically ≈ 6 mm, and can be adjusted by changing the currents employed.

Perhaps intuitively, the optimal arrangement of the oncoming beams would be all three components orthogonal to each other. The nature of this experiment, containing an atom chip, makes this configuration not valid, since one of the axes is completely blocked by the understructure containing the atom chip. Additionally, the axes of the quadrupole field generated by the U shaped structure, forces two of the beams to shine in with an angle with respect to the surface of the chip. The MOT configuration in this case is the so called "Mirror-MOT" [79]. One of the spatial coordinates is addressed horizontally using two counterpropagating laser beams through the side DN40CF windows of the chamber. The other two spatial coordinates are addressed from the bottom DN100CF window. Two beams, coming at a 32° angle with respect to the vertical, are shone onto the surface of the chip and reflected back (see fig. 3.13). This angle should be as close to 45° as possible, but is limited by the physical configuration of the chamber and the Z-Bias coils. The surface of the atom chip is built with a high (98 %) reflection coefficient for this purpose. The loading efficiency of this type of MOT is good for an atom chip experiment, in which the chip itself has a limitation in the number of atoms that can be loaded.

The MOT light is transported from the optical bench with the aid of polarisation maintaining optical fibres. These help to maintain polarisation as well as to restore and improve the gaussian shape characteristic of a laser beam. After the fibre output, the beams are collimated with a lens. The output light from a polarisation maintaining fibre is linearly polarised to the fast axis of the fibre. A $\lambda/4$ plate then converts this polarisation into the desired circular polarisation (see section 2.1 for details). The $1/e^2$ diameter of the MOT beams after collimation is 20 mm, which is large enough for trapping whilst still fitting on the surface of the chip. Any light hitting the edges of the atom chip would produce unwanted reflection that would affect the efficiency of the setup. The light intensity of the cooling beams was found

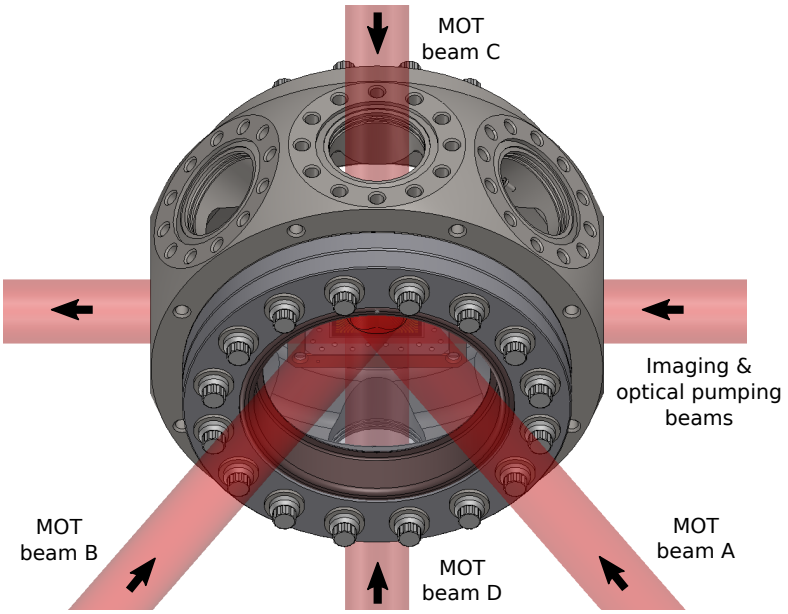


FIGURE 3.13: CAD drawing of the orientation of the MOT beams with respect to the chamber. The imaging beam crosses the chamber from side to side in the drawing, with the rest of the beams being cooling and repumping light. The bottom beams are incident at an angle of 32° with respect to the vertical, and reflect from the chip surface and onto each other's paths.

to be optimum at 50 mW each for the bottom beams, and 30 mW each for the two horizontal counterpropagating beams, resulting in a good atom number and low temperature in the MOT. For convenience, repumping light was only added to the horizontal beams, with a combined power of 12 mW. The distribution of the light intensity between beams is carried out on the optical bench. Detuning of the cooling AOM was found to be optimum at 196 MHz, 16 MHz from the $|F = 2\rangle \rightarrow |F' = 3\rangle$ transition (see fig. 3.3).

The cloud of ^{87}Rb atoms is constantly monitored on a TV screen with a finger camera set on one of the side DN40CF windows of the main chamber. Atoms can be seen due to fluorescence. An example is shown in fig. 3.14.

Thanks to the addition of the 2D MOT stage, the atom loading rate of the 3D MOT is up to $5 \times 10^7\,\mathrm{s}^{-1}$, reaching a few hundred millions of atoms in 10 to 15 seconds. It is important to note that the MOT can be optimised for greater atom number, but this does not necessarily mean better efficiency. A larger number of atoms can result in a higher overall temperature and/or lower density, leading to more pronounced losses during transfer to the magnetic trap.

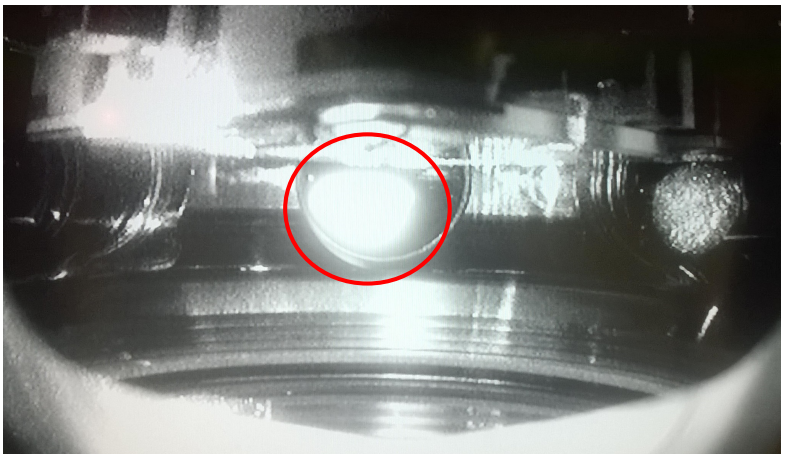


FIGURE 3.14: Photograph of a typical mirror-MOT fluorescence image. Atoms can be seen in the centre of the chamber, inside the red circle, at 6 mm from the surface of the chip. Photograph taken with a finger camera without IR filter.

3.5.1 Sub-Doppler cooling and compression

This type of cooling presents a lower temperature limit, at which the heating due to spontaneous emission of the atoms competes with the cooling process (see section 2.1.2). This Doppler cooling limit is given by [64]

$$T_D = \frac{\hbar\Gamma}{2k_B}, \tag{3.4}$$

where Γ is the natural linewidth of the electronic transitions, resulting in a temperature limit of $\approx 145\,\mu K$ for ^{87}Rb atoms. Cooling below this limit is achieved using other techniques, such as polarisation gradients in an optical molasses [80]. In the setup described here, in the last 5 ms of the MOT, the cooling beam is detuned up to four times its value, and due to the AOM's reduced efficiency at this point, the intensity of the beams is also reduced. Since the temperature of the sample is directly proportional to the intensity of the light, and inversely proportional to the detuning, this simple mechanism reduces the temperature. To illustrate this technique, a temperature measurement is shown in fig. 3.30. With this technique, temperatures down to a few tens of micro-Kelvin have been observed in the MOT.

At the end of the MOT stage, the cloud of rubidium atoms is at a distance of ≈ 6 mm from the surface of the atom chip. At this distance, the atoms cannot be captured by the magnetic trap produced by the understructure. For this reason, in the last 200 ms of the MOT loading process, the field from the X-Bias coils is increased by up to three times its initial magnitude, effectively pushing the cloud

of atoms to a distance of $\approx 1.5\,\text{mm}$ from the surface of the chip. The additional Y-Bias and Z-Bias coils are used to accurately position the atomic sample matching the position of the centre of the magnetic trap. The current in the sheet bar and the sidebars is modified at the same time to shape the cloud of atoms.

3.6 Magnetic trap

Once the cloud of atoms has been compressed and moved closer to the surface of the chip, a transfer to a purely magnetic trap is then carried out. This magnetic trap is achieved with the use of the central "H" shaped track in the understructure (represented in blue in fig. 3.5b), passing current from one of the extremes to another, effectively driving the current in a "Z" shaped. This, with the addition of an external homogeneous bias field generated using the X-Bias coils, creates the desired magnetic trap potentials.

The transfer of atoms from the Magneto-Optical Trap (MOT) stage to the purely magnetic trap stage is a very delicate procedure. It requires optimisation to reduce the atom number losses during the transfer and to avoid excessive heating of the whole sample. For this transfer to be as efficient as possible, the two trapping potentials from the MOT and magnetic trap have to be centred in the same position, and the magnetic trap stage should be deep enough to host the whole cloud of atoms being transferred. If there is a large trapping potential mismatch between the initial and final traps, the cloud of atoms will try to follow the change, resulting in a loss of atoms and an overall heating of the sample. For this reason, the initial magnetic trap is set to be weak, maximising the number of atoms trapped. To check if the two traps (MOT and magnetic trap) are centred in the same position, a scan of position versus time after transfer is performed, showing oscillation of the atoms. The closer together the two traps are, the smaller this oscillation will be.

As explained in section 2.2, a purely magnetic trap will only trap atoms in the magnetic spin states $|F = 2, m_F = +1\rangle$ and $|F = 2, m_F = +2\rangle$. Additionally, in the later compression of the trap and evaporative cooling procedure, the experiment is optimised for the $|F = 2, m_F = +2\rangle$ state, which experiences a tighter confinement compared to the $|F = 2, m_F = +1\rangle$ state. In the MOT, atoms are distributed over the five magnetic spin states of the $F = 2$ state, $m_F = -2, -1, 0, +1, +2$. For this

reason, it is important to first transfer as many atoms as possible to this state. This is achieved via optical pumping and described in detail in section 2.2.1. After all the fields and laser light for the MOT are switched off, optical pumping is carried out. For a period of time of 3 ms, atoms in all five states are addressed with a homogeneous magnetic field of 3 G created by the X-Bias coils, splitting the energy levels of the atoms. A pulse of light of 3 ms from a single pass AOM shift of -75 MHz (see fig. 3.3) is sent through a polarisation maintaining optical fibre (same fibre as the imaging beam), with a σ^+ circularly polarised light, addressing all $\Delta m_F = +1$ transitions. In this way, atoms undergo the $|F = 2\rangle \rightarrow |F' = 2\rangle$ transition with a $\Delta m_F = +1$, leading to $\approx 96\,\%$ of the atoms being trapped in the $|F = 2, m_F = +2\rangle$ state. During this period of time, repumping light is also shone into the sample, to recover atoms falling to the dark $F = 1$ state. Proper functioning of the optical pumping procedure can be checked by simply removing this stage and comparing the magnetically trapped atoms resulting. If needed, a Stern-Gerlach type of experiment can be carried out. By applying a strong magnetic field gradient before imaging, atoms with different magnetic spin are accelerated differently, with $m_F = 0$ not being accelerated, and $m_F = +1, +2$ and $m_F = -1, -2$ being accelerated in opposite directions. In this way, the population of each magnetic spin state can be extracted.

Once the atoms are trapped in the $|F = 2, m_F = +2\rangle$ state, and positioned in the centre of the magnetic trap potential, the Z shaped understructure path is driven with 80 A and the X-Bias coils with 28 A, giving an axial trapping frequency of $2\pi \cdot 17.9$ Hz and a radial trapping frequency of $2\pi \cdot 77.8$ Hz. No Y-Bias field is used at this point to keep a high trap bottom for the transfer. This transferring process, when optimised, has a typical transfer efficiency of $\approx 70\,\%$ and a final mean temperature of $\approx 120\,\mu$K.

3.6.1 Evaporative cooling

The magnetic trap stage is used to achieve further cooling below the MOT cooling limits. For many experiments, the goal of this stage is to get a cold thermal cloud of a few tens of micro-Kelvin. In the case of the experiment described here, the goal of the magnetic trap stage is to achieve a low enough temperature for the atoms to be transferred into the atom chip trap. This is realised after the so called

evaporative cooling procedure. Additionally, the Phase-Space Density (PSD) of the cloud is increased by a few orders of magnitude.

Evaporative cooling is a procedure in which the hottest atoms are removed from the sample, leaving only the coldest atoms in the trap and, effectively, reducing the overall temperature of the sample. This is carried out via Radio Frequency (RF) evaporation. Starting with a cloud of atoms trapped in the $|F = 2, m_F = +2\rangle$ state, fig. 3.15, frequency ν_{RF} is applied to the sample of atoms. When $g_F \mu_B |B| = h\nu_{RF}$, atoms experience a resonance between different magnetic spin states separated by $h\nu_{RF}$ (green lines in fig. 3.15), thus linking these states. Atoms that reach the truncation energy $\epsilon_t \propto k_B T$, will be automatically transferred to the $|F = 2, m_F = +1\rangle$ state, followed by a transfer to the $|F = 2, m_F = 0, -1, -2\rangle$ non-trapping states. In this way, these hot atoms with energy greater than the truncation energy, ϵ_t, are removed from the trap. The truncation energy is given by

$$\epsilon_t = 2h(\nu_{RF} - \nu_0), \tag{3.5}$$

where $\nu_0 = 0.70\,\mathrm{MHz\,G^{-1}}$ corresponds to the separation of the energy level at their trap minimum.

The cloud of atoms then re-thermalise again to a Maxwell-Boltzmann distribution. The RF frequency ν_{RF} is gradually reduced, evaporating the hottest atoms of this re-thermalised cloud. The truncation parameter, η, determines the efficiency of the evaporative cooling process, and is a measure of how far into the energy distribution the RF cut is. This parameter is given by

$$\eta = \frac{\epsilon_t}{k_B T}, \tag{3.6}$$

and, for optimal efficiency, has to be kept constant at a value of ≈ 7 throughout the whole evaporative cooling process. This determines the speed at which the evaporative cooling process has to be carried out. If the process is too fast, the truncation parameter rises dramatically. In this experiment, the evaporative cooling stage is typically 10 s long.

An interesting experiment that helps to explain this process is the RF knife. In an RF knife measurement, the atom number is measured as a function of the

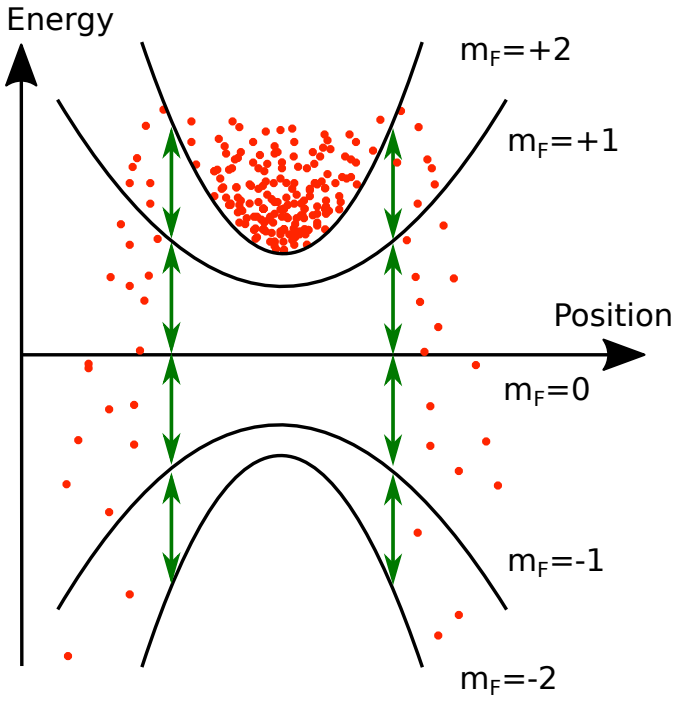


FIGURE 3.15: Evaporative cooling scheme. Black curves show energy versus position of the atoms for $m_F = -2, -1, 0, +1, +2$ sublevels. With all the atoms initially trapped in the $|F = 2, m_F = +2\rangle$ state, the applied frequency addresses the hottest atoms, removing them from the trap, and effectively cooling the sample. Atoms are represented with red dots, and the induced energy transitions with green lines.

RF frequency, ν_{RF}, applied. It can be deduced from fig. 3.15 that the number of atoms will be lower for lower ν_{RF} values. When the trap bottom is in resonance with the RF frequency applied, i.e. $h\nu_0 = h\nu_{RF}$, all the atoms are removed from the trap. But for $h\nu_0 > h\nu_{RF}$, none of the atoms are addressed and they all remain trapped. Figure 3.16 shows an example of this type of measurement. This technique is used to optimise the evaporative cooling process. The trap bottom can be easily extracted by finding the frequency at which the graph goes from maximum atom number to zero atom number. Note that the sharpness in this change is given by the linewidth of the RF frequency applied. The larger the linewidth of the frequency generator, the larger the frequency range addressed at each single point in time. RF knife measurements are essential to optimise the power of the radio frequency signal. A low signal power results in the cloud not being completely addressed when $h\nu_0 = h\nu_{RF}$, and the graph not reaching the zero value at any point. A high power results in the signal addressing atoms at different frequencies, producing an extended zero line around the trap bottom (near 0.8 MHz in fig. 3.16).

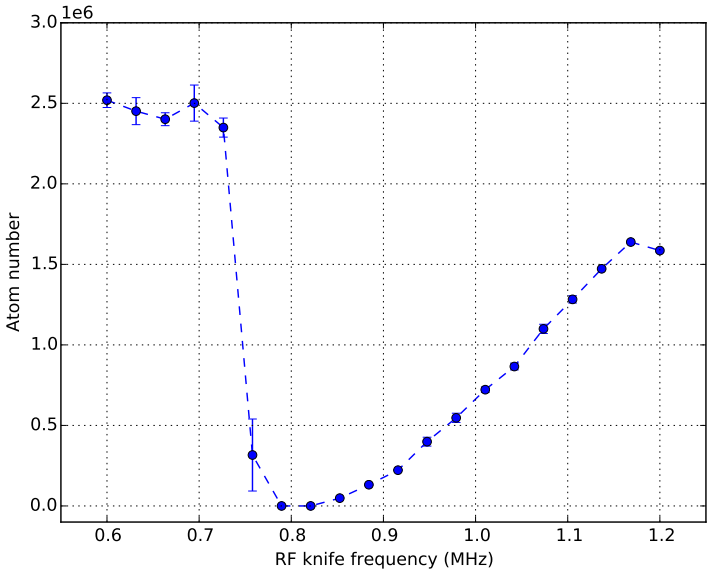


FIGURE 3.16: Radio Frequency (RF) knife measurement. The RF frequency is scanned, to address different trap frequencies. This type of measurement is performed in order to optimise the RF cooling. Power and linewidth of the RF signal are factors affecting the shape of this graph, therefore helping to optimise them. The height of the trap bottom can also be easily extracted from the sharp change in atom number.

The radio frequency signal is sent to the atoms via an antenna. This can be implemented in different ways. The closer the antenna is to the atoms, the better the efficiency of the system. For this reason, in this experiment, the radio frequency generator system is connected to two of the legs of the "H" shaped understructure piece (fig. 3.5), forming a "U" shaped antenna that emits the radio frequency in the central part of the "H", directly below the cloud of ^{87}Rb. The signal is typically ramped linearly from a value of 20 MHz to a value of ≈ 0.8 MHz, very close to the frequency of the bottom of the trap, in a time-scale of 15 s. In the last 4 s of the ramp, the slope of the ramp is usually flatter, ensuring the truncation parameter is kept close to its ideal value of 7.

Along with the gradual change in the Radio Frequency applied, adiabatic compression of the cloud is carried out. The confinement of the trap is progressively changed along with the frequency of the trap, increasing the density of the cloud of atoms and, therefore, also increasing the rate of elastic collisions that determine the re-thermalisation speed. The amount of compression is limited by three-body losses.

The ultimate purpose of the magnetic trap stage, with the compression and evaporative cooling processes, is to increase the Phase-Space Density (PSD). The PSD is a measure of the atomic density of the cloud of atoms. It typically starts at a value of $\approx 10^{-22}$, going up to $\approx 10^{-8}$ by the start of the evaporative cooling and, ultimately, reaching condensation at a value of 1.202. The PSD is given by

$$\text{PSD} = n\lambda_{dB}^3, \tag{3.7}$$

where n is the density of atoms derived from the peak OD, and

$$\lambda_{dB} = \frac{h}{\sqrt{2\pi m k_B T}} \tag{3.8}$$

is the thermal *de Broglie* wavelength. PSD is therefore determined by the number of atoms, the frequency of the trap at each step in the compression and the temperature of the cloud, emphasizing the importance of both the adiabatic compression and the evaporative cooling processes. Figure 3.17 shows the change in atom number and temperature throughout an example of evaporative cooling, in which the BEC transition line (see eq. (2.27)) is represented in red in fig. 3.17. Note that if the slope of the graph is too large, condensation is never reached.

The purpose of the magnetic trap stage in this experiment is to reach low temperatures before transferring the thermal cloud to the atom chip. Evaporative cooling in the magnetic trap in this setup is usually stopped at 20 µK, which results in $\approx 100\,\%$ transfer efficiency to the atom chip trap. Nevertheless, condensation is achievable and was observed in this trap by further cooling the sample.

The understructure used in this experiment is also a very useful tool to modify the shape of the sample of atoms. Using only the "H" shaped structure for creating the trapping potential, opens up the possibility of using the sidebars (red in fig. 3.5b) to modify the aspect ratio of the trap. Additionally, the combined use of the understructure and the atom chip is possible. The use of two wires of the chip running parallel to the legs (vertical sections of the wire in fig. 3.20a) of the Z trap, gives the ability to easily modify the aspect ratio of the trap, reaching aspect ratios of up to 40 in this type of trap. These elongated traps showed characteristics of density modulated BECs arising from in-trap phase fluctuations, discussed in detail in section 4.2.

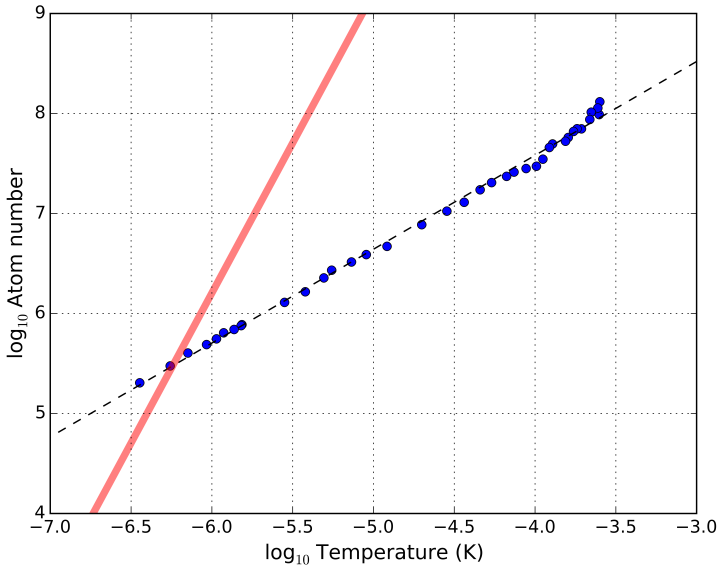


FIGURE 3.17: Measurement of atom number and temperature throughout the evaporative cooling process. The Phase-Space Density (PSD) increases during this process from a value of $\approx 10^{-8}$ to ≈ 1, with condensation happening at PSD = 1.202. The red line represents the BEC transition line, at which the cloud condenses. The slope of the data points is represented by a black dashed line. The efficiency of the process is determined by the slope of this data: if the slope is too large, condensation does not happen.

3.6.2 Lifetime measurement

In order to reach the desired temperature and PSD, the lifetime of the magnetic trap has to be sufficiently long (or the collision rate has to be high enough) to apply an effective evaporative cooling procedure. The lifetime is measured by measuring the number of atoms remaining in the trap with respect to the time of the trap. It is determined by the loss rate, with the atom number decaying exponentially according to

$$N = N_0 e^{-\frac{t}{\tau}}, \tag{3.9}$$

with t being the time of the trap, N_0 the initial atom number, and τ the lifetime of the trap. Figure 3.18 is an example of this type of measurement, in which a magnetic trap lifetime of $\tau = 9.3\,\mathrm{s}$ was achieved. This example of lifetime measurement was taken prior to the incorporation of the 2D MOT stage, which critically increased this value to $\approx 20\,\mathrm{s}$ by reducing the background gas pressure present in the magnetic trap stage.

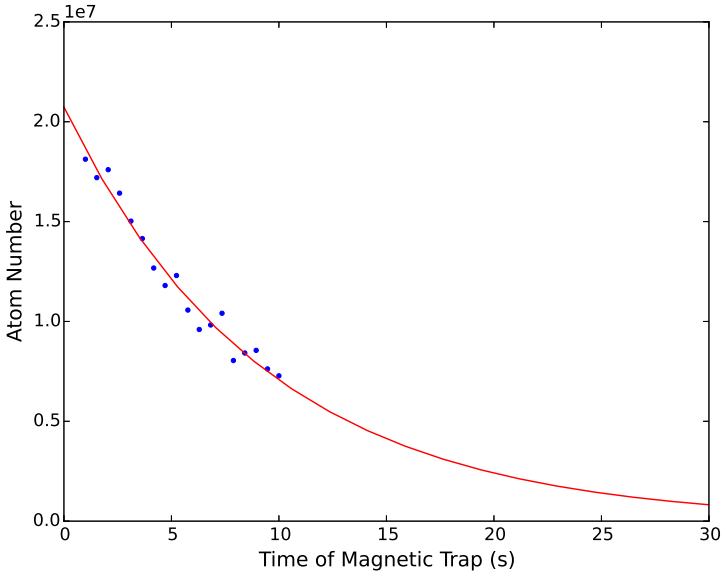
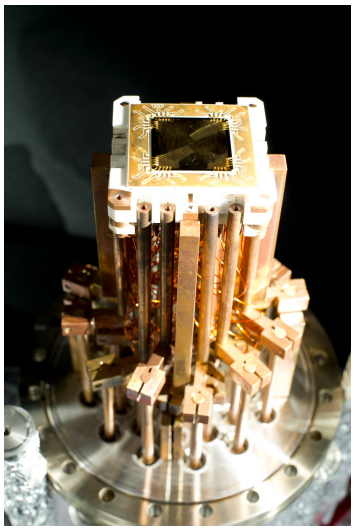


FIGURE 3.18: Lifetime measurement of the magnetic trap prior to the incorporation of the 2D MOT stage. Lifetime measurements are very important to determine whether evaporative cooling is possible. The lifetime in this example is $\tau = 9.3\,\mathrm{s}$, and proved the necessity to increase it, by reducing the background gas pressure with the addition of the 2D MOT.

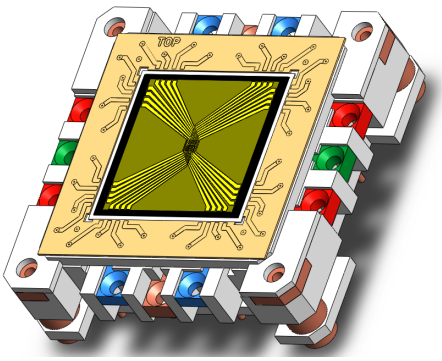
3.7 Atom chip

Similar to the magnetic trap described in the previous section, the atom chip is also a purely magnetic trap system. It is based on the same principles of trapping, and addresses the same magnetic spin state $|F = 2, m_F = +2\rangle$ of the atoms. With the dimensions of the chip being in the micrometre range, this stage requires an already cold and dense cloud of gas of a few microkelvin. The imperfections in the atom chip are in the nanometre range, resulting in smoother and more accurate magnetic fields than in the macroscopic trap when close to the conductors. The chip used in this setup is shown in fig. 3.19. The trapping potentials generated by this atom chip are described in detail in section 5.2.

The current carrying wires in the atom chip are all bonded to a PCB board that surrounds the chip, and acts as a connection point to the spring loaded copper rods that are then connected to the vacuum feedthrough flange. Wire bonding is a very delicate technique that requires "clean room" facilities. It is performed prior to installation of the chip, and was done using a microscope connected to a robot. Thin gold wires are attached to the connecting pads of the chip and to the pads on the PCB. Each electrical connection is realised with around 25 gold

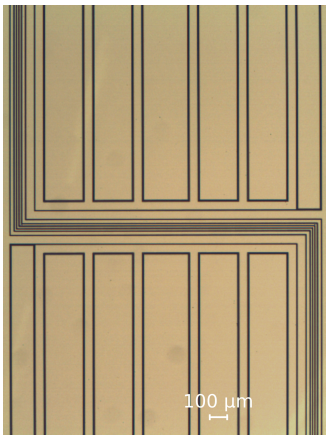


(a) Atom chip.

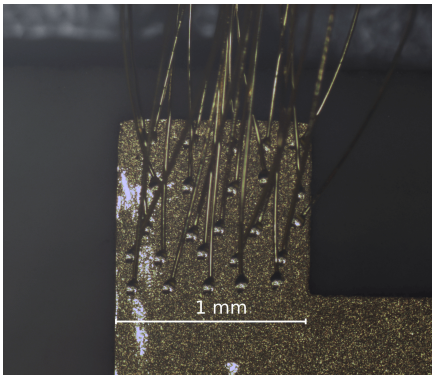


(b) CAD drawing.

FIGURE 3.19: Atom chip used in the setup. The chip is held in place using a 70×70 mm boron-nitride holder (white) that screws on top of the understructure. Wires are connected to the PCB board that surrounds the chip and is placed in contact with spring loaded copper rods. The rods are then electrically connected to the outside of the vacuum chamber via a feedthrough.



(a) Atom chip.



(b) Wire bonding.

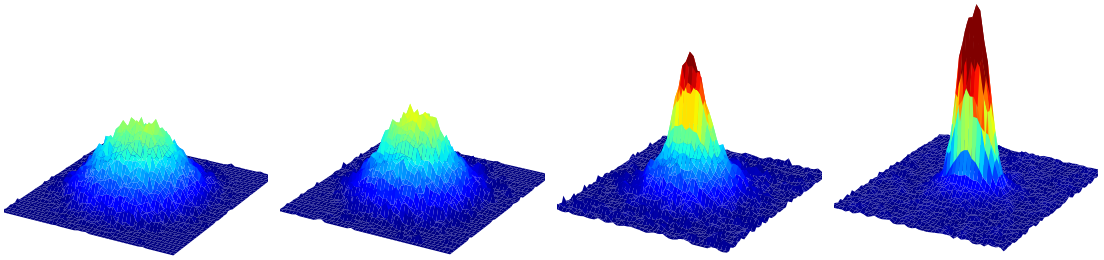
FIGURE 3.20: Micrographs of the atom chip. The central Z shaped current carrying wires and the additional lateral U shaped wires can be seen in the optical micrograph in (a). The optical micrograph in (b) is an example of the wire bonding needed to electrically connect the atom chip to the surrounding PCB board.

wires, shown in fig. 3.20b, ensuring that, together, they withstand currents of up to a few Amps.

3.7.1 BEC on the atom chip

Loading atoms into the chip trap is done from the macroscopic magnetic trap, with the transfer found to be optimum when performed at a temperature of 20 µK. The transfer efficiency at this stage is $\approx 100\,\%$, with very small atom loss. It is performed after stopping the evaporative cooling process, and is typically realised in 300 ms. The process starts with a linear ramp of the current through one of the Z shaped wires of the chip, shown in fig. 3.20a, to a value of 1 A. At the same time, the X-Bias coils are ramped down to a much smaller magnetic field value of a few Gauss. The Y-Bias field used to control compression and the trap bottom in the previous step is ramped down to zero. Note that the direction of travel of the current in the Z wire has to be the same as the one in the macroscopic magnetic trap, so that the homogeneous X-Bias field required points in the same direction. At 60 ms after starting the transfer, the ramping down of the Z shaped copper track from the macroscopic magnetic trap starts.

By the end of these ramps, the atoms are trapped in the atom chip trap, and further cooling is resumed. The induced Radio Frequencies (RF) in this stage of the evaporative cooling process also originate from the understructure copper track acting as an antenna. The purpose in this phase of the experiment is to achieve a PSD of 1.202, resulting in condensation of the sample of ^{87}Rb. The length of this stage is again dictated by the lifetime of this trap, and by the η parameter (see section 3.6.1) being close to 7 throughout the ramp. The optimum timescale for the ramps in the chip trap was found to be between 2 s and 3 s in length, resulting in the generation of BEC. Figure 3.21 shows how the cloud peak Optical Density (OD) dramatically increases in the final few tens of kHz of the RF ramp, with the BEC starting to appear in the centre of the thermal distribution (fig. 3.21c), and ending in an almost pure condensate with very little thermal cloud (fig. 3.21d). Figure 3.22 is an example of the OD integrated in the radial direction and fitted to a bimodal distribution containing a thermal Gaussian part and a condensed Thomas-Fermi part (see section 2.3).



(a) 688 kHz. (b) 678 kHz. (c) 668 kHz. (d) 658 kHz.

FIGURE 3.21: Formation of a Bose-Einstein condensate (BEC) in the final part of the evaporative cooling procedure. The condensed part can be seen appearing in the central part of the thermal cloud in (b) and (c), and progressively increasing to form an almost pure BEC in (d). The BEC atom number is $\approx 10^5$ and the temperature is $\approx 500\,\text{nK}$. The frequencies represent the final Radio Frequency (RF) applied during the evaporative cooling.

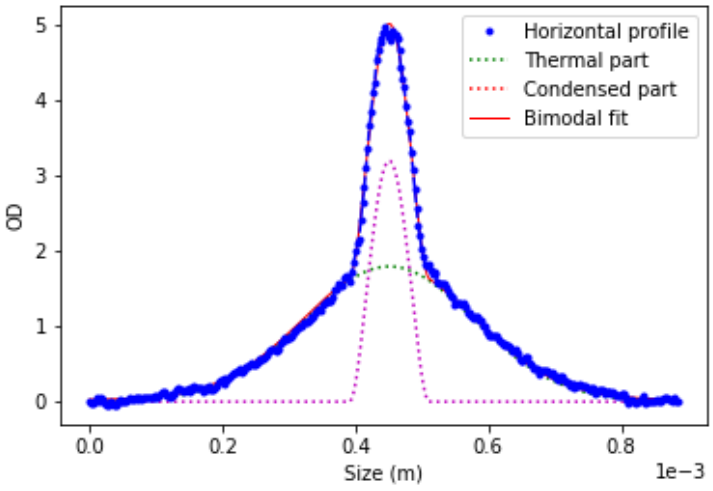


FIGURE 3.22: Example of bimodal fitting (red curve) of the integrated Optical Density (OD) (blue circles) of a BEC formed in the atom chip trap. The condensate, described within the Thomas-Fermi approximation fit (red dotted curve), can be clearly distinguished from the thermal Gaussian part (green dotted curve). From this type of fitting, parameters such as atom number and size of the condensate can be extracted.

3.7.2 Trapping frequencies and aspect ratio

In order to achieve full understanding of the physics behind an experiment, it is essential to be able to measure and control each and every physical parameter present in the experiment. In a cold atom experiment, some of the most important variables are determined by the trapping frequencies, which are the frequencies at which the atoms oscillate in each of the trap directions. These drive the interatomic interactions and, therefore, determine how the atoms interact with each other. For the majority of the experiments carried out, a simulation of the trapping frequencies can be carried out starting from the currents delivered to each of the trapping structures and wires in the system. While this gives a fast and relatively accurate result, to determine the frequency more accurately it has to be measured experimentally.

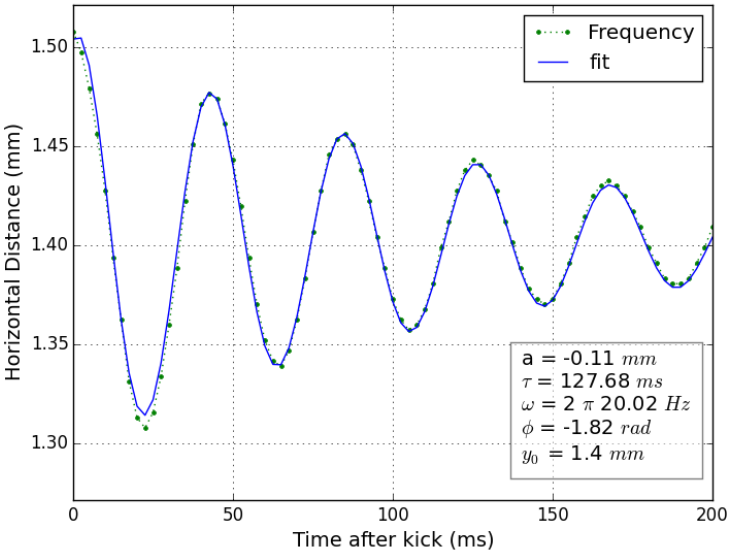
The frequency of the trap determines the vibration of the atoms inside it. For this reason, the frequency is calculated from the motion of the atoms. To be able to visualise this motion, the best route is to induce a perturbation in the magnetic potential. This perturbation, or quench, is either first added and then switched off rapidly or first removed and then switched on rapidly, allowing for the atoms to recover their initial position in space, resulting in an oscillatory damped motion that can be imaged and adjusted to a damped harmonic oscillator model of the form

$$y = ae^{-\frac{t}{\tau}} \cos(\omega t + \phi) + y_0, \tag{3.10}$$

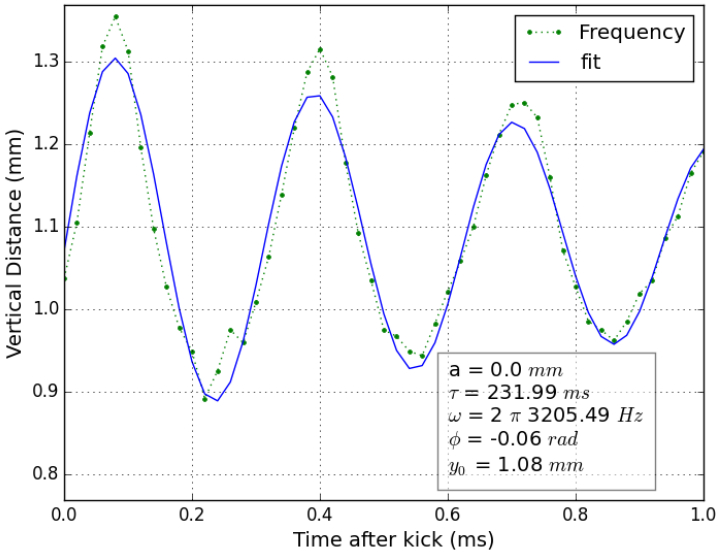
where τ is the decay, a is the amplitude, ϕ is the shift, y_0 is the offset and ω gives the angular frequency of the trap, which is typically around a few hundred hertz.

For this setup, in the stage of magnetic trap prior to the atom chip trap, the most reliable method was to induce the perturbation in either the Z shaped structure or the coils. During the chip trap stage, the perturbation was easily added by small changes in the currents of certain wires. This ability to rapidly manipulate currents with a very low inductance feedback from the system is a well known characteristic of atom chips. For measuring the radial component of the frequency, the perturbation was induced on the main Z shaped trapping wire and, for measuring the axial component of the frequency, the aspect ratio of the cloud was modified by applying currents to two wires that add (or remove) magnetic field to the legs

(vertical sections of the wire in fig. 3.20a) of the Z wire. This procedure is particularly useful to measure the aspect ratio of the cloud, λ. Knowing the aspect ratio is of extreme importance when studying the physics of a quasi-1D system, or 3D elongated system.



(a) Axial frequency.



(b) Radial frequency.

FIGURE 3.23: Axial and radial measurements of the trapping frequencies for an extreme aspect ratio value of 160, obtained by displacing the cloud of atoms closer to the surface of the chip ($\approx 10\,\mu$m), at a time-of-flight of 1 ms. Frequencies are measured by inducing a perturbation kick on the system and analysing the oscillation pattern arising.

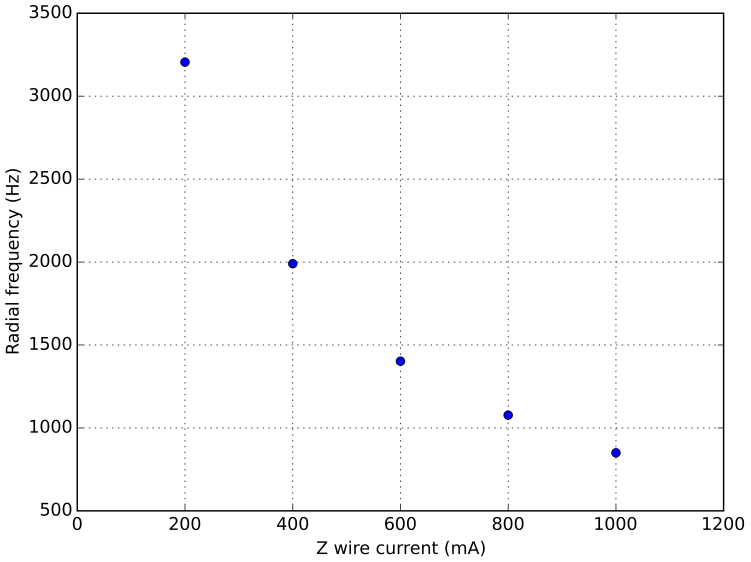


FIGURE 3.24: Radial frequency of the trap versus current in the Z shaped trapping wire.

The aspect ratio of the trap can be easily modified by pushing the cloud closer to the surface, which changes the radial frequency, by suppressing or enhancing the effect of the legs of the Z wire, which changes the axial frequency, or by a combination of both. The cloud can be moved closer to the surface by altering the ratio between the current through the Z wire and the current through the coil that induces the bias field used for trapping. The effect of the legs of the Z wire is modified either by changing the current through the coil that creates the additional bias field used to raise the bottom of the trap, or by altering the current through wires that run parallel to the legs of the Z wire (see fig. 4.3a). Since the control of the currents through the atom chips is more manageable than through coils, modifying currents only on the chip is often the path chosen to measure trapping frequencies in these experiments. In order to maintain the same temperature of the cloud with the same evaporative cooling procedure, the trap bottom has to be adjusted for each configuration of currents.

The aspect ratio of the cloud can be easily modified to achieve values ranging from $\lambda = 26$ to an extreme $\lambda = 160$ (see fig. 3.23a and fig. 3.23b). Figure 3.24 shows the large effect that the distance to the surface has on the radial frequency. A lower Z wire current means that atoms are trapped closer to the surface. This greatly helps with the study of quasi one-dimensional physics and effects like phase fluctuations, explained in more detail in section 4.2.

3.7.3 BEC lifetime in a chip trap

Once the cloud of ^{87}Rb atoms has condensed into a BEC, and it has been fully characterised, experiments with the BEC can start. For this, it is important to be able to keep the BEC in the trap for sufficient time, ensuring that realisation of the experiments is plausible. At this stage, the forced RF cooling has been stopped, and the BEC sits in the atom chip magnetic trap. During this time, the sample starts slowly heating up and, although the lifetime of the cloud can be long enough for experiments, the cloud may not remain condensed for that time. In order to ensure that the condensate is maintained during this time, an RF shield, or RF knife, is employed. Keeping a constant RF frequency equal to that used for the final value of the evaporative cooling ramp ensures that atoms heating up above the corresponding trap height will be expelled from the trap, following the scheme represented in fig. 3.15. In this way, the BEC is maintained for longer, but atoms are lost from it. Figure 3.25 shows the lifetime curve measured with the peak Optical Density (OD). Peak OD is a parameter that characterises the BEC. The higher the peak OD, the more likely it is that condensation is present. The lifetime of the BEC shown in fig. 3.25 increases dramatically with use of the RF knife.

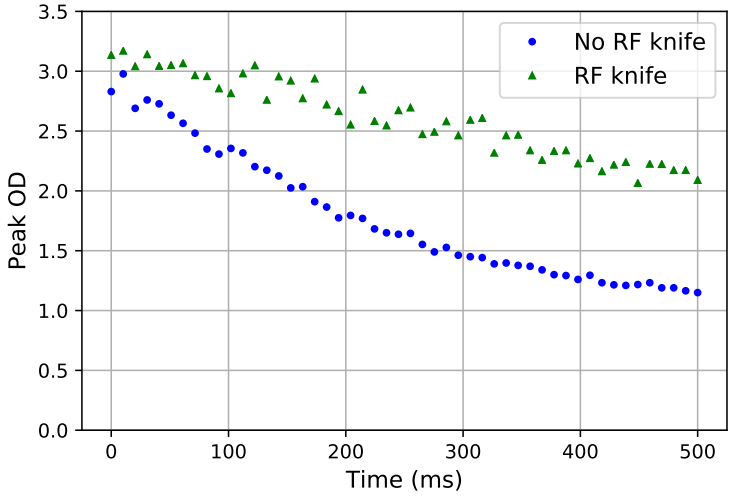


FIGURE 3.25: Example of a Bose-Einstein condensate (BEC) lifetime measurement showing peak OD of the sample measured over a standby period with (green triangles) and without (blue circles) an RF knife. The RF knife BEC lifetime increases when applying a constant RF frequency, effectively capping all the atoms that heat up in the trap, maintaining the BEC for a few hundreds of milliseconds. The BEC lifetime is important for the realisation of experiments.

3.8 Imaging system

The imaging system is the most important source of information from the experiment. Therefore, a careful design and implementation is essential. The setup described in this document contained an ImagingSource DMK-21BF04 CCD sensor camera, with a pixel size of 5.6 µm and a resolution of 640 × 480 pixels. This camera gave sufficient resolution for a MOT stage and even for magnetic trapping of thermal atoms. Unfortunately, the quality and noise level of the camera was not sufficient for imaging a BEC.

A new imaging system was implemented, with a state of the art Andor iXon3 888 CCD sensor camera, with a pixel size of 13 µm and a resolution of 1024 × 1024 pixels. The camera, along with all the optics, was mounted on an optical board, shown in fig. 3.26, and on top of a three way translation stage. The magnification was chosen to be 5, using two lenses, L_1 and L_2, with focal length $f_1 = 150\,\text{mm}$ and $f_2 = 750\,\text{mm}$, placing L_1 closer to the target and L_2 closer to the camera (see fig. 3.27). This configuration gave a good resolution of the BEC, enabling more accurate experimental measurements. The only drawback was that, for aligning the MOT, this configuration is not useful. For this reason, a more complex system was developed, in which both cameras, ImagingSource and Andor, can be swapped rapidly without any alignment needed. Leaving L_1 unchanged for both setups, L_2 determines the magnification and position of the camera. Figure 3.26 is a SolidWorks drawing of the setup with the Andor camera in place on the right. A section of tube containing lens L_2 is attached to it and, on the left part of the drawing, a mirror redirects the light after passing through L_1. Swapping to the ImagingSource is as easy as removing a section of tube and sliding it in the central supporting pillars shown in the drawing. With L_2 for the ImagingSource setup having a focal length of $f_2 = 75\,\text{mm}$, the system can rapidly swap from a magnification of 5 to a magnification of 0.5 for alignment. The whole imaging system is slightly tilted to avoid L_1 and the surface of the UHV window to be parallel to each other, which would produce interference due to coherent reflection of light on both surfaces.

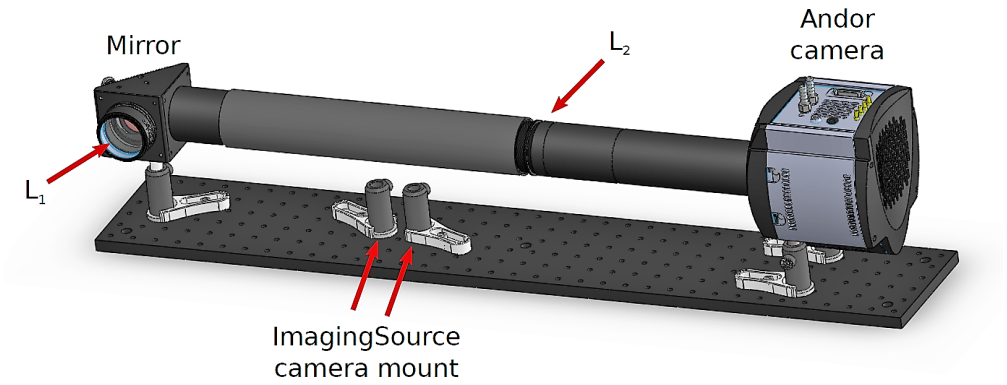


FIGURE 3.26: CAD drawing of the imaging system employed in the laboratory. On the left side, there is the L_1 lens together with a mirror. The mirror was added due to space constraints of the room and the optical bench. In the middle section, two free supporting pillars are placed to host the ImagingSource camera with a different L_2 lens integrated in it, used for MOT alignment. The Andor camera along with the L_2 lens is shown in the right side of the drawing.

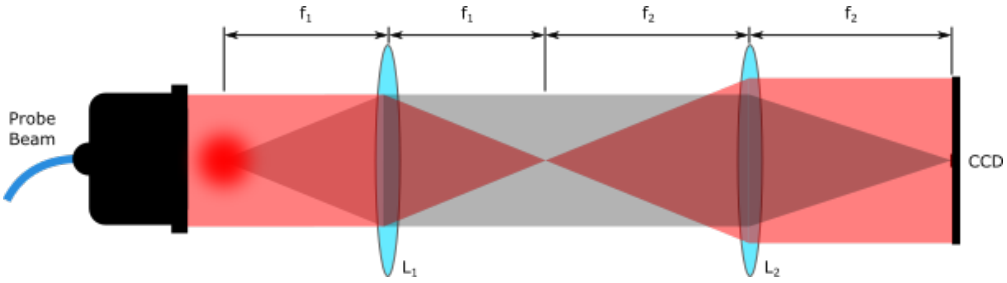


FIGURE 3.27: Absorption imaging scheme showing the imaging beam emerging from the polarisation maintaining fibre on the left. The light interacts with the atoms, represented by a red circle, and the attenuated light then travels through two lenses and is focused into the CCD chip of the camera. The focal length and position of the lenses is of high importance and the ratio between focal lengths determines the magnification of the system.

3.8.1 Absorption imaging

Experiments are realised by interrogating the sample. Atoms are typically imaged using the absorption imaging technique. For this, light and magnetic fields used for trapping have to be eradicated beforehand. External magnetic fields greatly affect the imaging, since they alter the energy levels of the atoms, splitting them and upsetting the absorption of photons coming from the imaging beam. To make sure no fields are present during imaging, data are always acquired after some ballistic expansion time, or time-of-flight (TOF). The shortest TOF before taking reliable data is 1 ms in the magnetic trap.

The image obtained in absorption imaging is extracted from the attenuation of the imaging light that the atoms create. An oncoming resonant laser beam shines on the sample, creating a shadow that is imaged on the CCD detector of the camera. This shadow is generated when the atoms absorb the oncoming photons. For this reason, it is a destructive method, since the cloud is heated considerably in the process. The propagation of a beam of intensity I_0 along the z direction is given by the Beer-Lambert law [15]

$$I(x,y) = I_0(x,y)e^{-OD(x,y)}. \tag{3.11}$$

The OD is defined as

$$OD(x,y) = \sigma n(x,y), \tag{3.12}$$

where the density of atoms is integrated along the path of the beam

$$n(x,y) = \int n(x,y,z)\mathrm{d}z, \tag{3.13}$$

and the photon-atom scattering cross-section is given by

$$\sigma = \frac{\sigma_0}{1 + (2\delta/\Gamma)^2 + I/I_{sat}}. \tag{3.14}$$

When the light is on resonance ($\delta = 0$), the cross-section is defined by

$$\sigma_0 = \frac{\hbar\omega\Gamma}{2I_{sat}}. \tag{3.15}$$

The saturation intensities can be found in the *Rubidium 87 D Line Data* [64].

Light from a polarising maintaining fibre is collimated and shone onto the atomic sample. With the light being resonant with the $|F = 2\rangle \rightarrow |F' = 3\rangle$ transition, atoms will absorb these photons and re-emit them in random directions, effectively creating a "shadow", as seen in fig. 3.27. Although not essential, repumping light is also added during this pulse to repump any atoms that fall into the dark state.

In the experiment described here, the light (and shadow) will then hit the atom chip, reflecting from it before reaching the L_1 lens.

The common absorption imaging procedure involves taking three consecutive images, with a temporal separation of $\approx 100\,\text{ms}$, and is illustrated in fig. 3.28 for MOT imaging using the ImagingSource camera. The first image contains the atoms and, therefore, the shadow that they create through interaction with the imaging light. The second image is taken after the sample of atoms has escaped the trap, with the imaging and repumping beams both on. The third image is taken with both laser beams off, giving the background intensity I_{bg}. This background is removed from the first and second pictures, which are then compared to determine the region occupied by the atoms. The optical density shown in fig. 3.28d is then given by [81]

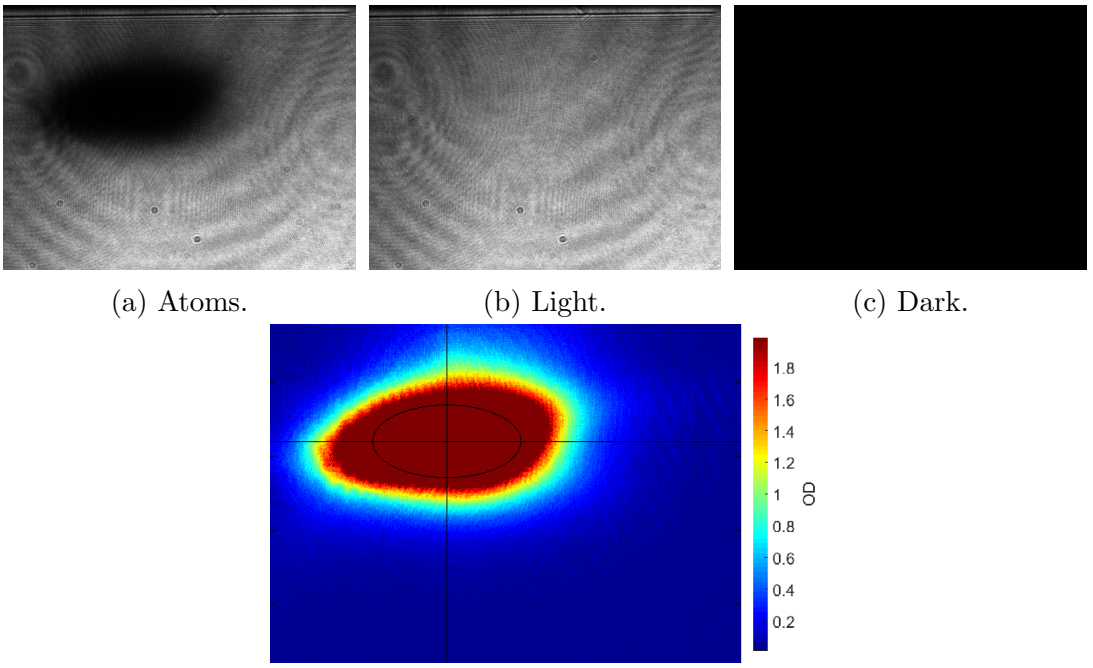
$$OD(x,y) = \frac{I_0(x,y) - I(x,y)}{I_{sat}} - \ln\frac{I(x,y) - I_{bg}(x,y)}{I_0(x,y) - I_{bg}(x,y)}. \tag{3.16}$$

The imaging beam pulse lasts for a few tens of microseconds, and its power is set to $\approx 1\,\text{mW}$ (intensity of $\approx 0.3\,\text{mW}\,\text{cm}^{-2}$), which was optimised by previous PhD student Dr. Gal Aviv [30] using the ImagingSource camera. The exact frequency shift applied with the AOM is found by performing a fine scan of frequencies to find the optimum value. This scan is then fitted to a Lorentzian function

$$L(x) = \frac{1}{\pi}\frac{\frac{1}{2}\Gamma}{(x - x_0)^2 + \left(\frac{1}{2}\Gamma\right)^2}, \tag{3.17}$$

where x_0 is the centre and Γ is the width.

Figure 3.29 is an example of one of these scans. This scan was performed to find the optimum imaging frequency. At that stage in the experiment, the optimum imaging frequency was found to be $212.4\,\text{MHz}$, with $\Gamma = 7.2\,\text{MHz}$. The imaging frequency is a very sensitive experimental parameter, since the absorption will be reduced with small drifts from the resonance frequency, leading to errors in the atom number calculation, temperature measurements, etc.



(a) Atoms. (b) Light. (c) Dark.

(d) Processed image.

FIGURE 3.28: Example of absorption imaging procedure, using the Imaging-Source camera on a MOT cloud of ^{87}Rb. Three pictures are taken for each absorption imaging process. (a) is the first picture showing the shadow of the atoms created through interaction with the imaging beams. (b) is the second picture for normalisation of the laser beams intensity without atoms. (c) is the third picture for capturing the background intensity. (d) is the processed image (see text for details).

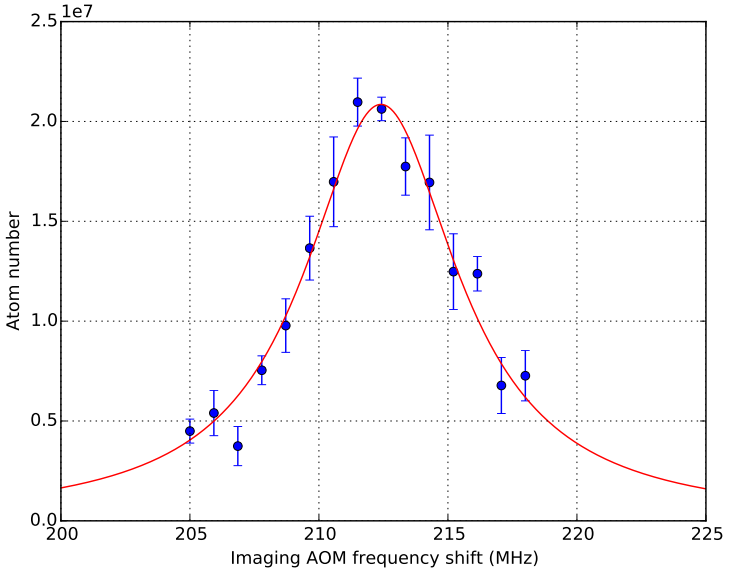


FIGURE 3.29: Imaging frequency scan showing the Lorentzian distribution (red curve) fitted to the measured data (blue circles and error bars). The peak of the distribution lies at 212.4 MHz, with $\Gamma = 7.2$ MHz.

3.8.2 Temperature measurement

The temperature of a thermal cloud of atoms can be extracted by analysing the change in size of the atomic cloud during ballistic expansion. The expansion of the cloud when released from its trapping potential is caused by the temperature of its particles. The expansion of the sample due to its temperature T is given by [82]

$$\sigma^2(t) = \sigma^2(0) + \frac{k_B T}{m} t^2, \tag{3.18}$$

with t being the time of flight, or expansion time, and $\sigma(t)$ the RMS width of the Gaussian profile of the cloud at time t. Figure 3.30 is an example of a temperature measurement carried out in the laboratory. The temperature is extracted by fitting the square of the measured radial (y) and axial (x) RMS widths versus the expansion time squared. This is a very reliable way of measuring the temperature of a sample of thermal atoms.

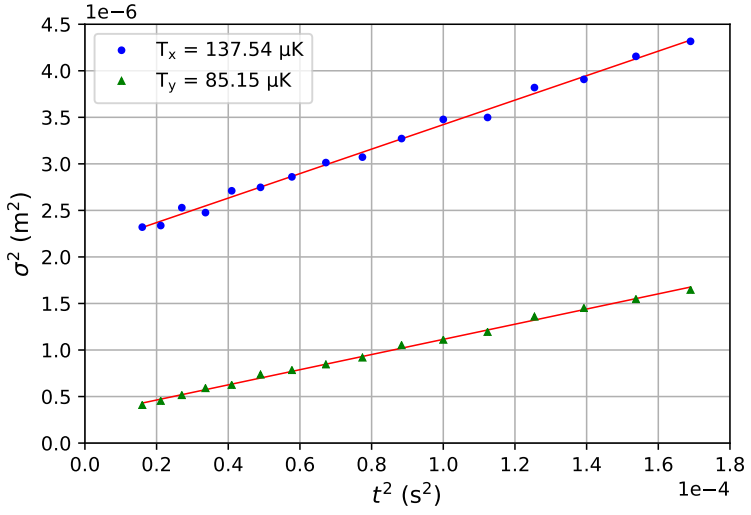


FIGURE 3.30: Example of the measurement of the width of the atomic cloud during ballistic expansion, at the end of the MOT stage. The temperature of the sample is extracted from the fits (red lines) of the measured axial (blue circles) and radial (green triangles) widths. A higher temperature causes the cloud of atoms to expand more rapidly.

3.8.3 Resolution focus and magnification

The whole imaging system was mounted on a three-way translation stage. This allows for centring of the image to the atoms. Its usual position is just below the line of sight of the chip but, for some experiments requiring long expansion times, the imaging system needs to be moved down to capture the falling atoms. The ability to move the entire imaging system closer or further away from the atoms facilitates the correct focusing of the camera. Additionally, the resolution of the imaging system was measured using a resolution test target, and found to be 10 µm. This is an important test in order to accurately measure small distances when running experiments.

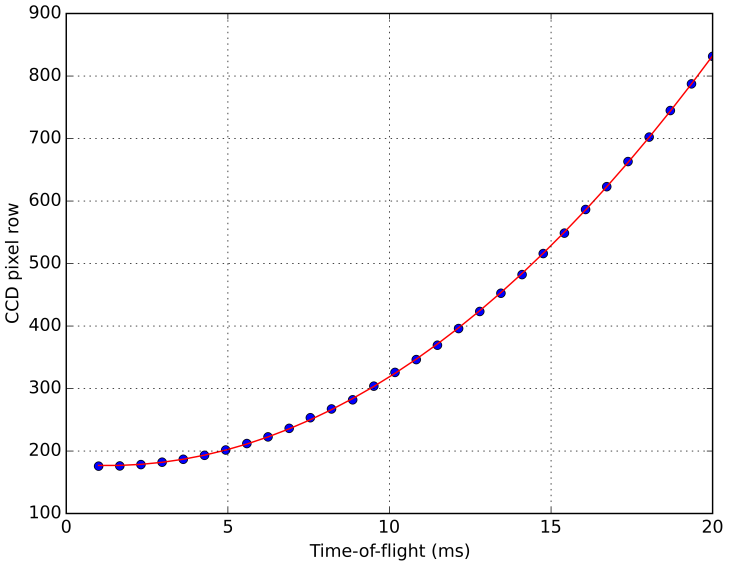


FIGURE 3.31: Magnification of the imaging system is extracted from the distance travelled by the atoms during ballistic expansion. The graph shows the measured mean position of the atoms (blue circles) in pixels using the Andor camera with the imaging system described in this section. The pixel size of the Andor camera is 13 µm. Red curve shows the best fit to the experimental data.

The main and most important source of information coming from the experiment is the absorption images extracted. Therefore, the more optimum an imaging system is, the more accurate the experimental results will be. The optimum parameters of the imaging system are calculated and set beforehand but, due to technical limitations and possible imperfection of components, the actual results can differ slightly from the calculated ones. Magnification is one of the most important parameters in the imaging system, since it affects calculations of atom number,

the size of the cloud and position of the cloud. In the setup with the Andor camera, the magnification was theoretically calculated to be 5. The most straight forward way of calculating this value is to measure a parameter linked to a known constant. Letting the sample fall due to gravity, and knowing that the pixel size of the camera is 13 µm, the magnification was measured to be 4.97 ± 0.04. Figure 3.31 shows the mean position of the sample during ballistic expansion, measured in pixels of the camera. For the ImagingSource camera, this magnification was found to be 0.49.

Chapter 4

Low-dimensional Bose gas in an atom chip

This chapter describes several experiments that can be performed using the setup described in previous chapters of this document. The full potential of an atom chip experiment is explained and experimentally realised. It is shown how the trap can be quenched and manipulated, thus altering the trapping potentials, aspect ratio and position of the atoms. The chapter is divided into three main sections; the quenching and manipulation of traps in an atom chip, the observed density fluctuations after ballistic expansion, and the microscopy of imperfections on the surface of the chip.

Two examples of experiments are described in section 4.1. First, in section 4.1.1, a cloud of cold ^{87}Rb is divided in two clouds with the aid of various chip wires. When using two parallel Z shaped wires, depending on the currents used, the cold cloud splits either vertically or horizontally. This experiment is also simulated in order to pre-determine the required currents. The results show splitting of the cloud in the vertical direction. With the present setup, only the vertical splitting can be imaged. The second experiment, in section 4.1.2, uses two additional side wires on the chip in order to perturb, or quench, the trap in which the cold atoms are sitting. Depending on the adiabaticity of the quench, a strong oscillation in the dimensions of the Bose gas can be observed.

Section 4.2 focuses on the effect that phase fluctuations have on the density of the cloud after some time-of-flight. A one-dimensional cold cloud exhibits thermal excitations over a specific range of frequencies, where these thermal excitations

alter the phase along the gas. In time-of-flight, these alterations can be visualised and characterised [83]. This section also shows the phase fluctuations dependence on the temperature of the gas.

In the last part of this chapter, it is shown how microscopy can be achieved with a cold atoms setup such as the one described in this document. Microscopy of one of the wires on the atom chip is achieved, realising the first step towards a functional BEC microscope, which is capable of microscopy at a nanometre scale.

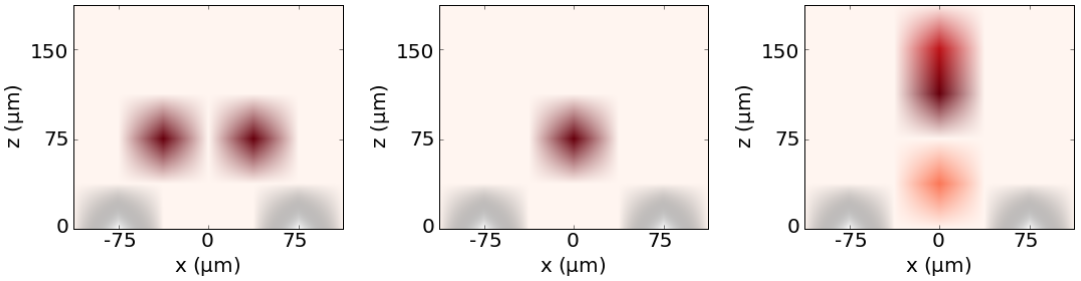
4.1 Quenching and manipulation of atom clouds in a chip trap

In order to understand the behaviour of the atoms at temperatures near absolute zero, and to be capable of using these systems for different applications, such as interferometry, it is necessary to acquire the ability to quench (rapidly change the shape of the trapping potential) and manipulate these gases of atoms inside the trap. The development of atom chips has greatly helped towards achieving a precise and controlled way of manipulating atomic traps. By using different wires with specific currents through each of them, one can quench or modify the trap in a desired way.

4.1.1 Splitting of a cold atom cloud

When it comes to the design of the layout of an atom chip, there are plenty of options available and plenty of examples in different groups. A common characteristic, though, is the addition of several wires running parallel to the main trapping wire. This feature facilitates the development of more complex experiments that require, for example, the use of RF dressing potentials or double-well potentials.

A double-well potential can be created by using two parallel current-carrying wires in the presence of a uniform bias field, and can be used as an interferometer [84]. Depending on the current that passes through them, keeping a constant bias field, the splitting is either vertical or horizontal, going from horizontal to vertical as the current increases. A simulation of this is shown in fig. 4.1. This splitting can



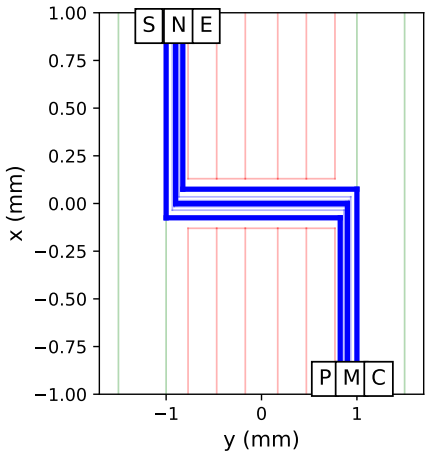
(a) $I < 400\,\text{mA}$. (b) $I = 400\,\text{mA}$. (c) $I > 400\,\text{mA}$.

FIGURE 4.1: Simulated splitting of the trapping potential in the xz plane using two parallel wires with current flowing along the y direction, and a constant X-Bias field. The two wires are positioned at $x = \pm 75\mu$m and the current flows in the same direction in both wires. The colour scale (arb. units) illustrates the position of the potential minima (dark red). For $I < 400\,\text{mA}$ (a) the two minima are separated horizontally. As I increses, the two minima gradually approach, merging at $I = 400\,\text{mA}$ (b). For larger current values, $I > 400\,\text{mA}$ (c), the two minima split in the vertical direction, with different values of the trapping potential minima.

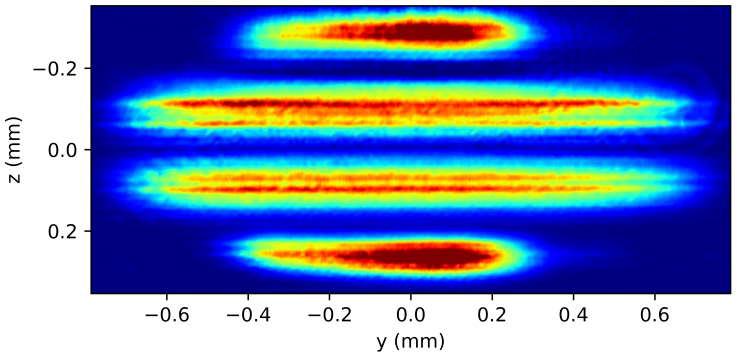
also be realised by keeping the same current in the wires and changing the X-Bias field.

In the experimental setup, the magnetic trap cooling stage is done partially by using the copper understructure, as explained in the previous chapter. For this reason, when the atoms are transferred to the chip, the experimental sequence has to be optimised for one of the wells, leaving the other one empty. The ultracold cloud of atoms is therefore first achieved in one of the two wells. After the cloud of atoms is prepared using just one of the wires (E-C or S-P), the current through this wire is ramped down to 400 mA at the same time as the other wire is switched-on and current through it is ramped up to 400 mA, in a time period of 50 ms. This allows for some of the atoms to spill onto the other well. The current through both wires is then ramped up simultaneously, in another 50 ms, to a value of 480 mA, which creates two clearly independent wells filled with atoms. Figure 4.2b shows the result of this process, using absorption imaging. In this image, four different regions can be distinguished, corresponding to the double-well and its reflection from the surface of the chip, as explained in the previous chapters.

The trapping potential and well depth in each well cannot be independently controlled, leading to an impossibility of controlling the population of atoms for each well. In this setup, there is no straightforward way of imaging the two horizontal wells, making vertical splitting the only option. For the vertical splitting, as the



(a) Chip schematic.



(b) Double well.

FIGURE 4.2: Double well produced by a combination of currents passing through two parallel Z-shape wires. Figure 4.2a shows the two wires used, E-C and S-P. Figure 4.2b is an average of a set of experimental images of the atom cloud density after 0.8 ms time-of-flight. The image is doubled, showing four regions with atoms, due to the mirroring effect of the chip, which is in a horizontal position in the middle of the picture. The well depths in each well are different, leading to a difference in atom number.

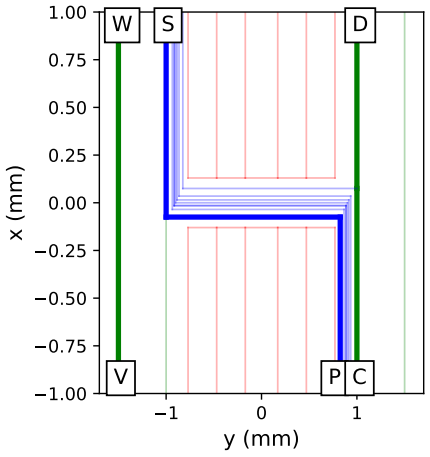
current through the wires is increased, the two potential wells that are formed have different minimum values. This leads to an imbalance in the atom population between wells, as well as a difference in the trapping frequencies of each of them (see fig. 4.1c).

The different values of the potential minima means that, in principle, the cloud would not be cooled down equally in both wells, ending up with different temperatures in each well and, most likely, a condensate in one but not the other. This problem could be addressed by a more complex evaporative cooling sequence, in which both wells would have to undergo the final cooling stage independently, using a different RF frequency ramp for each. Additionally, for this vertical splitting, the separation of the wells will always have to be comparable to the separation between the wires used. For this reason, interference between both clouds is very difficult. For these experiments, the closest possible separation between wells is $\approx 40\,\mu m$, which suggests that the time of flight for the clouds to overlap is in the order of tens of milliseconds. For this time of flight, the fringe spacing caused by interference would be smaller than the resolution of the imaging system (fringe spacing calculated in section 5.3), which is configured for a resolution of $2.6\,\mu m$ per pixel. The issue could be solved with a longer time of flight expansion, increasing the fringe spacing. Some experiments have been realised in which, using magnetic levitation, interference for large cloud separations can be imaged [85].

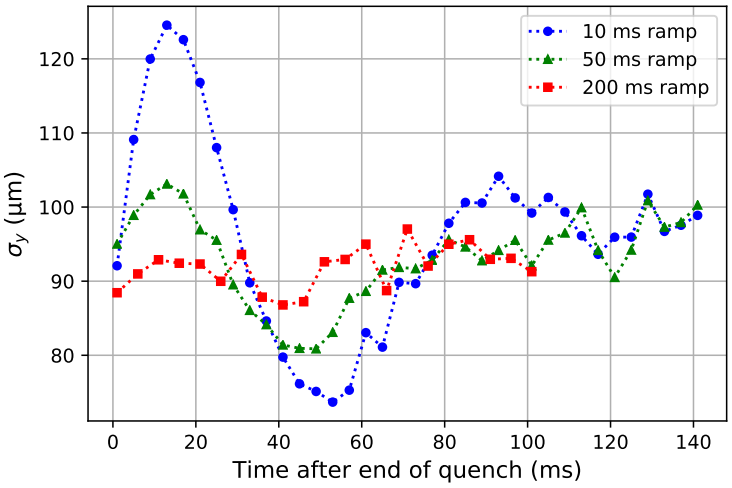
4.1.2 One-dimensional quench

When modifying a trapping potential it is important to know whether the transition is adiabatic or non-adiabatic. In other words, to know whether the atoms are able or not to follow the change in the potential. In an adiabatic transition, atoms follow the change, and the PSD of the cloud remains constant during and after the transition. On the other hand, if it is a non-adiabatic transition, the PSD of the cloud will change together with other characteristics of the cloud, i.e. the aspect ratio of the cloud of atoms.

As a rule of thumb, any change in the trapping potential undergone in a shorter time-scale than the trapping frequency will be non-adiabatic. This means that, in order to keep the PSD constant, the change in trapping potential should be slower than the trapping frequency.



(a) Chip schematic.



(b) Quench of the trap for different ramp times.

FIGURE 4.3: Breathing modes of cold atoms in a chip trap. Figure 4.3a shows the wire configuration used for this experiment, with current flowing in the S-P trapping wire and the change in aspect ratio realised with current flowing through wires W-V and D-C in (a). Figure 4.3b shows the change in axial size of the atom cloud after different ramping times of the current flowing through wires W-V and D-C. The size is shown as σ_y, value extracted from the Gaussian fit of the atom density in the axial direction after 17 ms of time of flight. A non-adiabatic transition happens for 10 ms (blue circles) and 50 ms (green triangles) ramp times, where breathing modes are clearly seen. An adiabatic transition happens for a 200 ms (red squares) ramp time, where there are no breathing modes seen in the system.

A very interesting effect produced by a non-adiabatic change in the trapping potential in a very cold cloud of atoms is known as breathing. Starting with a low temperature system, a quench in the trapping potential is induced, this results

in a sharp change in the magnetic potentials of the trap. The atom cloud tries to follow this change but, if the change is faster than the trapping frequency, it starts "breathing". The atoms will expand and contract rhythmically, resembling the breathing of an animal [86].

Atom chips are great tools for studying quench experiments. In this experiment, the use of two side wires helped by inducing a rapid change in the trapping potential along the axial direction of the trap. The wires used for this experiment are shown in fig. 4.3a. Current along these wires was ramped-up to the desired value. The speed of this ramping determined the adiabaticity of the transition. In fig. 4.3b it can be seen how this breathing decreases the more adiabatic the process is. In this experiment, the axial frequency is changed from $2\pi \cdot 20\,\mathrm{Hz}$ to $2\pi \cdot 23\,\mathrm{Hz}$, with an initial temperature of $1\,\mu\mathrm{K}$. The cloud is then held in the trap and the change in size is analysed. The atom number decreases due to the lifetime of the trap, and the size increases due to heating of the cloud. The rapid decay is due to a high temperature of the cloud and possibly cross-coupling between dimensions.

The manifestation of breathing modes during non-adiabatic quenches has also been studied theoretically using the numerical tools described in detail in chapter 6.

4.2 Low-dimensional behaviour of a BEC

Low-dimensional cold clouds have always attracted lots of attention from researchers [87]. The quantum behaviour of the atoms when placed inside a low-dimensional anisotropic trap gives rise to some interesting physics. One of the most well known and, probably, least understood phenomena, is phase fluctuations. Phase fluctuations were first seen shortly after the realisation of the first Bose-Einstein condensate. Macroscopic phase is related to many properties of BECs such as quantum coherence, superfluidity and superconductivity effects. Therefore, studying the behaviour of the phase in these reduced-dimensionality systems is of great importance.

4.2.1 Phase fluctuations in an elongated 3D BEC

In a BEC, the coherence length defines the point of condensation. When this length becomes larger than the inter-atomic distance, the system can be described

by a single wavefunction. Coherence properties are essential for applications of BEC such as matter wave interferometry [88]. In the case where the trapping frequencies are anisotropic, the coherence length can be larger than the radial size of the trap but shorter than the axial size. This is commonly referred to as a quasi-BEC, or quasi-condensate. In a one-dimensional harmonic oscillator, condensation does not occur at finite temperatures due to the density of states, where $\alpha = 1$ in eq. (2.25) [89].

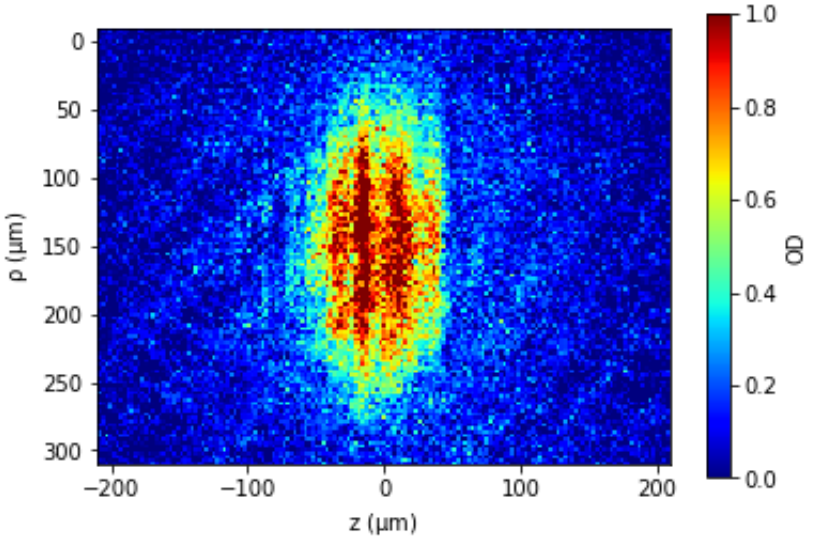


FIGURE 4.4: Example of a density modulated ^{87}Rb atom cloud derived from in-trap phase fluctuations and imaged with absorption imaging 20 ms after releasing the trap. The axial trap frequency is $\omega_z = 2\pi \cdot 20\,\text{Hz}$ and the radial trap frequency is $\omega_\rho = 2\pi \cdot 850\,\text{Hz}$.

Interestingly, a Bose gas does not need to reach these extreme cases to exhibit some low-dimensional physics not encountered in three-dimensional systems. It has been shown experimentally that, for aspect ratios over $\lambda = 40$, the condensate already starts mimicking the behaviour of a low-dimensional Bose gas, as can be seen in fig. 4.4 where phase fluctuations were seen in a condensate with an in-trap aspect ratio of $\lambda = 45$. In these cases, the coherence length becomes larger than the radial size of the trap. When this happens, phase fluctuations inside the condensate appear due to thermal excitations. If the wavelength of the thermal excitations is smaller than all dimensions of the condensate it has a 3D character and does not lead to pronounced phase fluctuations. For elongated condensates, low energy axial excitations have wavelengths larger than the radial size of the sample and therefore acquire a pronounced 1D behaviour, leading to axial phase fluctuations. Phase fluctuations depend on temperature of the condensate, atom

number, and trapping geometry. Since they are the result of thermal excitations, they only appear at finite temperatures.

Let's define a one-dimensional quasi-condensate with a radial frequency ω_ρ, an axial frequency ω_z, and an axial length L as follows:

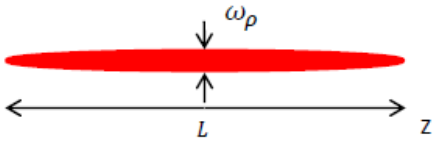


FIGURE 4.5: One-dimensional quasi-condensate.

From the Bogolyubov equations, the mean square thermal fluctuations are given by [90]

$$\left\langle \left[\delta\hat{\phi}(z,z')\right]^2 \right\rangle_T = \Sigma_{j:\epsilon_j<\hbar\omega_\rho} \frac{\mu(j+2)(2j+3)}{15(j+1)\epsilon_j N_0} \left[P_j^{(1,1)}\left(\frac{z}{L}\right) - P_j^{(1,1)}\left(\frac{z'}{L}\right)\right]^2 N_j \tag{4.1}$$

where $P_j^{(1,1)}$ is a Jacobi polynomial, N_0 is the number of BEC particles, and N_j is the equilibrium occupation number for the excitations. They are defined by the following equations:

$$\epsilon_j = \hbar\omega_z \sqrt{\frac{j(j+3)}{4}}, \tag{4.2}$$

$$N_j = \frac{T}{\epsilon_j}, \tag{4.3}$$

$$N_0 = \left(\frac{8\pi}{15}\right) n_{0m} R_{TF}^2 L. \tag{4.4}$$

In the Thomas-Fermi regime, the 3D density distribution has a parabolic shape with radius $R_{TF} \approx (2\mu/m\omega^2)^{1/2}$ and maximum density value $n_{0m} = \mu/g$, where g is the coupling constant.

At temperatures $T \gg \hbar\omega_z$ and on a small distance scale of $|z - z'|/L$, the phase fluctuations are determined by [90]

$$\left\langle \left[\delta\hat{\phi}(z,z')\right]^2 \right\rangle_T = \delta_L^2 |z-z'|/L, \tag{4.5}$$

where

$$\delta_L^2 = \frac{32\mu T}{15N_0(\hbar\omega_z)^2}. \tag{4.6}$$

The Thomas-Fermi chemical potential is given by

$$\mu = \left(\frac{15N_0 g}{\pi}\right)^{2/5} \left(\frac{m\omega_\rho^{2/3}\omega_z^{1/3}}{8}\right)^{3/5}. \tag{4.7}$$

Hence,

$$\delta_L^2 = \left(\frac{T}{T_c}\right)\left(\frac{N}{N_0}\right)^{3/5}\delta_c^2. \tag{4.8}$$

For $N_0 \approx N$, the fluctuations are governed by the parameter δ_c^2. For $\delta_c^2 \gg 1$, the nature of the BEC depends on temperature. Therefore, there is a characteristic temperature at which $\delta_L^2 \approx 1$, given by

$$T_\phi = \frac{15N\hbar^2\omega_z^2}{32\mu(\omega_\rho,\omega_z)}. \tag{4.9}$$

In the temperature interval $T_\phi < T < T_c$ the phase fluctuates. In other words, the phase will undergo pronounced fluctuations when $\hbar\omega_z < |\mu| < \hbar\omega_\rho$. This interval is larger for larger atom number inside the same trap as well as for more extreme aspect ratio configurations.

It is hard to get a full picture of the phase of the condensate in trap. Some groups have developed simulations showing how the phase fluctuates [83, 90]. When it comes to measuring it, the phase at each point has to be compared to an already known phase. One could think of an experiment in which two condensates are generated, one with a three-dimensional character and therefore constant phase in trap, and another one with a one-dimensional character presenting phase fluctuations. Using the system as an interferometer, the phase at different points of the elongated condensate can be interrogated. Since the phase fluctuates randomly,

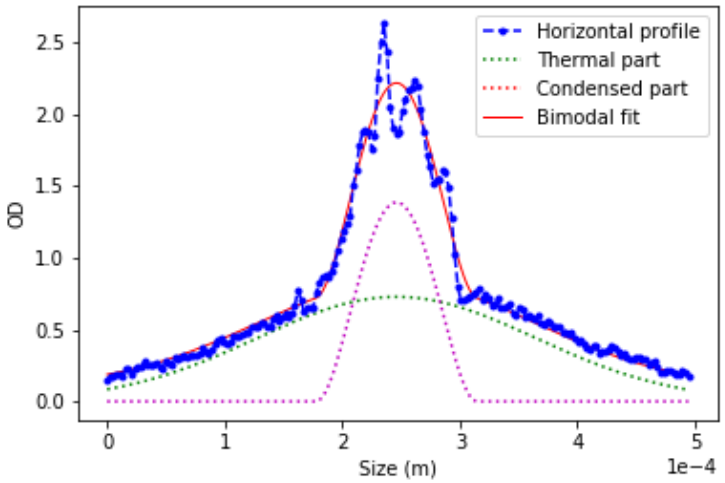
the interrogation in different locations along the one-dimensional condensate has to be done in the same cycle. For this, a multi-condensate experiment can be a great tool (see section 5.3), where the condensate is divided in two condensates, and one of them is then fragmented into multiple three-dimensional condensates.

A more straight forward way of studying the physics of low-dimensional condensates is to look into density fluctuations, produced by in-trap phase fluctuations, after ballistic expansion.

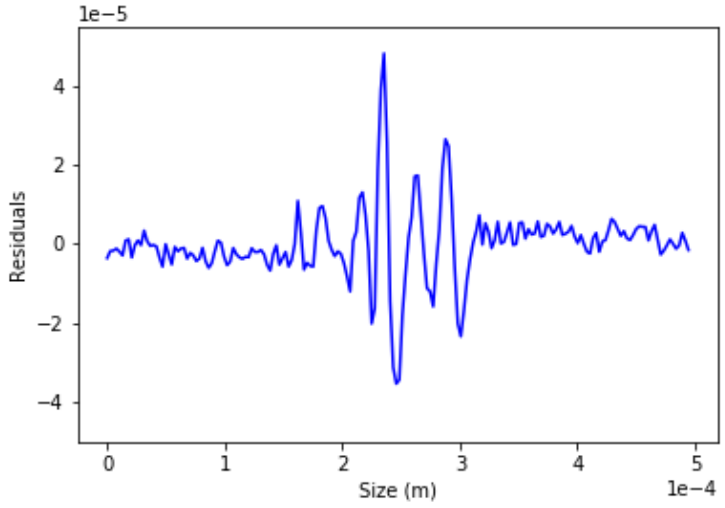
4.2.2 Density fluctuations in free expansion of the atom cloud

Phase fluctuations produce large phase gradients in the trapped atom cloud. These gradients induce different velocities in different regions of the condensate. After switching off the trap, the mean-field interaction rapidly decreases and the axial velocity field is then converted into a particular density distribution after ballistic expansion. In the equilibrium state of a BEC in a trap, the density fluctuations remain unaffected even if the phase fluctuates - the mean-field interparticle interaction prevents the transformation of the local velocity fields provided by the phase fluctuations into modulations of the density.

In the experiment, the cloud of atoms was first cooled down to a few hundred nano-Kelvin before extracting the atom density profile from the absorption imaging process. To ensure proper visualisation of the different density regions when imaging, the resulting image was de-noised, ignoring features that are not relevant to this study, such as the photon noise. The way this is done is by Fourier transforming the image, removing the high frequencies, and transforming it back. During this process, the vertical and horizontal axes were de-noised differently, to ensure that the features coming from the fringes were not removed or altered. After this, the density profile of the cloud was extracted, and fitted to a bimodal distribution with a Thomas-Fermi region and a Gaussian region, shown in fig. 4.6a. Extracting the fit from the density profile results in the plot of the residuals, fig. 4.6b. With the Thomas-Fermi radius being calculated from the bimodal fit, the shot noise shown in the thermal part is then removed to avoid it having any effect on the measurement of the density of fringes. Then, the amplitude of fringes and the number of fringes can be measured.



(a) Bimodal fit.



(b) Residuals of the bimodal fit.

FIGURE 4.6: Analysis of phase fluctuations for the density plot shown in fig. 4.4. The phase fluctuations in-trap induce density modulations after ballistic expansion, which can be quantified from the residuals of the bimodal fitting in the Thomas-Fermi region. (a) shows the bimodal fit (red line) of the optical density, OD, (blue dots) of a BEC with phase fluctuations, after 20 ms of time of flight. (b) shows the residuals extracted from the difference between the blue points and the red line in (a), and provides a tool for measuring the root mean square of the atom density fluctuations. The axial trap frequency is $\omega_z = 2\pi \cdot 20\,\text{Hz}$ and the radial trap frequency is $\omega_\rho = 2\pi \cdot 850\,\text{Hz}$.

A very simple test to ensure that the density modulations are indeed generated by in-trap phase fluctuations is to average over a set of images taken in consecutive experimental cycles. Since the fluctuations are random, the averaged image should not show any density modulations. This test was carried out several times in the experiment, confirming the existence of such phase fluctuations, as seen in fig. 4.7. One might claim that the shot noise is responsible for the random fringe pattern formation. To eliminate this possibility, different laser intensities were used when imaging the atoms. Even though the shot noise scales down at higher imaging intensities, the measured atom density profiles still revealed a clearly distinguishable fringe pattern.

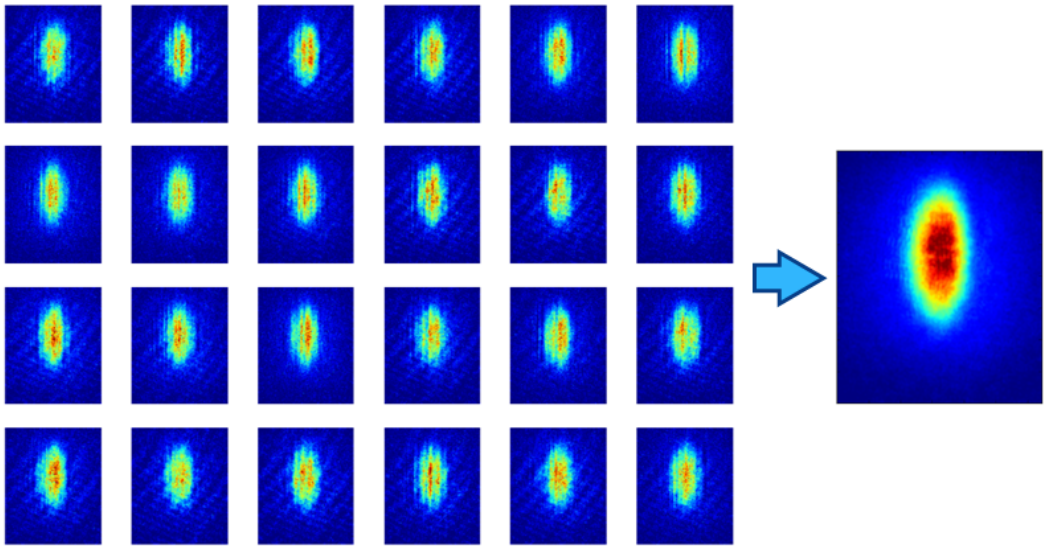


FIGURE 4.7: Set of density modulated atom cloud images taken in consecutive experimental cycles with their average (right-hand side), to ensure that the density modulations are indeed generated by in-trap phase fluctuations.

The scale of the mean square density fluctuations in the central part of the cloud, after a ballistic expansion time, t, can be expressed as [90]

$$\left(\frac{\sigma_{BEC}}{n_0}\right)^2 = \frac{\omega_z}{\omega_\rho}\frac{T}{T_\phi}\sqrt{\frac{\ln(\omega_\rho t)}{\pi}}\left[\sqrt{1+\sqrt{1+\left(\frac{\hbar\omega_\rho^2 t}{\mu\ln(\omega_\rho t)}\right)^2}}-\sqrt{2}\right]. \tag{4.10}$$

This equation predicts a linear variation of the density fluctuation amplitude with the temperature of the system [34, 91], as well as showing how the density of the fringes should increase over the time-of-flight, t. Since measuring the temperature of a cold Bose gas is not an easy task, having a way of doing thermometry from

the density modulations alone can be a very useful tool in such low-dimensional setups. Thermometry was attempted by scanning the temperature of the cloud of atoms from $T \approx 850\,\mathrm{nK}$ to $T \approx 240\,\mathrm{nK}$. Fringes are clearly seen as soon as $T < T_c$. When going below 240 nK, the condensate disappears rapidly, making it very complicated to image the region where $T < T_\phi$. The chemical potential in this region is very low, making the condensate extremely susceptible to any external perturbation. Consequently, measurements in this region are highly sensitive and inaccurate.

A finer scan of the temperature was taken, using extra wires on the chip to increase the aspect ratio to $\lambda \approx 45$, with temperatures ranging from around 750 nK to around 200 nK in nine steps. For this, ten different sets of images were taken after 18 ms of time-of-flight, and the results averaged. Figure 4.8 shows the root mean square of the fringe density averaged along the BEC, versus the temperature of the cloud. The error in the y axis is taken as the standard error of the ten sets measured. The temperature was estimated from the final value of the RF frequency applied for the evaporative cooling. For this, the temperature was previously measured for different RF values by fitting the thermal part of the distribution to a Gaussian. This method needs improvement for further study of phase fluctuations but, for the work in this thesis, it proves the dependence of the fringes on the temperature, and gives very precise results when comparing it to previous work from other groups [34].

From eq. (4.10) one can see the relation between the density of fringes and the time-of-flight. The longer the time-of-flight, the more pronounced these fringes will be. This behaviour is clearly observed in the experimental data shown in fig. 4.9. The values plotted on the vertical axis are the root mean square density fluctuations in the cetral part of the cloud for different time-of-flight measurements, with the error being the standard error of the three sets measured. These results agree well with previous work from other groups [83, 91], where the theoretical density of fringes from eq. (4.10) shows a very similar trend in the data. The data in fig. 4.9 is in arbitrary units since they are derived from the number of counts per pixel of the camera, and the image is also post-processed.

When a phase fluctuating Bose gas is released from its trapping potential, atoms start travelling freely along the cloud. Therefore, the density modulations of the expanding cloud will only appear after an atom, starting from the centre of the

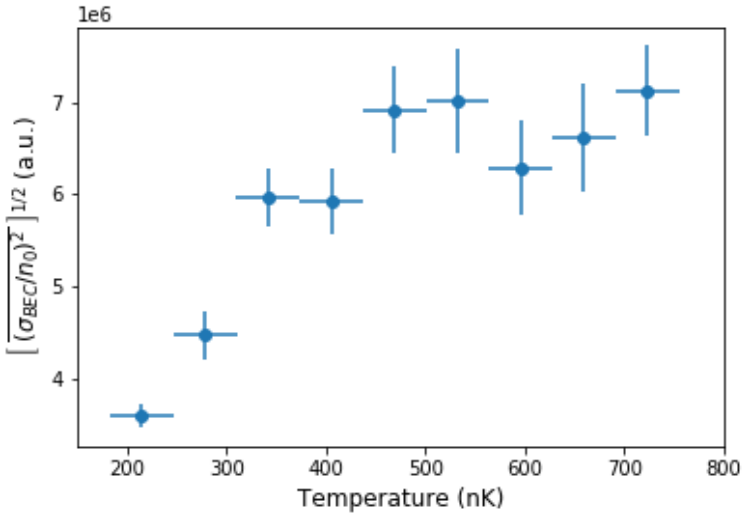


FIGURE 4.8: Root mean square of the atom density fluctuations averaged along the atom cloud for different temperatures. Points show experimental values averaged over ten sets. Temperature is calculated by fitting the Gaussian thermal cloud surrounding the condensate.

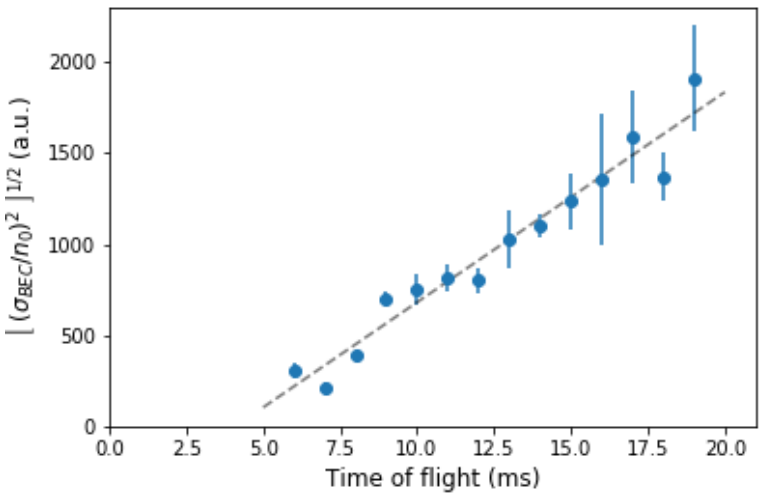


FIGURE 4.9: Root mean square of the atom density fluctuations averaged along the atom cloud for different time of flight values of the phase fluctuating cloud. Points show the experimental results averaged over three sets. Dashed line is the linear fit to the measured data to help visualisating the results.

Bose gas, has had enough time to travel to the edge of the cloud. This time can be estimated from the thermal velocity of a particle, via the following equality

$$\frac{3}{2}k_B T = \frac{1}{2}mv^2, \tag{4.11}$$

where k_B is the Boltzmann constant, T is the temperature, v the velocity of the particles and m the mass of the atoms, in this case ^{87}Rb.

In our case, with an axial Thomas-Fermi radius measured to be roughly 60 µm, indicating the size of the condensed region, the estimated time for the fringes to start appearing is $\approx$ 4 ms, which agrees with the experimental observation (fig. 4.9).

4.3 BEC microscopy and disorder

In the last few decades, there has been great interest in, and development of, imaging techniques [92, 93]. Macroscopic imaging techniques have been well researched and developed, leading to many advances in science and technology. The problem comes when trying to image at a microscopic level, on the scale of nanometres. A common example to illustrate this scenario is checking for cracks in the wings of aeroplanes. It is well known from studying material fatigue that, before a complete break down of a material, microscopic cracks start appearing. Being able to image these cracks can prevent disastrous consequences. Using atoms in their lowest energy configuration is arguably one of the best routes to achieve the required scale and sensitivity for microscopy to detect early signs of fatigue.

The principle of Bose-Einstein condensate microscopy relies on the effect that the surface has on atoms trapped just above it. Let's consider an already-formed BEC on a chip. The BEC can be transported over the material that needs to be analysed. Passing a current through such material will create a magnetic field component that will then affect the trapping potential of the chip. In the case of cracks on aeroplane wings, this addition should only add one component of magnetic field, orthogonal to the flow of current. This will displace the cloud, without altering its form. On the other hand, if the wing presents some imperfections, the current flow will not be straight, but will follow some meandering path. This path generates magnetic fields with two or three spatial components. The cloud of

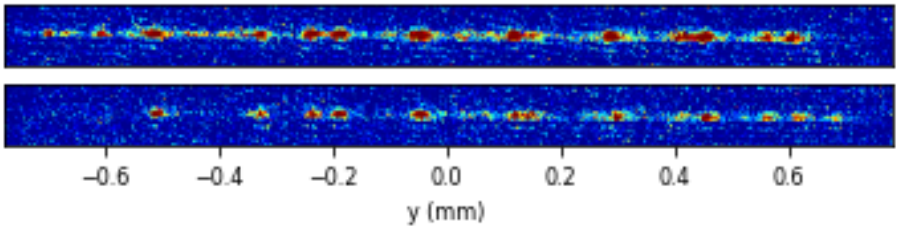
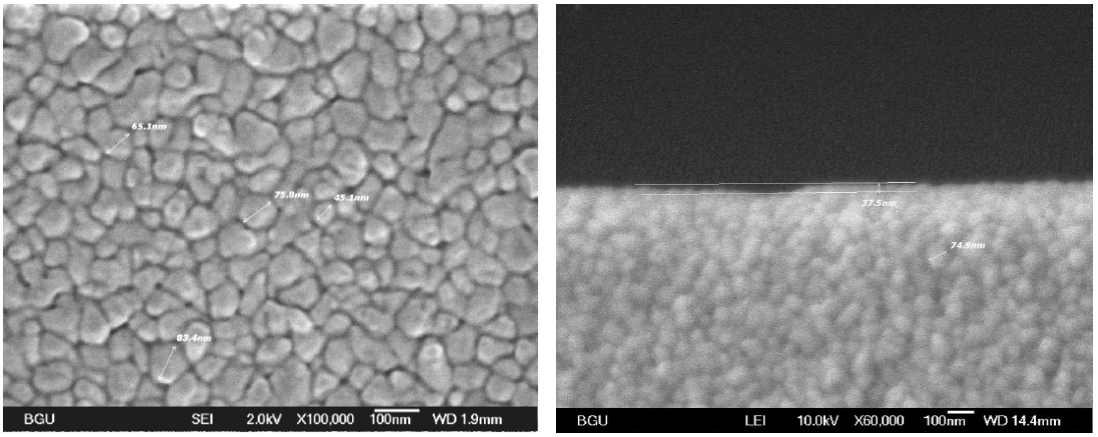


FIGURE 4.10: Atom density profile measured for a fragmented BEC 10 µm from the surface of the chip. The top image shows the fragmented cloud, and the bottom image is the fragmented cloud with the centre of mass displaced to the right, showing how the density maxima occur at the same positions, proving that the BEC is performing microscopy of the trapping wire.

atoms will then be displaced in different directions as well as fragmented. Imaging the fragmented and displaced cloud of atoms can enable reconstruction of the path that the current passing through the wing took.

To demonstrate this, an experiment was carried out on the atom chip. Starting with a BEC, the current through the Z wire was reduced gradually to 150 mA, positioning the condensate closer to the surface of the wire. This could have been done by ramping up the bias field instead, but that would make the magnetic potential tighter and therefore the scanning area would be smaller. When the cloud is placed within 20 µm from the surface, the condensate fragments into sub-condensates within multiple potential wells, as shown in the top image in fig. 4.10. This fragmentation is produced by the imperfections in the chip wire used to trap the atoms [94]. Such imperfections are shown in the microscope photographs taken in the fabrication report (see fig. 4.11). To prove that the fragmentation is not caused by any other factor, in a second experiment, a 2 A current was passed through one of the side-wires, V-W in fig. 4.3a, adding an extra magnetic field component that pushes the whole centre of mass to one side. The bottom image in fig. 4.10 shows that even though the whole cloud was displaced to the right, the atom density maxima still fell at the exact same positions, proving that the underlying potential perturbations were indeed generated by the imperfections from the trapping wire of the chip. Additional study of the effects of imperfections on the chip are further developed in section 5.1.

Once a region of space has been imaged, the microscope can be moved and the cycle repeated. With each cycle lasting under 30 s, and the possibility of decreasing this time-scale, surfaces can be scanned in a matter of minutes. Further development could see the creation of a two-dimensional condensate, instead of the



(a) Atom chip surface roughness. (b) Atom chip edge roughness.

FIGURE 4.11: Micrographs from the fabrication report from Ben Gurion University showing the atom chip used in the experiment. Microscope images show (a) the granular surface roughness and (b) the edge imperfection generated during the fabrication process.

one-dimensional condensate described here, which would result in the imaging of two-dimensional surfaces in a single cycle. This research shows the potential for using cold atomic clouds for microscopy, although further miniaturisation of the setups will be needed in order to make these systems portable and reliable enough for the commercial market.

Chapter 5

Fragmentation of a low-dimensional condensate

This chapter is divided into three sections, the first part of the chapter addresses the experimental observation of fragmentation in low-dimensional Bose-Einstein condensates (BEC) at short distances to the surface. The second part proposes a possible explanation for this fragmentation. Finally, the third part of the chapter describes the experimental capabilities of having multiple condensates in each experimental cycle.

The unexpected fragmentation of the condensate observed when lowering the atoms closer to the surface of the chip is addressed at the beginning of the chapter. Different tests done in the hope of understanding this effect are described in the following paragraphs. After not reaching a clear conclusion as to how this effect originates, a possible explanation is proposed on the grounds of these tests, suggesting that imperfections in the conducting wires of the atom chip explain this effect. An uneven distribution of electrons in the conducting wires would cause corrugations in the current flow. These imperfections would be at a nano-scale, making it impossible to be observed using conventional microscopes. A very brief description of the manufacturing process is then given, and a simulation of the trapping potentials from such wires is performed.

The final section of this chapter focuses on how this fragmentation can be used to the advantage of having multiple condensates per cycle. This ultimately can result in several experiments performed at the same time, potentially saving time when running experiments or using the setup as a quantum sensor.

5.1 Fragmentation of a low-dimensional BEC

As explained in section 4.3, one of the applications of such an experiment is to image surfaces by analysing the magnetic field generated when passing a current through those surfaces. This is because any change in the direction of the current will induce a magnetic component in a certain direction, affecting the effective trapping potential seen by the atoms. The magnetic field generated scales down with the square of the distance from the source. This means that, the closer the sensor is placed with respect to the object, the larger the effect on the trapping potentials will be.

In the experiment described in this document, the imperfections due to irregularities on the wire can be seen with distances $< 10\,\mu m$. Unfortunately, in this experiment, the elongated condensate splits in different high atom density sub-clouds before this point, at distances $< 80\,\mu m$.

5.1.1 Formation of sub-clouds in an elongated 3D-BEC

The formation of sub-clouds when pushing atoms closer to the surface has been one of the major issues encountered when studying low-dimensional behaviour of the BEC. This effect has been observed every single time that the atoms were moved closer to the surface of the atom chip, independently of the method used for this purpose. Figure 5.1 shows an example of an image of a cloud of ^{87}Rb atoms trapped on the atom chip at a distance of $\approx 10\,\mu m$.

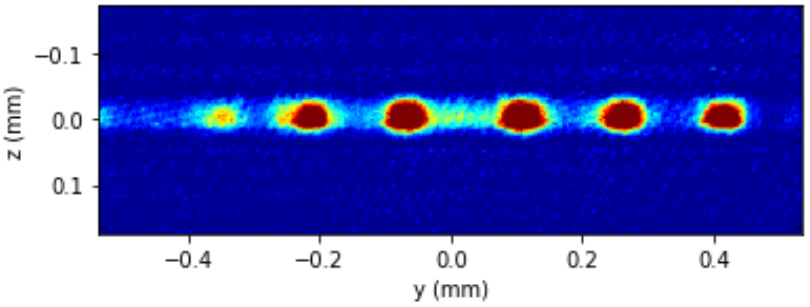


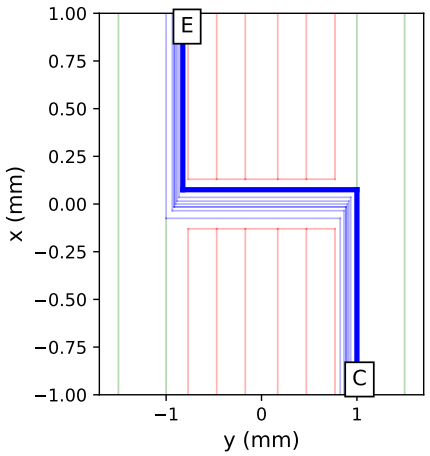
FIGURE 5.1: Fragmentation of a low-dimensional condensate trapped on the atom chip with 200 mA through the Z-wire, at a height of $\approx 10\,\mu m$, and 1 ms time-of-flight. This elongated atom cloud was achieved with the use of wires VW and CD (see fig. 4.3a). The horizontal axis determines the distance from the centre of the atom chip.

Different tests were carried out in the hope of finding clues leading towards a better understanding of this effect.

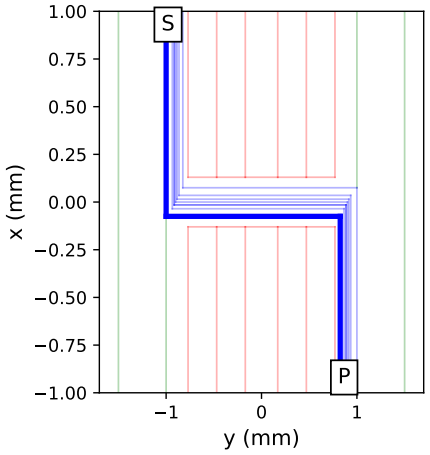
The first, and most obvious, was to determine whether this effect was observed regardless of the method used to push the atoms closer to the surface. The atoms will move closer to the chip as the total magnetic field component in the direction normal to the surface of the chip becomes weaker. As seen in section 3.7, this can be done either by reducing the current through the Z-wire, by increasing the component of the X-Bias field, or by a combination of both. In all three cases the fragmentation effect was observed with ease. The only differences were in the trapping frequencies in the axial and radial components, which is expected since the trapping potentials are configured differently.

The design of the Ben-Gurion chip allowed for the use of up to seven different wires with a Z shaped configuration, as seen in section 3.7. All of these wires (except for the ones with broken connections) were tested by BEC imaging of the potential landscape to determine if the fragmentation is caused by imperfections in one, and only one, of the wires. In all cases, fragmentation was clearly seen, independently of the wire used. It is good to note that, even though the centre of mass was displaced by the different position of the legs of the Z-wires (vertical sections of the Z-wires in figs. 5.2a and 5.2b), the sub-clouds occur in the same position (see fig. 5.2c). Such separation corresponds to approximately half of the distance between adjacent U shaped wires surrounding the Z shaped wires. This suggests that even though no current flows through the U shaped wires, their presence might still be influencing the atom density profile. Figure 5.2c shows two different images taken with a condensate trapped using the P-S wire (see fig. 5.2b) and the C-E wire (see fig. 5.2a), respectively. For both cases the current was 200 mA and the height over the atom chip surface $\approx 10\,\mu$m. The lower atom number in the bottom image is due to the BEC experimental cycle being optimised for transfer into the P-S wire, and not the C-E wire, as well as the imaging system being out of focus for the latter.

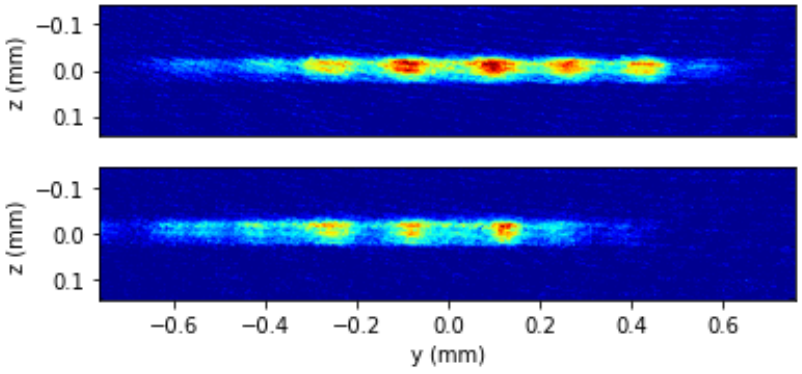
One could also question whether charges can accumulate on the conducting plates of the chip, effectively acting like a capacitor and inducing an extra electric component that affects the confining potentials, fragmenting the cloud. To ensure that this was not the case, all conducting parts of the chip not used for the production of BEC were connected to a specific potential (-12 V, 0 V and 12 V) with respect to the Z-wire. This also showed no effect on the splitting of the condensate. Only



(a) C-E wire.



(b) P-S wire.

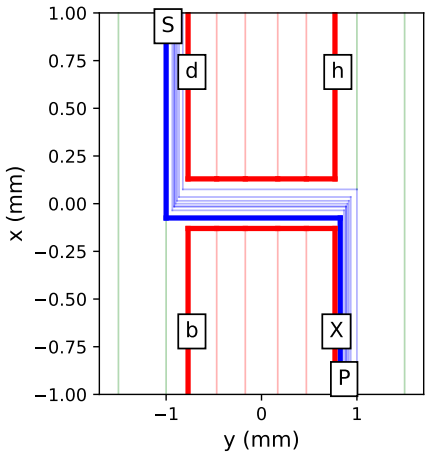


(c) Fragmentation of the atom cloud held above P-S (top image) and C-E (bottom image) wires.

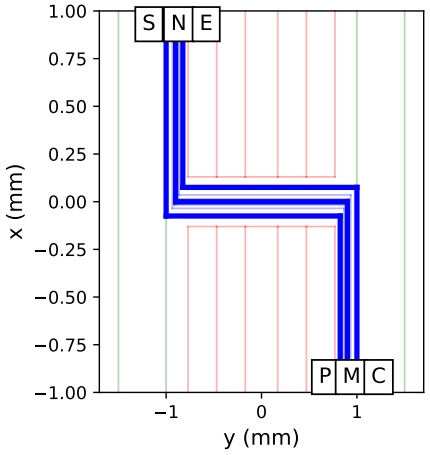
FIGURE 5.2: Fragmentation observed for BECs trapped with different Z shaped wires. The atom density plot in (c) shows fragmentation of a low-dimensional condensate trapped using the P-S wire (top image) and the E-C wire (bottom image). In both cases the condensate was trapped passing 200 mA through the Z-wire, and the image taken after 1 ms of TOF.

a slightly lower atom number was observed due to noise induced with the addition of cables and power supplies.

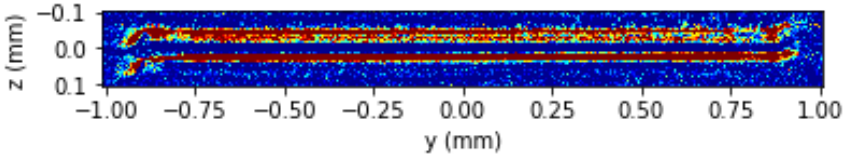
Taking into account the results of the tests explained here, one can realise that such imperfections are present in, at least, all of the central wires, and located at the same position with respect to the comb structure comprising U shaped wires. During the manufacturing process of the chip, the fabrication of the comb structure part could have influenced the quality of the central Z shaped wires. If this was the case, these wires would induce an extra component of the field in the x-direction, altering the trapping potential that the atoms see and, effectively, creating small dips in which the atoms would fall once the sample is cold enough. Assuming there is some kind of imperfection present in all central wires, these extra components of the field can be cancelled by applying current in the opposite direction in adjacent wires. An experiment was carried out in which the X-Bias field, usually generated by the use of external coils, was then generated using different wires in the chip. This creates a self-contained atom chip trap, that does not require the use of external coils for achieving condensation once the atoms are transferred into the atom chip magnetic trap. Two different schemes were used for this test (fig. 5.3). In the first case (fig. 5.3a), the P-S wire was used as the trapping wire, and wires h-d and X-b (red) were used to create the X-Bias field with currents running in opposite direction to P-S wire. In the second case (fig. 5.3b), N-M was used as the trapping wire, and S-P and E-C created the X-Bias field component. The first configuration was still showing fragmentation, whereas with the second configuration, the fragmentation completely disappeared, as shown in fig. 5.3c. This suggests that there is some kind of imperfection present in all of the central Z shaped wires, since the imperfections are counteracted using these parallel wires for creating the X-Bias field. Figure 5.3c shows the atom density profile of a condensate trapped by passing a current of 150 mA through the N-M wire and 400 mA through the S-P and the E-C wires (fig. 5.3b wiring configuration).



(a) X-Bias field created with comb structure.



(b) X-Bias field created with parallel Z-wires.



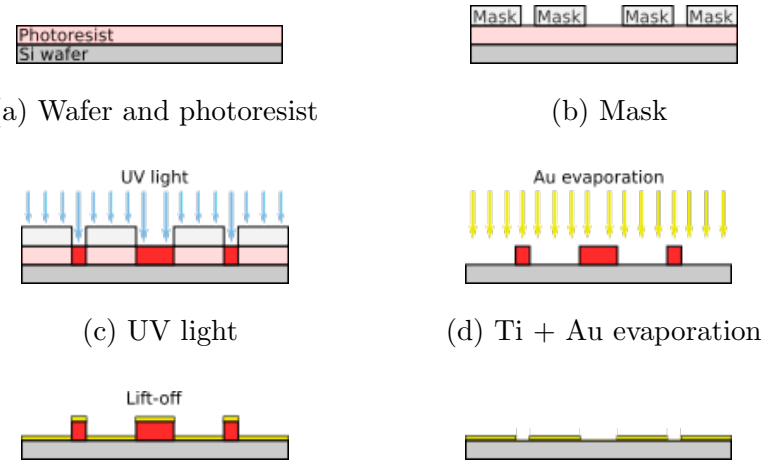
(c) Atom density profile of a BEC ≈ 15 µm from the surface using the wiring configuration in (b).

FIGURE 5.3: Two wiring configurations implemented in order to create a self-contained atom chip trap, without external coils. (a) shows a configuration in which the U shaped wires (red) are used to generate the X-Bias field component. (b) shows a different configuration with parallel Z shaped wires used to generate the X-Bias field component. The density profile of the BEC shown in (c) was taken using the configuration in (b). No fragmentation was seen, even at atom chip distances much smaller than those at which fragmentation usually occurs. The image was taken 1 ms before switching off the trap to ensure that the expansion of the condensate does not mask any fragmentation of the atom cloud. This smoothness was observed also after time of flight.

5.1.2 Atom chip fabrication

The fabrication of atom chips has become a whole area of research in the last decade. Its complexity and nano-scale require new and improved fabrication techniques [95]. A simple wire bond between an atom chip and a PCB requires hours of work in the clean room facilities.

The atom chip used in this experiment was manufactured using a "Lift-off process" [26, 96, 97], in the Ben-Gurion University of the Negev. The process is started by placing an empty wafer of the desired material, in this case a $500 \pm 25\,\mu m$ thick polished Si wafer, boron doped and covered by a 100 nm thick SiO_2 insulating layer (fig. 5.4a), with an additional photoresist layer on top. A lithography mask with the negative image of the pattern of the desired chip is then placed on top (fig. 5.4b), and UV light is shone onto the sample for a few seconds. Baking this sample makes the previously exposed areas insensitive to further exposure, and the unexposed areas are carefully removed (fig. 5.4c). Thermal evaporation of a 30 nm thick Ti adhesion layer and 2 µm thick Au top layer then takes place. (figs. 5.4d and 5.4e). Removing the photoresist areas uncovers the final atom chip (fig. 5.4f).



(a) Wafer and photoresist (b) Mask

(c) UV light (d) Ti + Au evaporation

(e) Lift-off (f) Atom chip

FIGURE 5.4: Atom chip lift-off process. A photoresist material is applied on top of a Si wafer. Using UV light and a mask, the desired patterns are printed on the photoresist (red). The gold tracks (yellow) of the atom chip are then evaporated on top. Finally, the photoresist is removed, leaving the gold wires on the Si wafer. See text for details.

5.1.3 Suppression of imperfection effects

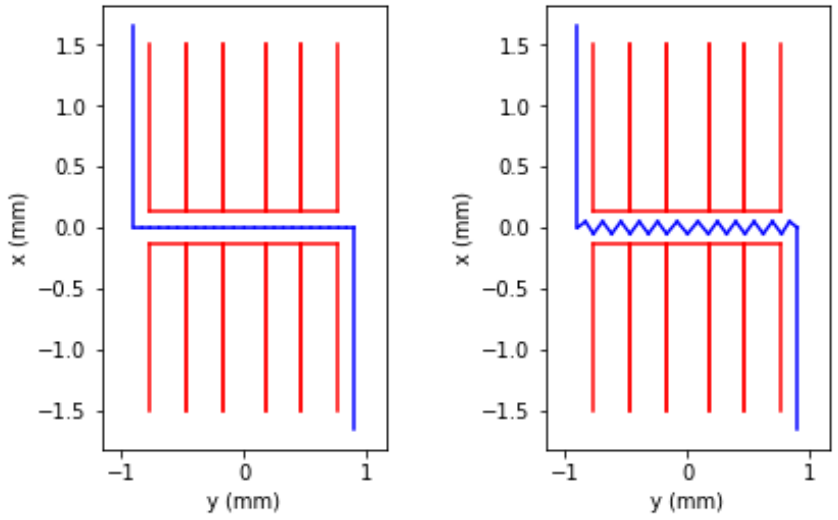
A change in the trapping potential is given when the imperfections add a perturbing component of field in a direction other than orthogonal to the current flow. A method to eliminate this perturbation is presented in [98]. By modulating the current from negative to positive, both on the chip wire and for the bias field, the additional field components created by the imperfections will be counteracted. Since the bias field is also oscillating in phase with the current oscillation in the chip wire, the trapping potential will be kept. Although this system might sound like a great solution to ignore imperfections, there is an additional difficulty present when using AC currents instead of DC currents. Controlling the current output of an AC power supply imposes new challenges, e.g. making sure the modulation in the bias field and in the chip wire is in phase. Moreover, the use of coils to create the bias field in this case becomes trickier, since the inductance of the coils is too high for them to change direction of current at a sufficiently fast rate.

5.2 Effect of a corrugated current flow

In this section, a possible explanation for the fragmentation observed experimentally is proposed. The nano-scale nature of atom chips makes invisible imperfections alter the trapping potential that atoms see [99]. This is even more critical when the atoms sit close to the surface of the chip, at distances $< 100\,\mu m$. When the confining potential changes slightly, the evolution of the BEC will be different [100]. It can lead to a splitting of the BEC, forming a string of several BECs.

The first step is to simulate the fields created by a simple Z-wire, without any imperfections. Then, a pattern of "zig-zag" imperfections is introduced, making the corners of the "comb" structure coincide with the corners of the "zig-zag" wire. Figure 5.5a shows the coordinate schematics of the chip used in this section. Figure 5.5b is the schematic showing the imperfections with a larger amplitude of the zig-zag. This second figure is just for explanatory purposes, and this configuration was not used.

Taking the parameters used in the experiment, the simulations reproduce all three components of the magnetic field. For this, the Z-wire is considered to be an infinitesimally thin stick wire. Some tests were done with a rectangular wire,



(a) Atom Chip 50 nm imperfections (b) Atom Chip 50 µm imperfections

FIGURE 5.5: Schematics of the atom chip structure used for the simulation. The central wire is in a "zig-zag" configuration emulating a corrugated current flow. The simulation was performed with a change of 0.04° in the path of the current at each change in the wire direction, corresponding to (a). (b) contains the same corrugation with 10^3 larger scale, only for illustration purposes.

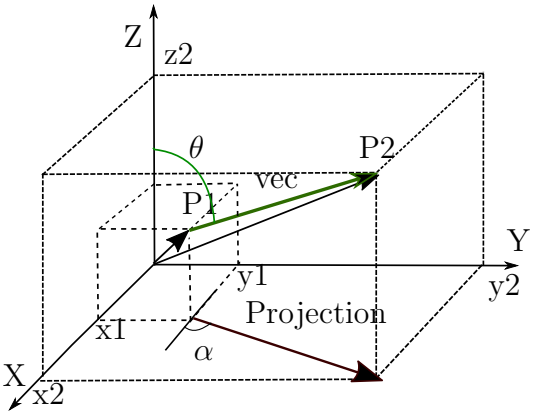


FIGURE 5.6: Angles of rotation α and θ.

showing no notable difference in the results. This is because the height of the cloud of atoms is a few times larger than the width of the wire. Each wire is then defined by a set of segments that form the Z-wire. The field generated by these independent stick wires is calculated at each point in the trapping region.

The first step is to define each independent wire segment, with a starting point P1(x_1, y_1, z_1) and a final point P2(x_2, y_2, z_2) (see fig. 5.6). The angle of rotation α around the z-axis is calculated,

$$\alpha = \arctan\left(\frac{y_2 - y_1}{x_2 - x_1}\right)\left(\frac{180}{\pi}\right). \tag{5.1}$$

Once α is calculated, the length of the projection of the wire on the XY plane is given by $(x_2 - x_1)/\cos(\alpha)$ and the angle of rotation θ around y-axis is,

$$\theta = \arctan\left(\frac{z_2 - z_1}{\frac{x_2}{\cos(\alpha)} - \frac{x_1}{\cos(\alpha)}}\right)\left(\frac{180}{\pi}\right). \tag{5.2}$$

To facilitate application of the Biot-Savart law to the zig-zag line elements, the following transformations are applied, which centre each element at (0,0,0).

$$\begin{aligned} x &= x - \frac{x_1 + x_2}{2}, \\ y &= y - \frac{y_1 + y_2}{2}, \\ z &= z - \frac{z_1 + z_2}{2}. \end{aligned} \tag{5.3}$$

Knowing α, θ and the length of the wire

$$L = \sqrt{(x_2 - x_1)^2 + (y_2 - y_1)^2 + (z_2 - z_1)^2}, \tag{5.4}$$

the rotated coordinates are obtained, using the rotational matrices [101]. The coordinates are rotated first around the z-axis and then around the y-axis,

$$\Re_z(\alpha) = \begin{bmatrix} \cos(\alpha) & \sin(\alpha) & 0 \\ -\sin(\alpha) & \cos(\alpha) & 0 \\ 0 & 0 & 1 \end{bmatrix} \begin{bmatrix} x \\ y \\ z \end{bmatrix} = \begin{bmatrix} x\cos(\alpha) + y\sin(\alpha) \\ -x\sin(\alpha) + y\cos(\alpha) \\ z \end{bmatrix}, \tag{5.5}$$

$$\Re_y(\theta)\,\Re_z(\alpha) = \begin{bmatrix} \cos(\theta) & 0 & -\sin(\theta) \\ 0 & 1 & 0 \\ \sin(\theta) & 0 & \cos(\theta) \end{bmatrix} \begin{bmatrix} x\cos(\alpha) + y\sin(\alpha) \\ -x\sin(\alpha) + y\cos(\alpha) \\ z \end{bmatrix}, \tag{5.6}$$

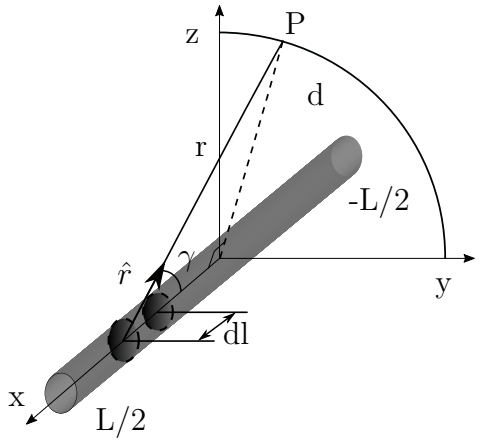


FIGURE 5.7: Biot-Savart law applied to a stick wire of finite length.

$$\begin{aligned} x_r &= x\cos(\alpha)\cos(\theta) + y\sin(\alpha)\cos(\theta) - z\sin(\theta) \\ y_r &= -x\sin(\alpha) + y\cos(\alpha) \\ z_r &= x\cos(\alpha)\sin(\theta) + y\sin(\alpha)\sin(\theta) + z\cos(\theta). \end{aligned} \tag{5.7}$$

The magnetic field created by a conductor volume is given by the Biot-Savart law (fig. 5.7),

$$d\vec{B} = \frac{\mu_0}{4\pi} I \frac{d\vec{l} \times \hat{r}}{r^2}, \tag{5.8}$$

where $d\vec{l} \times \hat{r} = dx\sin(\gamma)\,\hat{u}$. The Biot-Savart law is sometimes presented in the integral form

$$\vec{B}(r) = \frac{\mu_0 I}{4\pi} \int_{-L/2}^{L/2} \frac{d\vec{l} \times \hat{r}}{|\hat{r}|^3}, \tag{5.9}$$

from which the two non-zero components of the field are extracted:

$$B_y = \frac{x - \frac{L}{2}}{(y^2+z^2)\sqrt{(x-\frac{L}{2})^2 + y^2 + z^2}}\, z - \frac{x + \frac{L}{2}}{(y^2+z^2)\sqrt{(x+\frac{L}{2})^2 + y^2 + z^2}}\, z \tag{5.10}$$

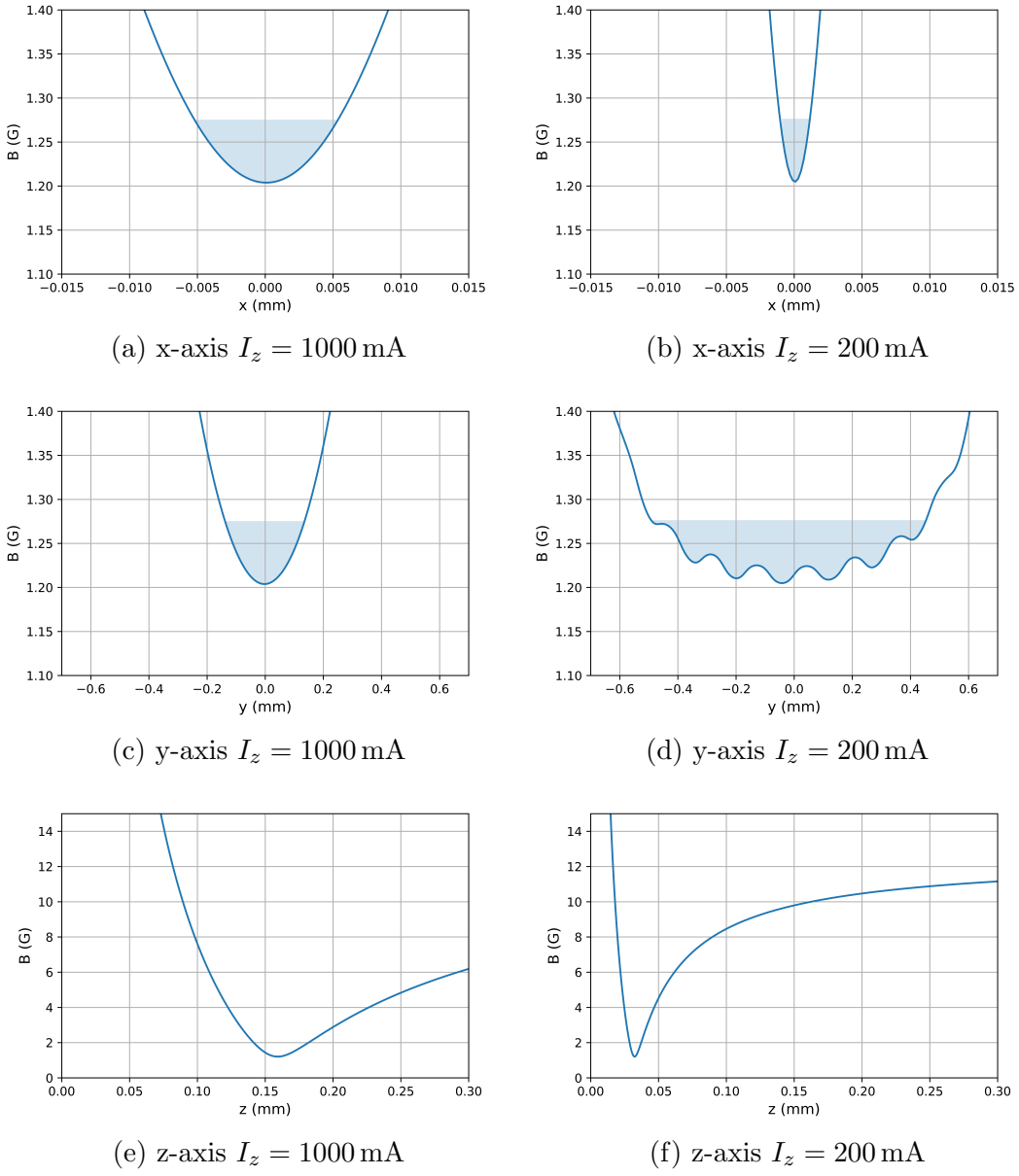
$$B_z = \frac{x+\frac{L}{2}}{(y^2+z^2)\sqrt{(x+\frac{L}{2})^2+y^2+z^2}}\,y - \frac{x-\frac{L}{2}}{(y^2+z^2)\sqrt{(x-\frac{L}{2})^2+y^2+z^2}}\,y\,. \quad (5.11)$$

These field components can now be projected into the original coordinate system, by applying the reverse transformations:

$$\begin{aligned} B_{xp} &= B_x\cos(\alpha)\cos(\theta) - B_y\sin(\alpha) + B_z\cos(\alpha)\sin(\theta) \\ B_{yp} &= B_x\sin(\alpha)\cos(\theta) + B_y\cos(\alpha) + B_z\sin(\alpha)\sin(\theta) \\ B_{zp} &= -B_x\sin(\theta) + B_z\cos(\theta). \end{aligned} \quad (5.12)$$

Each magnetic field component will then be given by the projected field component scaled to the current, I, passing through the wire. A simple scenario of comparison between experiment and theory is proposed in the next few paragraphs. The initial condensate is generated at a distance from the chip of $\approx 159\,\mu m$, using a fixed value of $I_{z-wire} = 1000\,mA$. The distance from the atom cloud to the surface is set by varying the X-Bias field component (varying the current through the coils). The Y-Bias field component is used to raise or lower the trap bottom. This is often neglected in theoretical work, but of high importance in experimental work, since the height of the trap bottom will determine the RF parameters needed during the evaporative cooling stage. The height of the condensate over the surface of the chip can be modified by lowering the current through the chip wire, or by increasing the current through the coils that generate the X-Bias. The first option results in lower confinement in the y direction, due to a weaker effect from the legs of the Z-wire. This option is the one chosen in this document. Experiments using the second option were carried out, proving the higher difficulty in creating elongated condensates. The wire currents used for the comparison were 1000 mA and 200 mA. For each current, the Y-Bias field was corrected (both in the simulations and with coils in the experiment) to keep a similar trap bottom and, therefore, a similar temperature of the cloud.

Figure 5.8 shows the field components calculated versus x, y and z for two different current configurations. There is also a representation (blue shaded region) of how the atoms would fill up the potential if the depth of the atom potential is about 50 kHz. When $I_{z-wire} = 200\,mA$, which corresponds to $\approx 36\,\mu m$ from the surface of the chip, fragmentation is clearly visible (see fig. 5.8d). The distance between



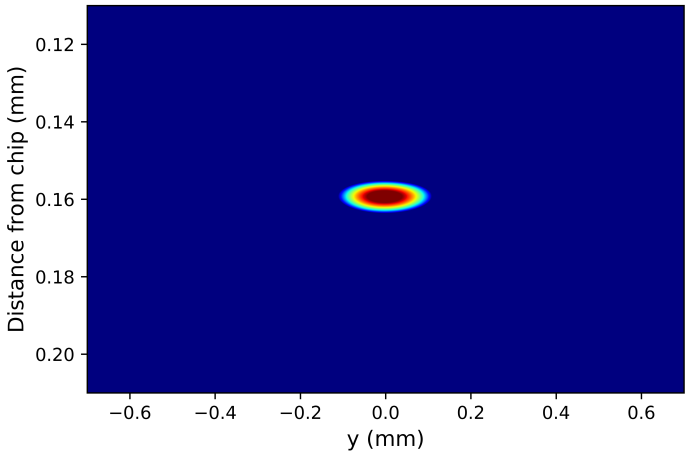
(a) x-axis $I_z = 1000\,\mathrm{mA}$ (b) x-axis $I_z = 200\,\mathrm{mA}$

(c) y-axis $I_z = 1000\,\mathrm{mA}$ (d) y-axis $I_z = 200\,\mathrm{mA}$

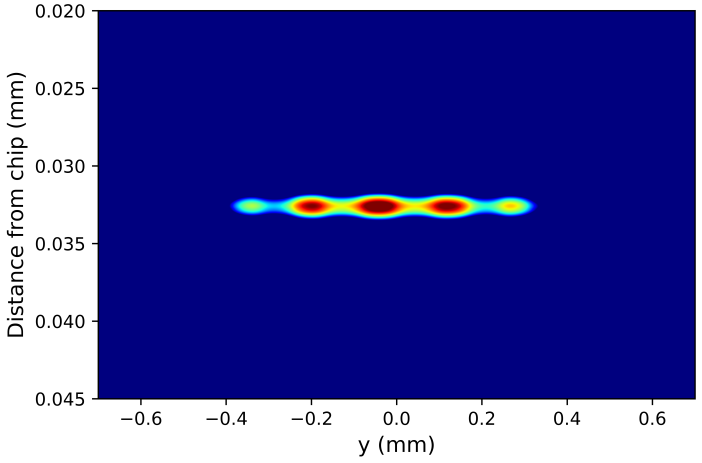
(e) z-axis $I_z = 1000\,\mathrm{mA}$ (f) z-axis $I_z = 200\,\mathrm{mA}$

FIGURE 5.8: Simulated magnetic field variation along x (a,b), y (c,d) and z (e,f) for different currents through the trapping Z-wire (1000 mA, left column; 200 mA, right column). Lower currents through this wire result in closer proximity to the surface of the atom chip. Fragmentation is seen along the y axis for lower I_z currents (d). Blue shaded region shows how the atoms would fill up the potential if the depth of the atom potential is about 50 kHz.

fragmented trapping potential minima, the depth of these fragmented potentials, and the distance from the atom chip at which they appear, are remarkably similar to the experimental observations. Figure 5.9 is a more visual representation of the trapping potentials. In this way, the simulation is easily comparable with the images taken in the experiment. Fragmentation becomes obvious in fig. 5.9b and the simulation agrees well with the experiment, as shown in fig. 5.10.



(a) $I_z = 1000\,\mathrm{mA}$



(b) $I_z = 200\,\mathrm{mA}$

FIGURE 5.9: Simulated in-situ density profiles for ^{87}Rb BECs, as seen along the y axis for different I_z currents. Fragmentation can be seen for $I_z = 200\,\mathrm{mA}$ (b), which corresponds to an atom chip separation of $\approx 36\,\mu\mathrm{m}$. Scales along vertical axis in (a) and (b) are different for clearer visualisation of the fragmentation.

The effect of nanometre scale imperfections on the atom chip poses a limitation on its applications. Some groups are starting to pursue different techniques, e.g. painted potentials [102], as substitutes for atom chips in cold atom experiments, showing a better reliability in the generation of cold clouds.

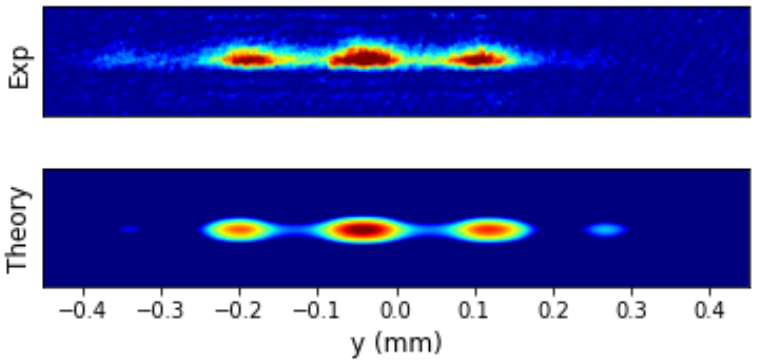


FIGURE 5.10: Comparison between experiment (top image) and simulation (bottom image) for the normalised density profiles of a BEC trapped at ≈ 36 µm from the chip with corrugated current flow in the Z shaped wire. The experimental image is taken after 1 ms of time of flight, whereas the simulation shows the in-situ trapping potential, thus the vertical axis scales are different to ensure proper visualisation of the formation of the fragmentated potentials.

5.3 Exploitation of fragmentation for multiple parallel studies

Building the Atom Chip BEC experiment at the University of Nottingham began eight years after the first BEC on an atom chip [103]. At that time, little was known about the behaviour of condensates near conducting wires. The aim of this experiment was to explore this unknown field. One of the main hopes was to understand condensation in very elongated traps. By using the atom chip Z-wire, the three-dimensional BEC could have been stretched to form a one-dimensional quasi-condensate. Unfortunately, this is not possible due to the trapping potential fragmentation. Therefore, so far in this document, the fragmentation of the cloud of atoms has been treated as a negative effect, resulting from "imperfections" in the chip. Focus was into understanding the "problem", the origin of it, and possible ways around it.

A more positive approach to this situation, would be to exploit the potential of a system that is capable of generating multiple condensates at once. Since every time an image is taken, the atomic sample is altered, it is necessary to generate a new sample of atoms for each measurement. This process slows down considerably any experiment or sensor measurement. In fact, some groups have been working to achieve fragmentation of the cloud and then exploit it to create a multi-experiment machine [104–106].

One of the instruments used to extract information from a condensate is to interrogate its phase. The way of doing this is by comparing the existing phase with a known phase. It is a common practice to split a condensate once it has been formed, perform any desired experiment on one of the two parts, and then recombine both condensates to study the evolution of the phase. The phase coherence in Bose-Einstein condensates can be estimated by the interference pattern created when merging a previously split BEC. This was done experimentally shortly after the achievement of the first condensate [107], as well as simulated theoretically in several publications [108–111]. This pattern would resemble the one seen in the phase fluctuations section (section 4.2). In a "multi-experiment setup", the fragmentation of the condensate could lead to multiple BECs that could be used for parallel experiments in which interference occurs between different sub-clouds. Note that for this to work, the condensate would have to be created before the fragmentation happens, with the condensate generated at distances $> 80\,\mu m$. After this, the experiment would be performed, and the trap released.

Consider a condensate that is split in two, a and b, condensates, positioned at $x_a = -d/2$ and $x_b = d/2$. The relative phase of such condensates inside the trap will be

$$\phi = \phi_a - \phi_b. \tag{5.13}$$

At $t = 0$ they are released from their trapping potential. The mean field energy will make the condensates expand in all directions and, eventually, make them overlap and interfere. During the overlapping process, density modulations are given by

$$n = n_a + n_b + 2\sqrt{n_a n_b}\cos(\phi_a - \phi_b), \tag{5.14}$$

where the gradient of the phase is described by the velocity field of the wavefunction $\nabla\phi = \frac{m}{\hbar}\vec{v}$ [112]. Approximating to the classical velocity of the particles, the gradient of the phase becomes

$$\nabla\phi = \frac{m}{\hbar t}\vec{r_{a,b}}. \tag{5.15}$$

Integrating eq. (5.15), gives the expression for the two phases,

$$\phi_{a,b} = \frac{m}{2\hbar t}(r \pm d)r + \phi, \tag{5.16}$$

with the integration constant being the initial relative phase. This then leads to

$$\phi_a - \phi_b = \frac{md}{\hbar t}r + \phi. \tag{5.17}$$

Using eq. (5.17) in eq. (5.14), reveals that the density modulations will depend on the initial separation of the condensates as well as the initial phase,

$$n = n_a + n_b + 2\sqrt{n_a n_b}\cos(\frac{md}{\hbar t}r + \phi). \tag{5.18}$$

The absolute position of the fringes depends only on the initial phase, making this a good mechanism to find that initial phase in an experiment, by using the resulting interference fringes. With the pattern of the fringes being $\cos(\frac{md}{\hbar t}r + \phi)$, the fringe spacing is then given by

$$\lambda = \frac{ht}{md}. \tag{5.19}$$

Unfortunately, the distance between the fragmented trapping potentials in this experiment is too large for the interference pattern to be visible. This poses an experimental problem, that would have to be solved by completely re-designing the imaging setup to get a closer look at this specific region of space. Some experiments have been carried out in which the cloud is held for long expansion times using magnetic levitation [85]. As this was not the primary aim of the work presented here, this experiment was not pursued further.

Chapter 6

Expansion of a low-dimensional condensate

This chapter is focussed on simulating the expansion of the Bose-Einstein condensate (BEC) after releasing the trapping potentials from an anisotropic magnetic trap. This will help validating the results obtained in the previous chapters, by making a direct comparison with the experimental results. To simulate the behaviour of the Bose gases, the Gross-Pitaevskii equation (GPE) will be introduced. Its solutions are found numerically using the Split-Step Fourier Method (SSFM), which is described in this section. The results of these simulations are then analysed and characterised, showing an excellent quantitative agreement with the experimental results.

The expansion speed can be extracted from the solutions of the GPE, as well as the aspect ratio. Arguably the best known characteristic of an anisotropic BEC is its change in aspect ratio when undergoing ballistic expansion. This change is analysed in this chapter, comparing full GPE simulations to the well-established Dalfovo theory and to our experiments. The theoretical results are compared side by side with the experimental data, giving a good picture of the agreement with the method developed and employed in this document. The limitations of these numerical solutions for the GPE are also discussed. A good selection of time steps, space steps and boundary conditions is crucial for acquiring accurate results, as explained in this chapter.

The GPE is developed using a two-dimensional model with rotational symmetry about one axis, corresponding to the lowest trapping frequency. In this way, the

model is effectively three-dimensional, saving the complex computational resources involved in the development of a fully three-dimensional model. Nevertheless, the three-dimensional simulation was also developed, and is presented in this chapter. An overview of the computational requirements is given, presenting ideas to accelerate the simulation process, and leading to a Matlab script that can be run from a standard laptop computer.

6.1 Gross-Pitaevskii Equation (GPE)

Assuming that thermal interactions are not present in a fully condensed cloud of particles, which is often the case for temperatures below the critical temperature (or transition temperature), the assumption of the gas being at zero temperature becomes accurate for modelling the system. The description of such a system would, ideally, be realised by representing the full many-body wavefunction of a system with N particles. Unfortunately, the complexity of this makes it non-viable. In a BEC, the inter-atomic interactions are weak, with the s-wave scattering length a_s being two orders of magnitude smaller than the de Broglie wavelength λ_{dB}. This is due to the weak forces between neutral atoms.

Assuming that the gas is at zero temperature, and the interactions between atoms in the BEC are weak, the Gross-Pitaevskii Equation (GPE) can be used to describe the system, with a macroscopic wavefunction

$$\psi(\vec{r},t) = \sqrt{n(\vec{r},t)}e^{iS(\vec{r},t)}. \tag{6.1}$$

The Gross-Pitaevskii Equation (GPE) was developed by Eugene P. Gross and Lev Petrovich Pitaevskii to describe superfluidity [113], and then applied to describe the behaviour of BECs [108]. It is a Nonlinear Schrödinger Equation (NLSE) in which the nonlinear term approximates inter-atomic interactions. Taking into account these interactions, the NLSE is

$$i\hbar\frac{\partial\psi(x,t)}{\partial t} = -\frac{\hbar^2}{2m}\frac{\partial^2\psi(x,t)}{\partial x^2} + \left[V(x) + g|\psi(x,t)|^2\right]\psi(x,t). \tag{6.2}$$

For interaction parameter $g < 0$, the interactions are attractive, and the condensate would collapse. For $g > 0$, as presented in this thesis, the interactions are

repulsive [114]. The dominant interactions are given by van der Waals elastic two-body interactions. For these interactions,

$$g = \frac{4\pi\hbar^2 a_S}{m}, \tag{6.3}$$

where a_s is the s-wave scattering length, which is specific for each element, being $a_s = 5.8 \cdot 10^{-9}$ m for ^{87}Rb [108, 114–117].

A full derivation of the GPE can be found in [36].

The NLSE is a Partial Differential Equation (PDE) derived from the well-known diffusion equation, with imaginary time [118, 119]. Considering the general form of such equations

$$A\psi_{xx} + B\psi_{xt} + C\psi_{tt} + D\psi_x + E\psi_t + F\psi = R(x,t), \tag{6.4}$$

B^2 is equal to $4AC$ and, therefore, the equation is Parabolic [120]. Although it is known that the equation is parabolic, an analytical solution is, in practice, not usually obtainable. Therefore, the solution of this equation must be obtained numerically. There are different solving methods for the GPE [114]. In this document, the Split-Step Fourier Method (SSFM) [121] is applied. The reason for choosing this method over others, like Runge-Kutta or Crank-Nicolson, is its efficiency when it comes to computational resources. Some groups have developed an alternative method using the Projected Gross-Pitaevskii Equation (PGPE) [122, 123]. Although the PGPE describes the behaviour of a Bose gas in a relatively accurate way, it neglects the highest energy modes of the sample.

6.1.1 Condensates in anisotropic harmonic potentials

In the experimental setup, the BEC is trapped in a harmonic magnetic potential. This confinement overcomes the inter-particle interactions. The shape of this potential will determine the shape of the condensate. Typically, a BEC can be found with a *spherical* shape ($\omega_x \approx \omega_y \approx \omega_z$), a *pancake* shape ($\omega_x > \omega_y, \omega_z$), or a *cigar* shape ($\omega_z, \omega_y > \omega_x$). In the case of $\omega_z, \omega_y \gg \omega_x$ and $\hbar(\omega_z\omega_y)^{1/2} \gg \mu$, excitations of the BEC are suppressed in the radial direction and only present in the axial direction, which makes an effective one-dimensional condensate. In this

case, the condensate can be described using a one-dimensional Gross-Pitaevskii Equation (1D GPE).

6.1.1.1 Weakly interacting regime

When $|\frac{Na_s}{l_r}| < 1$, where the harmonic oscillator length is defined as $l_i = \sqrt{\hbar/m\omega_i}$, the condensate can be considered to be in the weakly interacting regime. There is a macroscopic occupation of the ground state of the system, which has an approximately Gaussian form. This is often referred to as the ideal gas condensate.

The effective interaction strengths for a 1D GPE and a 2D GPE are given by [114]

$$g_{1D} = \frac{g}{2\pi l_z l_y}, \tag{6.5}$$

and

$$g_{2D} = \frac{g}{\sqrt{2\pi} l_x}. \tag{6.6}$$

The chemical potential of the systems are then

$$\mu_{1D} = \mu - \frac{\hbar\omega_z}{2} - \frac{\hbar\omega_y}{2}, \tag{6.7}$$

and

$$\mu_{2D} = \mu - \frac{\hbar\omega_x}{2}. \tag{6.8}$$

6.1.1.2 Thomas-Fermi approximation

When $|\frac{Na_s}{l_r}| \gg 1$, or $\mu \gg \hbar(\omega_z\omega_y)^{1/2}$, the interaction strength starts to grow. The particle distribution loses its characteristic Gaussian shape, widening in the middle and acquiring an inverted parabolic shape, which mirrors that of the harmonic trap. In this regime, the kinetic energy term $\nabla^2\psi$ can be neglected. This is known as the Thomas-Fermi approximation and has a density profile given by

$$n(x,y,z) = \begin{cases} \frac{\mu}{g}\left(1 - \frac{x^2}{R_x^2} - \frac{y^2}{R_y^2} - \frac{z^2}{R_z^2}\right), & \text{inside ellipsoid,} \\ 0, & \text{elsewhere.} \end{cases} \tag{6.9}$$

This approximation is used in the modelling of the expansion of the BEC and leads to a very good comparison with the experimental results obtained in the atom chip setup (section 6.3).

6.2 Split-Step Fourier Method (SSFM)

The Split-Step Fourier Method was originally proposed in 1973 by American physicist Frederick Tappert [124] and has, since then, been used across a wide range of applied sciences, including waves and acoustic propagation. In the case of a BEC, it is based on splitting the GPE into the linear and the nonlinear part [125], and analysing them independently. To get a good idea of how this method works, the next few lines describe the procedure in the one-dimensional case. Starting from a one-dimensional NLSE

$$i\hbar\frac{\partial\psi(x,t)}{\partial t} = \hat{H}\,\psi(x,t) = \hat{T}\,\psi(x,t) + \hat{V}\,\psi(x,t), \tag{6.10}$$

taking into account the interactions, as in eq. (6.2), there is an exact solution of the form

$$\psi(x,t+\Delta t) = e^{-\frac{i}{\hbar}\Delta t\hat{H}}\psi(x,t). \tag{6.11}$$

The equation is split into the nonlinear part $i\psi_t = -|\psi|^2\psi$ and the linear part $i\psi_t = -\frac{1}{2}\psi_{xx}$. In this way, the solutions to the potential energy operator $\hat{V}$ can be found directly in position space, and the solutions to the kinetic energy operator $\hat{T}$ can be found with the Fourier transform since $\hat{T}$ is diagonal in k-space, but not in position space. This can be done using the first order Lie-Trotter splitting [126, 127]

$$\psi(x,t+\Delta t) \approx e^{-\frac{i}{\hbar}\Delta t\hat{T}}e^{-\frac{i}{\hbar}\Delta t\hat{V}}\psi(x,t), \tag{6.12}$$

or the second order Strang splitting [127, 128]

$$\psi(x, t + \Delta t) \approx e^{-\frac{i}{2\hbar}\Delta t\hat{V}} e^{-\frac{i}{\hbar}\Delta t\hat{T}} e^{-\frac{i}{2\hbar}\Delta t\hat{V}} \psi(x, t). \tag{6.13}$$

The method developed by Strang is implemented in this simulation, since it has been proved by various groups to give a smaller error for large number of steps [129–131]. Higher order splitting methods would be possible and could lead to better accuracy. However, the implementation of these would require additional complexity and, for diffusion equations, it can introduce issues with stability [132, 133]. Therefore, the Strang splitting method provides a good compromise between accuracy and complexity.

Using the Fourier transform $\mathscr{F}$ to solve $\hat{T}$ in reciprocal space,

$$\psi(x, t + \Delta t) \approx e^{-\frac{i}{2\hbar}(V(x)+g|\psi|^2)\Delta t}\, \mathscr{F}^{-1}\left[e^{-\frac{i\hbar k^2}{2m}\Delta t}\, \mathscr{F}\left[e^{-\frac{i}{2\hbar}(V(x)+g|\psi|^2)\Delta t}\psi(x, t)\right]\right]. \tag{6.14}$$

When no interactions are taken into account, the initial wave function has a Gaussian profile. For the case of weak interactions, when $|Na_s/l_r| < 1$, the initial wave function is also Gaussian of the form

$$\psi_0 = \sqrt{\frac{N}{l_x}} \left(\frac{1}{\pi}\right)^{1/4} e^{-\frac{x^2}{2l_x^2}}, \tag{6.15}$$

for the 1D case [114]. For the 2D case

$$\psi_0 = \sqrt{\frac{N}{\pi(l_x^2 + l_y^2)}}\, e^{-\frac{x^2+y^2}{2(l_x^2+l_y^2)}}. \tag{6.16}$$

In this document, the SSFM is implemented using Matlab. The reason for using Matlab over Python for this particular simulation is that Matlab computes the discrete Fourier transform more efficiently and faster. Given the fine spatial grid and fine time steps needed, this proved to save about a third of the processing time. The problem is approached assuming that the condensate has a cigar

shape, presenting a rotational symmetry around the axial direction. Given this assumption, the y and z variation of the trap potential can be characterised by the same frequency and will therefore show the same expansion, in contrast with the x variation, which has a much lower frequency and will show a slower expansion.

The first step is to define a 2D meshgrid given by $x = [-M\Delta x, M\Delta x]$ and $y = [-L\Delta y, L\Delta y]$, with M and L being the number of spatial steps and Δx and Δy the distance between adjacent grid points. The whole script works using Cartesian coordinates, assuming that the expansion in y and z are equal. The wavefunction is then evolved over N_t time steps, of fixed internal Δt, using eq. (6.14). In which k is the Fourier transform parameter, or wave number, given by $k_x = [-M\Delta k_x, M\Delta k_x]$ and $k_y = [-L\Delta k_y, L\Delta k_y]$, where $\Delta k_x = \pi/(M\Delta x)$ and $\Delta k_y = \pi/(L\Delta y)$. This method has been implemented, both in Matlab and Python, using the pseudo code algorithm 1.

Algorithm 1 Split-Step Fourier Method pseudo code

$\psi_0 \rightarrow \psi$
for $n = 1$ to N_t **do**
  $\psi = \psi \exp\left[-\frac{i\Delta t}{2\hbar}\left(V(x) + g|\psi(x,t)|^2\right)\right]$
  $\psi_k = \mathscr{F}\left[\psi\right]$
  $\psi_k = \psi_k \exp\left[-\frac{i\Delta t\hbar}{2m}k^2\right]$
  $\psi = \mathscr{F}^{-1}\left[\psi_k\right]$
  $\psi = \psi \exp\left[-\frac{i\Delta t}{2\hbar}\left(V(x) + g|\psi(x,t)|^2\right)\right]$
end for
Return ψ

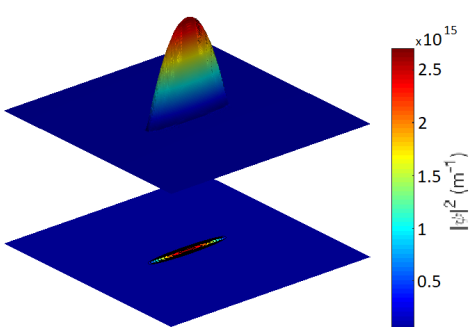
Special care has to be taken when choosing the time step size, as a large time step would result in an inaccurate approximation to our problem, and a too small time step would incur in unreasonable computing times. The time step chosen was 10^{-6}. The local error in the Strang splitting method decays as Δt^3 [114, 132]. The global error is given by the local error multiplied by the number of steps $N_t = t/\Delta t$, meaning that the method is second order accurate. Similarly, for the spatial step-size, a balance between accuracy in the result and computational time has to be found [134].

The SSFM for the 3D is implemented in this case assuming rotational symmetry around the x axis, effectively reducing the system to 2D. The initial wavefunction is defined using the Thomas-Fermi approximation described in section 6.1.1.2, in an anisotropic potential, with $\omega_z, \omega_y > \omega_x$. The ground state of the system and its chemical potential can be introduced analytically or by evolving a NLSE in

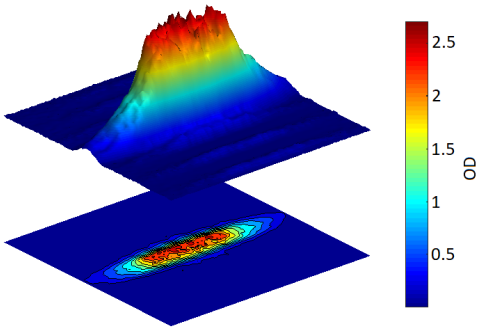
imaginary time, starting with a Gaussian density distribution. Excitations of the ground state often result in corrugations of the density distribution of the system, with the formation of solitons and vortices [41, 42].

Figure 6.1 shows the qualitative results of the SSFM method along with the experimental results, for comparison. The wavefunction is evolved over different times-of-flight, setting the trapping potential to zero everywhere, in order to simulate simple ballistic expansion following switch off of the trap. In the left hand column, figs. 6.1a, 6.1c and 6.1e show a 3D surface plot of $|\psi(t_{TOF})|^2$ over its xy plane contour projection. The colour scale of the plot is normalised for better visualisation. In the right hand column, figs. 6.1b, 6.1d and 6.1f show a 3D surface plot of the Optical Density extracted from the experiment using absorption imaging, and plotted over its xy plane contour projection. The x and y scales are equal in the left and right hand columns. In both the experimental and the SSFM cases, the condensate atom number was 10^5, with an axial trapping frequency of $2\pi \cdot 20\,\text{Hz}$ and a radial trapping frequency of $2\pi \cdot 1000\,\text{Hz}$.

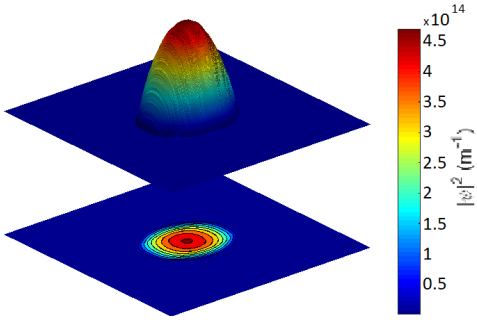
The experimental results are for a non-pure BEC, averaged over three sets of data. This averaged BEC profile contained density modulations arising from in-trap phase fluctuations (see section 4.2), explaining the origin of the "noise" in the axial direction. The fluctuations in the atom density in the radial direction (or gravity direction) are due to an imaging artefact, specifically optical diffraction generated by light reflecting from the surface of the atom chip. The condensate fraction of these results is $\approx 40\,\%$, leading to a Gaussian shaped thermal atom cloud surrounding a condensed part of parabolic form. This is the reason why for short times-of-flight, the experimental results have a larger atom density than for the SSFM counterpart. For longer times-of-flight, the thermal part expands much faster than the condensate, having very little presence in the region of the image, therefore showing a much closer result to the SSFM simulation. The effect of gravity is clearly identifiable, especially in fig. 6.1f, showing the Gaussian thermal distribution skewed in the direction of gravity (blue region skewed towards the plane of the paper). This is due to collision forces dominating over the gravitational force in the high-density condensate part of the atom cloud, compared to the low-density thermal cloud, in which the force of gravity dominates.



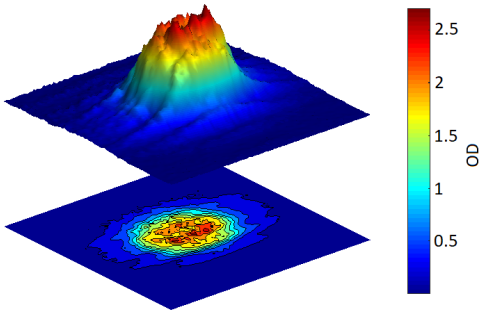
(a) GPE modelling $t_{TOF} = 1\,\text{ms}$



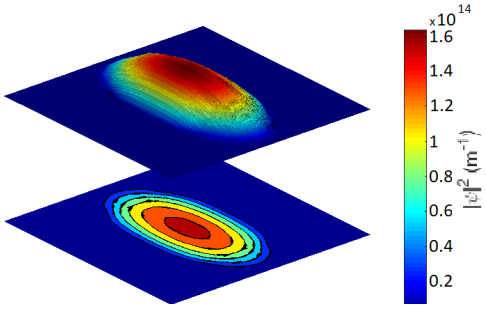
(b) Experiment $t_{TOF} = 1\,\text{ms}$



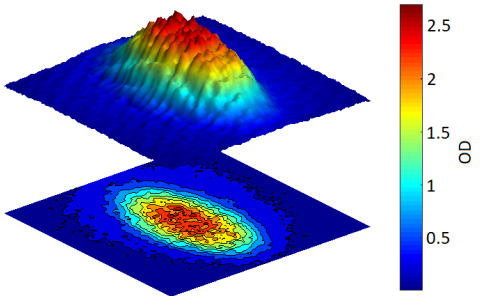
(c) GPE modelling $t_{TOF} = 5\,\text{ms}$



(d) Experiment $t_{TOF} = 5\,\text{ms}$



(e) GPE modelling $t_{TOF} = 13\,\text{ms}$



(f) Experiment $t_{TOF} = 13\,\text{ms}$

FIGURE 6.1: Simulation [(a),(c),(e)] of the expansion of a BEC compared to the experimental data [(b),(d),(f)] for the same conditions and for ballistic expansion times of $t_{TOF} = 1\,\text{ms}$ [(a),(b)], $t_{TOF} = 5\,\text{ms}$ [(c),(d)], and $t_{TOF} = 13\,\text{ms}$ [(e),(f)]. Each panel shows a 3D surface of $|\psi(t = t_{TOF})|^2$, or Optical Density (OD) in the experimental case, and its 2D contour projection underneath. Number of atoms in the BEC $N = 10^5$, radial trapping frequency $\omega_r = 2\pi \cdot 1000\,\text{Hz}$, and the axial trapping frequency $\omega_a = 2\pi \cdot 20\,\text{Hz}$. Figure size is 600×600 μm. The simulated expansion dynamics were obtained using the Split-Step Fourier Method (SSFM) for a two-dimensional Gross-Pitaevskii Equation (GPE) assuming rotational symmetry around the x axis. The measurements were made using the experimental setup described in chapter 3, following release of the BEC from the atom chip trap, and averaging over three data sets. The colour scale is normalised in both cases for clearer visualisation, and the x and y scales are equal in all figures.

Overall, the performance of the SSFM script is very good, being capable of accurately predicting any experimental procedure performed on the BEC, with easy tuning of the initial conditions. For experiments with short time-of-flight measurements and corresponding fewer simulation time steps required, the processing speed increases dramatically. These results are further analysed in the next section, which provides more detailed description and characterisation beyond the 3D surface and the 2D contour visualisation plots shown in fig. 6.1.

6.3 Expansion of a low-dimensional condensate

As explained in section 3.8.1, experiments on cold atoms can be visualised by imaging the system immediately after the experiment is performed. In this setup, images are taken after 1 ms to avoid residual magnetic fields affecting the detuning needed for imaging. Additionally, for certain experiments, longer ballistic expansion times are needed. Therefore, a full understanding of the expansion of a condensate is essential in order to extract information from the system by using absorption imaging.

6.3.1 Expansion speed

The expansion speed of a cloud of atoms at low-temperatures is determined by many different factors. The trapping frequency (section 3.7.2) is determined by the magnetic potentials generated for a specific trap configuration. This explains the aspect ratio inversion seen in a cigar-shape BEC undergoing free expansion (see fig. 6.3), where the trapping frequency in the radial direction is much larger than in the axial direction, delivering a much faster expansion speed in the radial direction once the trap is released. The vibrational excitation of the particles is directly related to the temperature of the atom cloud, meaning that a larger temperature produces a faster expansion speed. Inter-atomic interactions also play an important role, and are different for different species of atoms, due to factors like the scattering length (see section 6.1).

Figure 6.2 shows how a three-dimensional elongated condensate expands once the trapping potential is released. The condensate atom number was $N = 10^5$, with an axial trapping frequency of $2\pi \cdot 20\,\text{Hz}$ and a radial trapping frequency

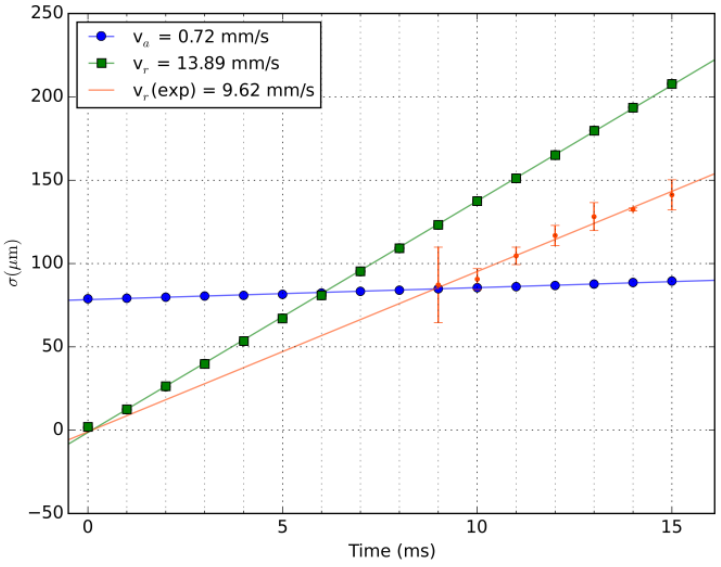


FIGURE 6.2: Evolution of the size of the condensate during time-of-flight for the 2D GPE SSFM simulations (blue circles and green squares show axial and radial expansion, respectively) and the experimental data (orange dots with errorbar show radial expansion). Lines show the fit to the plotted data. The radial and axial expansion speeds depend on the initial trapping potentials, which strong anisotropy produces the much faster expansion speed in the tightly-confined radial direction. The experimental data show a slower expansion speed compared to the 2D GPE.

of $2\pi \cdot 1000\,\mathrm{Hz}$. Solving the GPE numerically via the SSFM method shows an expansion speed in the radial direction of approximately 14 mm/s, whereas in the axial direction the expansion speed is $< 1\,\mathrm{mm/s}$. Simulation results are plotted in fig. 6.2 together with the experimentally measured radial expansion speed for the same initial system. The aspect ratio flip characteristic of an expanding elongated condensate is clearly seen here, and will be addressed in the next section.

Interestingly, the radial expansion speed extracted from the experimental data (orange line in fig. 6.2) is lower than predicted with the GPE simulations (green line in fig. 6.2). The experimental condensate fraction in this case is of $\approx 40\,\%$, meaning that the BEC is surrounded by a non-condensed thermal cloud of atoms. When the trap is released, the atoms in the thermal cloud expand in all directions, effectively "pushing" outwards as well as inwards, thus opposing the free expansion of the condensed part.

6.3.2 Aspect ratio

To analyse the evolution of the aspect ratio, the Split-Step Fourier Method results were compared with corresponding experimental data, and to the derivation made by Franco Dalfovo in the late 90s [37, 135], which is the most common theoretical model followed for predicting the expansion of a BEC.

For a large number of atoms in trap, the Gross-Pitaevskii Equation (eq. (6.2)) can be reduced to the atom density continuity equation

$$\frac{\delta}{\delta t}n + \nabla(\mathbf{v}n) = 0, \tag{6.17}$$

and to the Euler equation for the velocity field:

$$m\frac{\delta}{\delta t}\mathbf{v} + \nabla\left(V_{ext} + gn + \frac{mv^2}{2}\right) = 0, \tag{6.18}$$

where the external potential is $V_{ext} = \frac{m}{2}\sum_i \omega_i^2 r_i^2$.

Taking the Thomas-Fermi ground state atom density profile

$$n(\mathbf{r}) = g^{-1}[\mu - V_{ext}], \tag{6.19}$$

the solutions to eq. (6.17) have the density profile

$$n(x,y,z,t) = \begin{cases} a_0(t) - a_x(t)x^2 - a_y(t)y^2 - a_z(t)z^2, & n(x,y,z,t) > 0, \\ 0, & n(x,y,z,t) \leqslant 0 \end{cases}, \tag{6.20}$$

and a velocity field, from eq. (6.18), of the form

$$\mathbf{v}(x,y,z,t) = \frac{1}{2}\nabla[\alpha_x(t)x^2 + \alpha_y(t)y^2 + \alpha_z(t)z^2]. \tag{6.21}$$

Knowing that

$$\mathbf{v}(x,y,z,t) = \frac{\hbar}{m}\nabla S(x,y,z,t), \tag{6.22}$$

the phase is given by

$$S(x,y,z,t) = \frac{m}{2\hbar}[\alpha_x(t)x^2 + \alpha_y(t)y^2 + \alpha_z(t)z^2]. \tag{6.23}$$

The parabolic shape of the density (eq. (6.20)) remains, with the radii scaling as

$$R_i(t) = \sqrt{\frac{2\mu}{m\omega_{0i}^2}}b_i(t), \tag{6.24}$$

where

$$a_i = \frac{m\omega_{0i}^2}{2gb_xb_yb_zb_i^2}, \tag{6.25}$$

$$a_0 = -\left(\frac{15N}{8\pi}\right)^{2/5}(a_xa_ya_z)^{1/5}. \tag{6.26}$$

From the density and velocity field, the following equations can be derived [100]

$$\alpha_i = \frac{\dot{b}_i}{b_i}, \tag{6.27}$$

$$\ddot{b}_i + \omega_i^2 b_i - \frac{\omega_{0i}^2}{b_ib_xb_yb_z} = 0. \tag{6.28}$$

For an anisotropic trap, much as the one described in this chapter, eqs. (6.27) and (6.28) can be solved to give

$$\frac{d^2}{d(\omega_{y,z})^2}b_{y,z} = \frac{1}{b_{y,z}^3b_x}, \tag{6.29}$$

$$\frac{d^2}{d(\omega_{y,z})^2}b_x = \frac{\left(\frac{\omega_x}{\omega_{y,z}}\right)}{b_{y,z}^2b_x^2}. \tag{6.30}$$

These differential equations can be solved analytically, giving the ratio of expansion in both the axial and radial directions of the trap;

$$b_{y,z}(\omega_{y,z}t) = \sqrt{1 + (\omega_{y,z}t)^2}, \tag{6.31}$$

$$b_x(\omega_{y,z}t) = 1 + \left(\frac{\omega_x}{\omega_{y,z}}\right)^2 \left[(\omega_{y,z}t)\arctan(\omega_{y,z}t) - \log\sqrt{1 + (\omega_{y,z}t)^2}\right], \tag{6.32}$$

where the aspect ratio of the expanding cloud is $\frac{\omega_x b_{y,z}}{\omega_{y,z} b_x}$.

Figure 6.3 shows the evolution in time of the aspect ratio calculated from the 2D GPE SSFM solutions, the experimental data, and the expansion rate predicted by the analytical eqs. (6.31) and (6.32). The experimental data is taken as the average over three sets with a condensate atom number of $N \approx 10^5$, an axial trapping frequency of $2\pi \cdot 20\,\text{Hz}$ and a radial trapping frequency of $2\pi \cdot 1000\,\text{Hz}$. These same parameters were used for the two theoretical plots in fig. 6.3. The expansion of the surrounding thermal cloud opposes the expansion of the condensate in both the radial and axial directions, thus the aspect ratio evolution is independent of the condensate fraction.

It is important to note that the experimental values of the aspect ratio for $t_{TOF} \geqslant 5\,\text{ms}$ were taken by fitting the Thomas-Fermi atom density distribution and extracting the Thomas-Fermi radius, whereas the values for $t_{TOF} \leqslant 3\,\text{ms}$ were taken from the Half-Width Half-Maximum (HWHM) of a Gaussian fit due to the condensed and thermal clouds not being clearly distinguishable at this point. As a result, the data measured for shorter time-of-flight values agree slightly worse with the SSFM results than those at late times. The missing points in the experimental dataset (orange dots in fig. 6.3) are due to imaging artefacts affecting the quality of the image. The reflection of the light from the surface of the atom chip leads to diffraction lines that alter the optical density imaged by the CCD camera sensor. These diffraction lines can be avoided by tilting the imaging beam for different time-of-flight measurements, since it shifts the position of the lines [1].

[1] Due to the laboratory being moved to a different institution, further data acquisition was not possible.

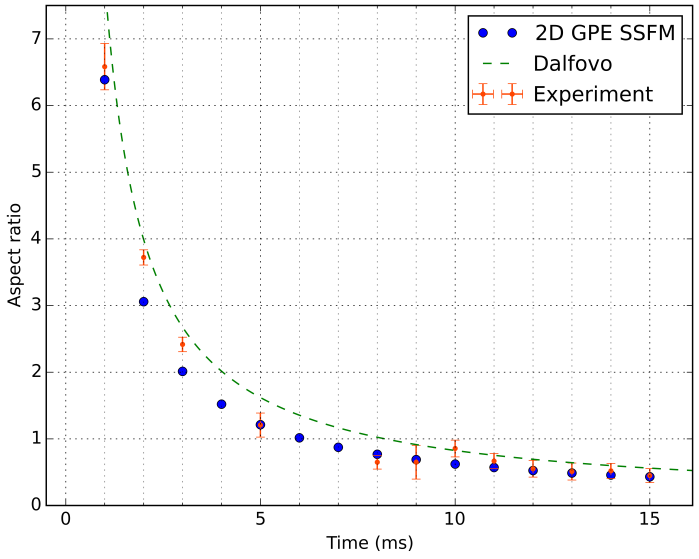


FIGURE 6.3: Evolution of the aspect ratio of the condensate during time-of-flight expansion. Results from the 2D GPE SSFM are shown by blue circles. Experimental data are shown in orange, with the errorbars arising from the standard error of the three different sets taken. The green dashed line corresponds to the Dalfovo derivation [108]. The condensate atom number is $N = 10^5$, with an axial trapping frequency of $2\pi \cdot 20\,\text{Hz}$ and a radial trapping frequency of $2\pi \cdot 1000\,\text{Hz}$. There is good agreement between all three datasets, with the experimental results suggesting that the 2D GPE SSFM is slightly more precise.

The agreement between the 2D GPE SSFM and the experiment is very good, with almost all of the theoretical points in fig. 6.3 lying within the experimental error. The qualitative and quantitative agreement with the Dalfovo derivation is also very good. The 2D GPE SSFM predicts a flip in the aspect ratio at $t_{TOF} \approx 6\,\text{ms}$, and the Dalfovo theory at $t_{TOF} \approx 8\,\text{ms}$. Comparison with the experimental data suggests that the 2D GPE gives better accuracy than the widely used analytical eqs. (6.31) and (6.32). These results show the potential of this 2D GPE SSFM as a modelling tool, not only for pure BECs, but also for cold atomic clouds with a non-condensed part.

Further to the work presented in this thesis, quantum reflection and breathing modes have also been simulated by the author using this GPE tool, proving its accuracy and extensive capabilities.

So far, the SSFM has shown results that are consistent with experiment qualitatively and quantitatively. Another interesting check for the expansion simulation is to reduce the size of the spatial grid used in the simulations, effectively forcing the

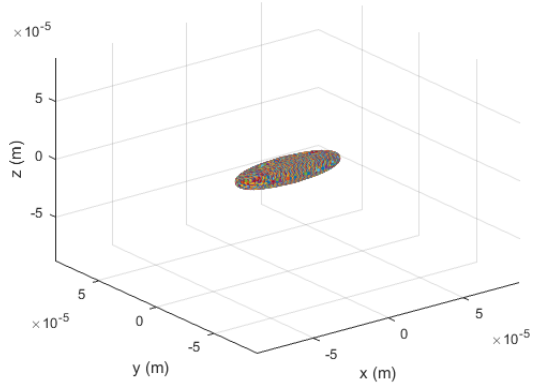
wavefunction to hit the grid boundaries, which act as infinite potential barriers, while expanding and so generating a reflecting wave and associated interference.

Several improvements to the processing efficiency were developed, leading to a final overall processing time of under 40 hours for the whole expansion modelling. The same code was also developed to work with Python, resulting in an increase of the processing time of about 10 %, due to the management of the Fourier transform process. If developing a 3D GPE SSFM script in the same way, for a system without rotational symmetry, the processing time would be very difficult to handle. A faster version of the script could be realised by coding and compiling the actual SSFM part in C language.

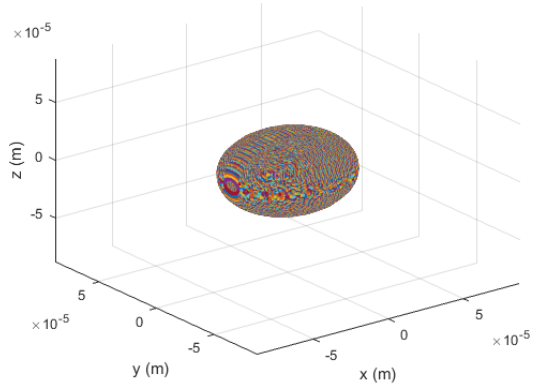
6.3.3 Three-dimensional modelling

The evolution of computing in the last two decades has been revolutionary. However, there are still plenty of limitations arising from computing resources. The vast majority of the work presented in this chapter was carried out using a two-dimensional implementation of the Split-Step Fourier Method. The symmetric character encountered in typical trapping geometries gives, in this case, a rotational symmetry along the axial axis of the trap. For a Z-wire trap, this is true as long as the temperature is small compared with the depth of the trapping potential well. In this situation, there is a lower axial frequency and two higher radial frequencies that can be described as one radial frequency with rotational symmetry. This allows for good understanding of the behaviour of the condensate, and a reasonable computational speed. Nevertheless, this work was extended to full three-dimensional modelling, i.e. with no axis of symmetry assumed, in which different shapes and configurations of traps are allowed, making it an ideal toolbox for any type of experiment in any possible configuration.

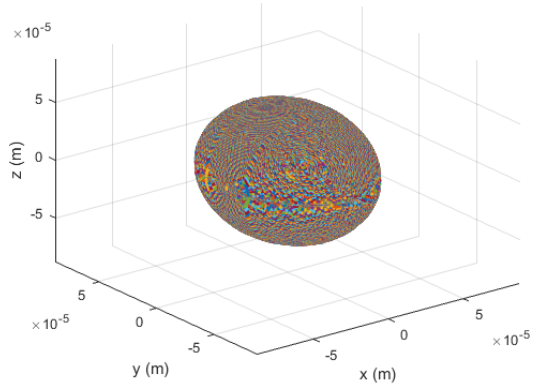
Figure 6.4 shows the simulated expansion of a condensate with atom number $N = 10^5$, an axial trapping frequency of $2\pi \cdot 20$ Hz and a radial trapping frequency of $2\pi \cdot 100$ Hz, with ballistic expansion times of 1 ms, 8 ms, and 15 ms. The evolution in time is clear, with the condensate expanding faster in the more confined radial direction than in the weaker axial direction.



(a) $t_{TOF} = 1\,\text{ms}$



(b) $t_{TOF} = 8\,\text{ms}$



(c) $t_{TOF} = 15\,\text{ms}$

FIGURE 6.4: Isodensity surfaces showing the expansion of a BEC, simulated using the Split-Step Fourier Method (SSFM) for a three-dimensional Gross-Pitaevskii Equation for ballistic expansion times of (a) 1 ms, (b) 8 ms, and (c) 15 ms. Isodensity surfaces plotting values $> 1/30$ of maximum. Speckle pattern is an artefact of the visualisation, with no physical significance.

The full set of data, with ballistic expansion times ranging from 1 ms to 15 ms, is compared to the commonly used theory of expansion developed by Dalfovo [37]. This is shown in fig. 6.5, which compares the evolution of the aspect ratio found in simulation and experiment and shows good agreement between the two.

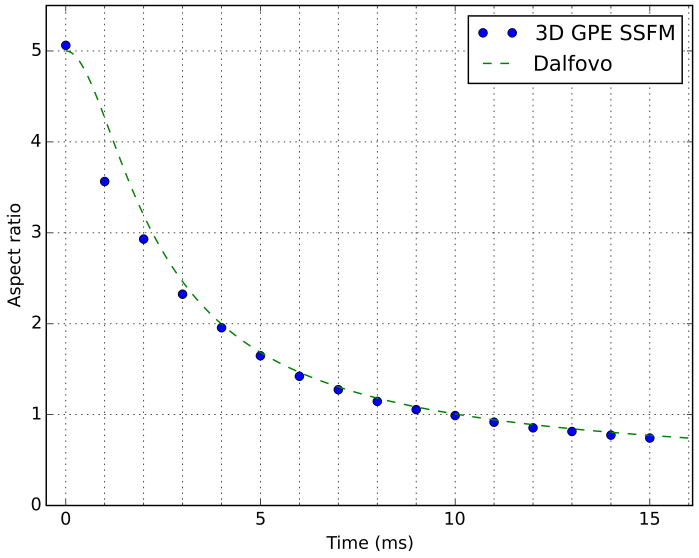


FIGURE 6.5: Aspect ratio of the condensate calculated versus time-of-flight using full three-dimensional GPE modelling. Results from the 3D GPE SSFM are represented by blue circles. The green dashed line corresponds to the Dalfovo derivation [108]. In both cases, the condensate atom number is $N = 10^5$, with an axial trapping frequency of $2\pi \cdot 20\,\text{Hz}$ and a radial trapping frequency of $2\pi \cdot 100\,\text{Hz}$. Good agreement can be seen between both theoretical datasets.

For constructing the figures from the evolved wavefunction, the density distribution matrix is interrogated step by step, plotting only the values that are above a certain probability threshold. Computing resource is a limiting factor, especially on the graphics side. Perhaps, the most interesting and relevant way to visualise the results is through isodensity surface plot of the atom density, which determine the overall size of the system. This enables the whole process to be run from a standard laptop computer, with running times comparable to the previously described 2D GPE SSFM script.

Chapter 7

Emerging Quantum Technology components

In the last decade, a lot of interest has been focussed on the use of quantum physics outside the laboratory environment. In 2013, the UK government announced an investment of £270m in quantum technologies, in which the University of Nottingham is active through partnership in the UK Quantum Technologies Hub for sensors and metrology. The aim of this funding is to convert quantum physics research into commercial products.

From a gravity sensor, to a rotation sensor, to a magnetic field sensor, the potential of quantum physics devices is huge due to their high sensitivity. These devices can improve the sensitivity of measurements by several orders of magnitude compared to present sensors. The application range is vast, including examples like a gravity sensor used to precisely image underground structures, or a rotation sensor used as an inertial navigation system.

Great progress has already been realised within the Quantum Technologies programme, with some example demonstrators already leaving the laboratory environment. However, there is still a long way to go before achieving fully compact and portable devices.

In the following sections, a brief description of devices and applications outside the laboratory environment is exposed. A portable 9 V coil system and a Magnetic Induction Tomography experiment are also described, showing the potential for

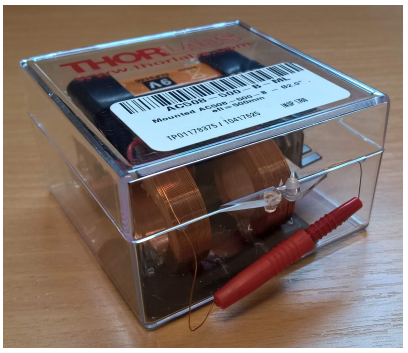
improved magnetic field generation systems. Finally, a "dual-colour" scheme for improving atom number in the MOT is explained and experimental results shown.

7.1 Optimisation of magnetic field generation

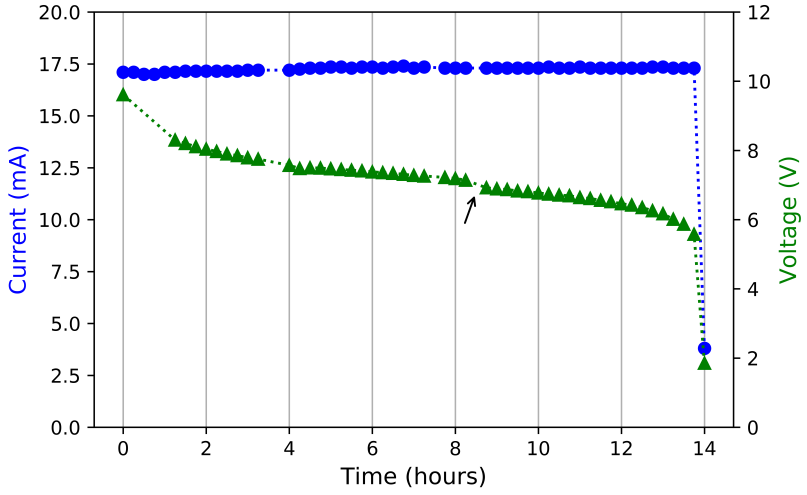
When doing research in a very conceptually and technologically complex setup, such as a cold atoms setup, it is easy to forget the foundations of these systems. The production of a MOT is a very robust process. Large variations in parameters such as background pressure, laser frequency or magnetic field potentials, will affect the MOT but will not necessarily stop it working completely. For this reason, magnetic fields are usually generated by large rudimentary home-built coils, designed for ease of construction and mounting on the setup. This often results in coils that overheat, and so need to be water cooled, consume large amounts of power, needing an industrial three phase power socket, and generate far from optimum magnetic potentials. Prof. Mark Fromhold and Dr. Nathan Welch have been developing optimisation codes to find the best magnetic field configuration for a specific purpose. Most of the time, this configuration relies on multiple coils, for which they have also developed an optimisation tool. With the help of a coil winding machine and the electronics workshop, these coils have been manufactured in-house. The fields have also been measured experimentally, validating the theoretical predictions, and showing great improvements in power consumption and field fidelity.

7.1.1 Battery powered magneto-optical trap

The optimisation of magnetic fields was realised experimentally by the construction of a compact coil system capable of producing the magnetic field gradients necessary for trapping and cooling ^{87}Rb atoms. The two coils were designed by Dr. Nathan Welch and manufactured by Mr. Ian Taylor, with a resistance of 183.5 Ω and an inductance of 9.25 mH each. The coils are powered by a commercial off-the-shelf 9 V battery. The whole setup fits inside a small lens box, $65 \times 65 \times 40$ mm in size (see fig. 7.1a). To ensure a constant magnetic field, a current regulator circuit was designed, built and added to the setup. This circuit is based around a LM317 3-terminal adjustable regulator, drawing 3 V. The result is a MOT coil



(a) Compact coil system for a MOT housed in a standard 2" Thorlabs lens box.



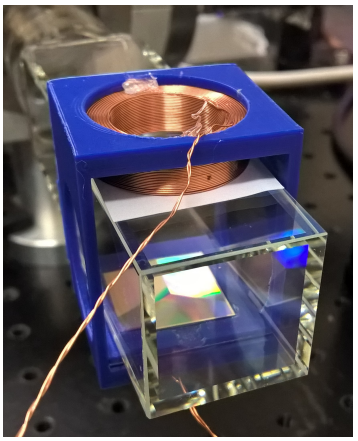
(b) Current through coils and battery output voltage measured versus time for a 9 V PP3 battery.

FIGURE 7.1: Compact and portable coil system (a) capable of generating the magnetic field gradients necessary to trap and cool ^{87}Rb atoms, driven by an off-the-shelf 9 V PP3 battery for a period of 14 hours. The setup is housed in a standard 2" Thorlabs lens box. The graph in (b) shows the measured stability of the coil current (blue circles) and battery output voltage (green triangles) throughout the 14 hours.

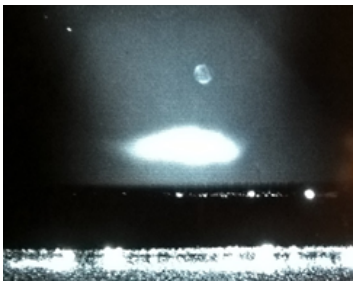
system driven by a single 9 V battery for a period of 14 hours non-stop, as shown in fig. 7.1b.

To prove the portability, the system was transported home in a backpack during this working time, showing a small bump in the data (arrowed in fig. 7.1b) due to a change in the measuring device.

Additionally, a second iteration of this system was developed to be integrated in a grating MOT (GMOT) experiment, based at the University of Strathclyde, in



(a) Coil setup.



(b) MOT picture.

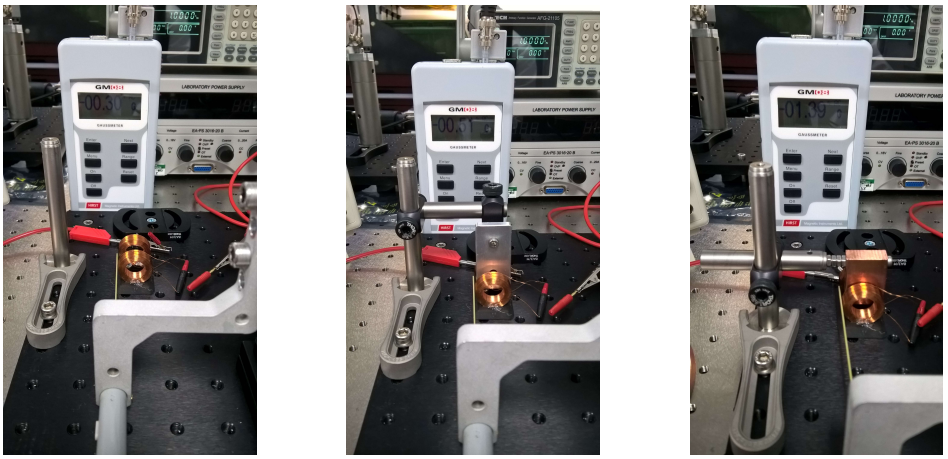
FIGURE 7.2: Optimised asymmetric coil system developed for the University of Strathclyde to generate a MOT with a single MOT beam reflecting from a grating, using only battery powered coils. The coils are housed in a 3D printed mount (blue) designed specifically for this setup.

the group of Prof. Erling Riis, Dr. Aidan Arnold and Dr. Paul Griffin [136, 137]. An asymmetric coil configuration was developed in order to fit around a glass cell, greatly reducing the overall size of the system, while keeping a low power consumption. A few days were spent at the University of Strathclyde, working on creating a MOT using these coils, powered from a 9 V battery. Figure 7.2 shows the system, with a 3D printed mount, containing the coils and grating. Up to 2×10^6 atoms were trapped using a single beam and generating the necessary magnetic fields using an off-the-shelf standard battery. To the author's knowledge, this constitutes the first ever MOT generated with coils driven from a standard battery.

These systems are a first step, on the magnetic fields side, towards a compact and portable quantum technologies device, and prove that there is still plenty of room for optimisation regarding magnetic field generation.

7.1.2 Magnetic Induction Tomography (MIT)

The ability to accurately control the production of magnetic fields, opens up new prospects for both classical and quantum physics. An important branch of contemporary research is imaging. From imaging imperfections in engineering products, to imaging the brain, the spectrum of areas is vast. The possibility of finding



(a) Empty space (b) Aluminium plate (c) Copper plate

FIGURE 7.3: Basic MIT experiment to show how different conductivities can be extracted from measured Eddy currents induced in different samples.

the structure of mechanical systems depends on how well these systems can be analysed. Security has also become an important issue in the 21^{st} century.

Some preliminary research on Magnetic Induction Tomography (MIT) was carried out. The concept of MIT is based on inducing Eddy currents in a metallic object by placing the object inside a well characterised magnetic field. These Eddy currents will then induce a magnetic field that can be measured with external pick-up coils. Measuring the magnetic field generated by the object requires being able to distinguish between the initial magnetic field and the one generated by the Eddy currents in the conductor. A way to solve this problem is to apply an AC magnetic field [138]. In this way, the Eddy current will induce a change in the amplitude and a phase shift in the measured signal. Different materials interact differently with the magnetic fields, leading to the ability to calculate the spatial conductivity variation of such materials and, therefore, being able to predict the material that is inside the interrogation area. This method is of great interest because it is non-invasive, unlike X-ray scanners, and can provide information about the location and type of material.

An experiment to demonstrate this effect was built using the coils described in the previous section. The coils are connected in an anti-Helmholtz configuration to a signal generator delivering a 1 kHz sinusoidal signal. A signal amplifier was connected in between to increase the current output of the system. The setup is shown in fig. 7.3, showing the RMS magnetic field measured using a Gaussmeter that is connected to a Hall probe.

The measured magnetic field will result from the addition of the applied magnetic field and the magnetic field generated by the Eddy currents,

$$|B| = \sqrt{|B_{applied}|^2 + |B_{Eddy}|^2}, \tag{7.1}$$

with $|B_{applied}| = 0.3\,\mathrm{G}$. Therefore, the magnetic field produced by the Eddy current is 0.412 G for the Aluminium plate and 0.687 G for the Copper plate. As the Eddy current scales with the resistivity of the material, it can be seen that the ratio of the two fields, 1.667, is within 10 % of the ratio of the two resistivities for Copper ($1.68 \times 10^{-4}\,\Omega\,\mathrm{m}$) and Aluminium ($2.65 \times 10^{-4}\,\Omega\,\mathrm{m}$).

This is a very simple, yet powerful, experiment that shows the potential of MIT technology to image objects in a non invasive way. As well as showing how there is still room for optimisation and improvement of magnetic field generation.

7.2 Optimisation of the MOT with a dual-colour scheme

For trapping and cooling atoms, there are three main areas to tackle, magnetic field generation, ultra-high vacuum and laser systems. With magnetic field generation being more and more developed with optimised coils, and background pressure being reduced with the implementation of pre-cooling devices such as the 2D MOT described in section 3.4, the last thing to look at is laser systems. There has been a lot of work in different groups trying to miniaturise these systems, as well as trying to enhance the trapping capabilities of a device. One way of increasing the atom number in trap is to use a "dual-colour MOT".

At the beginning of the work presented in this thesis, some time was spent developing a laser system scheme to improve the size of the atomic cloud in the magneto-optical trap stage. This scheme is based on using two different laser cooling frequencies [139, 140]. As seen in section 2.1, a usual cold atoms setup includes one cooling frequency, red-detuned by some factor δ from the cooling transition. The dual-colour MOT proposal involves using two different cooling frequencies, one detuned positively by δ_{dc} from this δ value and the other one detuned negatively by a frequency shift δ_{dc}, giving it the name of "dual-colour" due

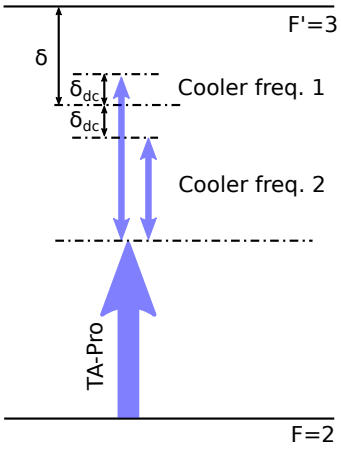


FIGURE 7.4: Level scheme for a dual-colour MOT in ^{87}Rb, with a two-frequency detuning cooling system, where δ_{dc} is the frequency shift.

to the positive and negative detunings from the optimal single frequency detuning. Experimentally, this scheme was implemented in two different ways to ensure that no experimental artefact was influencing the data. One implementation was using two different AOMs to modulate the frequencies. The other setup used a single AOM coupled to an RF frequency combiner, effectively driving the single AOM with the two frequencies at the same time. Results in both cases were similar, with small differences in atom number values, arising from technical differences between the two setups. Figure 7.4 shows the schematics of the laser frequencies used. Figure 7.5 is the resulting atom number measured versus the frequency shift δ_{dc}. It is very clear that an almost threefold improvement in the atom number arises with frequency shifts of $\delta_{dc} \approx 2\,\text{MHz}$, with an initial detuning of $\delta = -3\Gamma$. These results were obtained by averaging over four sets of data.

The density and characteristic Gaussian shape of the cloud were distorted during this procedure, so an additional MOT stage of a few milliseconds was implemented at the end to re-shape the cloud of atoms. This additional stage was enough to re-shape the cloud of atoms and increase its density while still preserving a twofold improvement in the atom number compared to a single frequency scheme.

This scheme has been the object of study for some groups for a few decades. At present, and to the knowledge of the author, no reliable explanation for this effect has been yet presented. Nevertheless, it can be a useful setup for experiments that require larger atom number in the magneto-optical trap stage. Moreover, some experiments require larger atom numbers with low density of atoms, like in the case of an atomic fountain [141], for which the setup could be extremely useful.

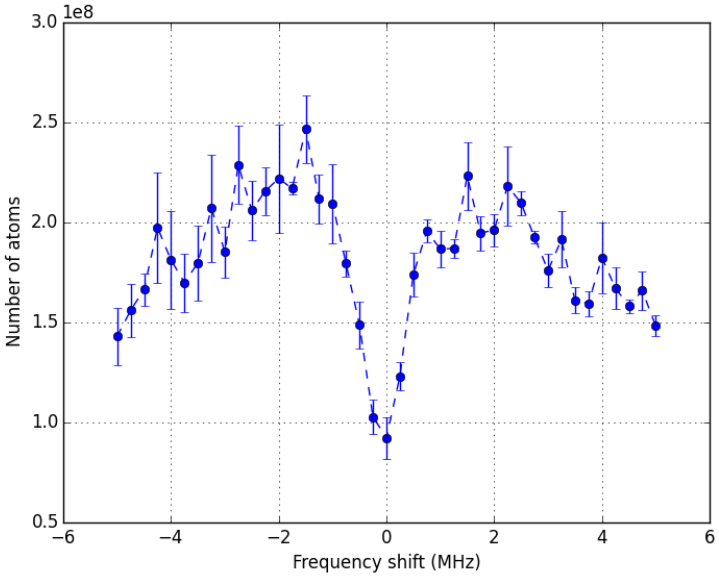


FIGURE 7.5: Atom number measured for different δ_{dc} shifts. An increase in atom number was measured for a frequency shift $\delta_{dc} \approx 2\,\text{MHz}$ in a dual-colour MOT configuration. An increase of up to three times can be achieved by using two cooling frequencies.

Due to the tight trapping potentials of the atom chip, it was not necessary to use a dual-colour MOT for the setup presented in this document. However, for quantum technologies out of the lab, the technique may be advantageous.

7.3 Conclusions and Outlook

This thesis has attempted to describe and explain some of the physics of low-dimensional Bose-Einstein condensates, both theoretically and experimentally, based on the work developed in the atom chip experiment described in chapter 3. Throughout, the advantages and limitations of this type of setup have been discussed together with the attempts to overcome these limitations.

The work carried out in the laboratory (chapter 4) shows the potential of atom chip based experiments both for low-temperature physics research, e.g. quenching dynamics (section 4.1) and phase fluctuations (section 4.2), and for applications outside the laboratory, e.g. BEC microscopy (section 4.3). Interesting physical effects were seen and analysed, helping to elucidate the physics of low-temperature Bose gases. Technical details of the experiment have been also presented, e.g.

showing the great improvement experienced by the addition of a 2D MOT that uses permanent magnets to generate the trapping potentials, described in section 3.4.

Some of the limitations that arose from this laboratory based work were developed and explained theoretically in chapter 5, especially the demonstration that imperfections at a nanometre scale were shown to have a large effect on the cold atomic cloud of Bose gas, presenting possible ways to solve the issues encountered in the experiments. This work can be of use for future development of atom chips. Graphene is currently set to revolutionise the state-of-the-art in atom chips. This new research promises to produce single layer conducting paths with reduced resistance and fewer imperfections. The development of these will definitely mark a significant improvement in the capabilities of experiments such as those described in this thesis.

Theoretical work was also developed to find numerical solutions for the non-linear Schrödinger equation in chapter 6. The Split-Step Fourier Method was chosen due to its reliable results. The expansion of Bose gases was presented, attempting to understand and explain the experimental results obtained, as well as the limitations encountered in the simulations, such as reflection of matter waves from the simulation grid boundaries. The results were compared in section 6.3 to previous analytical work done by F. Dalfovo, S. Stringari and L. Pitaevskii [135], amongst others, and also with data obtained from the laboratory, showing very good quantitative agreement.

As with every other experiment, there is always room for improvement, from improving the cycle times, to increasing the atom number, to reducing noise levels. A multi-condensate experiment was proposed in section 5.3, taking advantage of the fragmentation induced by imperfections on the atom chip, and using it to generate multiple experiments per cycle, considerably reducing experimental times. In section 3.4, the 2D MOT was shown to greatly accelerate the loading of the magneto-optical trap, as well as remove any background pressure effects that can considerably disturb the condensation of the Bose gas.

Bibliography

[1] S. N. Bose. *Plancks gesetz und lichtquantenhypothese*. Springer, 1924.

[2] A. Einstein. *Quantentheorie des einatomigen idealen Gases*. Akademie der Wissenshaften, in Kommission bei W. de Gruyter, 1924.

[3] K. C. Wali. Einstein and Bose. In *APS April Meeting Abstracts*, 2005.

[4] G. Bian, D. Vigil, H. Hu, M. Oz, S. Zhou, S. Hong, Z. Wang, B. Hsu, C. C. Z. Zamalloa, and D. Lyon. Realization of Bose–Einstein condensation in dilute gases. *Citeseer*, 2008.

[5] M. H. Anderson, J. R. Ensher, M. R. Matthews, C. E. Wieman, and E. A. Cornell. Observation of Bose–Einstein condensation in a dilute atomic vapor. *Science*, 269(5221):198–201, 1995.

[6] K. B. Davis, M.-O. Mewes, M. R. Andrews, N. Van Druten, D. Durfee, D. Kurn, and W. Ketterle. Bose–Einstein condensation in a gas of sodium atoms. *Physical Review Letters*, 75(22):3969, 1995.

[7] E. A. Cornell and C. E. Wieman. Nobel lecture: Bose–Einstein condensation in a dilute gas, the first 70 years and some recent experiments. *Reviews of Modern Physics*, 74(3):875, 2002.

[8] C. Cohen-Tannoudji and D. Guéry-Odelin. *Advances in atomic physics: An overview*. World Scientific, 2011.

[9] M. Zhan, K. Li, P. Wang, L. Kong, X. Wang, R. Li, X. Tu, L. He, J. Wang, and B. Lu. Cold atom interferometry. In *Journal of Physics: Conference Series*, volume 80, page 012047. IOP Publishing, 2007.

[10] A. Peters, K. Y. Chung, and S. Chu. High-precision gravity measurements using atom interferometry. *Metrologia*, 38(1):25, 2001.

[11] A. D. Cronin, J. Schmiedmayer, and D. E. Pritchard. Optics and interferometry with atoms and molecules. *Reviews of Modern Physics*, 81(3):1051, 2009.

[12] T. Schumm, S. Hofferberth, L. M. Andersson, S. Wildermuth, S. Groth, I. Bar-Joseph, J. Schmiedmayer, and P. Krüger. Matter-wave interferometry in a double well on an atom chip. *Nature Physics*, 1(1):57, 2005.

[13] C. Cohen-Tannoudji. Forces exercées par des photons sur des atomes. *Cours au College de France*, 1983, 1982.

[14] E. Raab, M. Prentiss, A. Cable, S. Chu, and D. E. Pritchard. Trapping of neutral sodium atoms with radiation pressure. *Physical Review Letters*, 59 (23):2631, 1987.

[15] C. J. Foot. *Atomic physics*, volume 7. Oxford University Press, 2005.

[16] H. J. Metcalf and P. Van der Straten. *Laser cooling and trapping*. Springer Science & Business Media, 2012.

[17] C. Cohen-Tannoudji. Piégeage non dissipatif et refroidissement évaporatif. *Cours au Collège de France*, 86:87, 1996.

[18] J. Dalibard and C. Cohen-Tannoudji. Laser cooling below the doppler limit by polarization gradients: simple theoretical models. *JOSA B*, 6(11):2023–2045, 1989.

[19] P. D. Lett, R. N. Watts, C. I. Westbrook, W. D. Phillips, P. L. Gould, and H. J. Metcalf. Observation of atoms laser cooled below the doppler limit. *Physical Review Letters*, 61(2):169, 1988.

[20] M. Inguscio and L. Fallani. *Atomic physics: precise measurements and ultracold matter*. OUP Oxford, 2013.

[21] A. Moerdijk, H. Boesten, and B. Verhaar. Decay of trapped ultracold alkali atoms by recombination. *Physical Review A*, 53(2):916, 1996.

[22] A. Frisch, K. Aikawa, M. Mark, F. Ferlaino, E. Berseneva, and S. Kotochigova. Hyperfine structure of laser-cooling transitions in fermionic erbium-167. *Physical Review A*, 88(3):032508, 2013.

[23] Z. Min, C. Ning, Z. Xiao-Hang, H. Liang-Yu, Y. Mao-Fei, T. Jie, G. Qi, J. Hai-Ling, T. Hai-Yao, and X. Xin-Ye. Experiments on trapping ytterbium atoms in optical lattices. *Chinese Physics B*, 22(10):103701, 2013.

[24] L. De Broglie. *Recherches sur la théorie des quanta*. PhD thesis, Migration-université en cours d'affectation, 1924.

[25] J. Reichel and V. Vuletic. *Atom chips*. John Wiley & Sons, 2011.

[26] S. Groth, P. Krüger, S. Wildermuth, R. Folman, T. Fernholz, J. Schmiedmayer, D. Mahalu, and I. Bar-Joseph. Atom chips: Fabrication and thermal properties. *Applied Physics Letters*, 85(14):2980–2982, 2004.

[27] Y. Zhou, N. Welch, R. Crawford, F. Oručević, F. Wang, P. Krüger, R. Wildman, C. Tuck, and T. M. Fromhold. Design of magneto-optical traps for additive manufacture by 3d printing. *arXiv preprint arXiv:1704.00430*, 2017.

[28] R. Saint, W. Evans, Y. Zhou, T. Barrett, T. Fromhold, E. Saleh, I. Maskery, C. Tuck, R. Wildman, F. Oručević, et al. 3d-printed components for quantum devices. *Scientific reports*, 8(1):8368, 2018.

[29] W. Ketterle and N. Van Druten. Evaporative cooling of trapped atoms. In *Advances in atomic, molecular, and optical physics*, volume 37, pages 181–236. Elsevier, 1996.

[30] G. Aviv. *Dynamic manipulations of interacting 1D Bose gases*. PhD thesis, University of Nottingham, 2014.

[31] A. Piccardo-Selg. *Cold atom sources for portable quantum sensors*. PhD thesis, University of Nottingham, 2013.

[32] T. J. Barrett. *An apparatus for the production of Bose–Einstein condensates in tunable geometries on a chip*. PhD thesis, University of Nottingham, 2017.

[33] J. Ferreras and M. Corrigan. Design and assembly of a source of atoms at a few hundred microkelvin. M.Sci. thesis, 2014.

[34] D. Hellweg, S. Dettmer, P. Ryytty, J. Arlt, W. Ertmer, K. Sengstock, D. Petrov, G. Shlyapnikov, H. Kreutzmann, and L. Santos. Phase fluctuations in Bose–Einstein condensates. *Applied Physics B: Lasers and Optics*, 73(8):781–789, 2001.

[35] G. Sinuco-León, B. Kaczmarek, P. Krüger, and T. Fromhold. Atom chips with two-dimensional electron gases: Theory of near-surface trapping and ultracold-atom microscopy of quantum electronic systems. *Physical Review A*, 83(2):021401, 2011.

[36] L. Pitaevskii and S. Stringari. *Bose–Einstein condensation and superfluidity*, volume 164. Oxford University Press, 2016.

[37] F. Dalfovo, C. Minniti, and L. Pitaevskii. Frequency shift and mode coupling in the nonlinear dynamics of a Bose-condensed gas. *Physical Review A*, 56 (6):4855, 1997.

[38] Y. Castin and R. Dum. Bose–Einstein condensates in time dependent traps. *Physical Review Letters*, 77(27):5315, 1996.

[39] V. Ménoret, R. Geiger, G. Stern, P. Cheinet, B. Battelier, N. Zahzam, F. P. Dos Santos, A. Bresson, A. Landragin, and P. Bouyer. A transportable cold atom inertial sensor for space applications. In *International Conference on Space Optics—ICSO 2010*, volume 10565, page 1056530. International Society for Optics and Photonics, 2017.

[40] H. Griffiths. Magnetic induction tomography. *Measurement science and technology*, 12(8):1126, 2001.

[41] T. Billam, A. Marchant, S. Cornish, S. Gardiner, and N. Parker. Bright solitary matter waves: formation, stability and interactions. In *Spontaneous Symmetry Breaking, Self-Trapping, and Josephson Oscillations*, pages 403–455. Springer, 2012.

[42] K. E. Strecker, G. B. Partridge, A. G. Truscott, and R. G. Hulet. Formation and propagation of matter-wave soliton trains. *Nature*, 417(6885):150, 2002.

[43] R. Scott, A. Martin, T. Fromhold, and F. Sheard. Anomalous quantum reflection of Bose–Einstein condensates from a silicon surface: the role of dynamical excitations. *Physical Review Letters*, 95(7):073201, 2005.

[44] H. F. Hess. Evaporative cooling of magnetically trapped and compressed spin-polarized hydrogen. *Physical Review B*, 34(5):3476, 1986.

[45] H. F. Hess, G. P. Kochanski, J. M. Doyle, N. Masuhara, D. Kleppner, and T. J. Greytak. Magnetic trapping of spin-polarized atomic hydrogen. *Physical Review Letters*, 59(6):672, 1987.

[46] C. S. Adams, H. J. Lee, N. Davidson, M. Kasevich, and S. Chu. Evaporative cooling in a crossed dipole trap. *Physical Review Letters*, 74(18):3577, 1995.

[47] S. Chu. Nobel lecture: The manipulation of neutral particles. *Reviews of Modern Physics*, 70(3):685, 1998.

[48] C. N. Cohen-Tannoudji. Manipulating atoms with photons. *Physics, 1996-2000*, 1996:166, 2002.

[49] W. D. Phillips. Laser cooling and trapping of neutral atoms. *Rev. Mod. Phys*, 70(3):721, 1998.

[50] J.-F. Clément. *Réalisation d'un condensat de Bose–Einstein dans un piège dipolaire optique à 1565 nm.* PhD thesis, Université Paris Sud-Paris XI, 2008.

[51] W. Petrich, M. H. Anderson, J. R. Ensher, and E. A. Cornell. Stable, tightly confining magnetic trap for evaporative cooling of neutral atoms. *Physical Review Letters*, 74(17):3352, 1995.

[52] D.-J. Han. Bose–Einstein condensation of rubidium-87 atoms in a magnetic trap. 1998.

[53] A. Arnold. *Preparation and Manipulation of an" 8" 7Rb Bose-Einstein Condensate.* PhD thesis, Citeseer, 1999.

[54] C. Cohen-Tannoudji. Piégeage non dissipatif et refroidissement évaporatif, 1996-1997. *Cours du College de France, disponible sur http://www. phys. ens. fr/cours/collegede-france/index. html.*

[55] O. Luiten, M. Reynolds, and J. Walraven. Kinetic theory of the evaporative cooling of a trapped gas. *Physical Review A*, 53(1):381, 1996.

[56] V. Bagnato, D. E. Pritchard, and D. Kleppner. Bose-einstein condensation in an external potential. *Physical Review A*, 35(10):4354, 1987.

[57] E. A. Cornell and C. E. Wieman. Nobel lecture: Bose–Einstein condensation in a dilute gas: the first 70 years and some recent experiments. In *Collected Papers Of Carl Wieman*, pages 626–644. World Scientific, 2008.

[58] W. Ketterle. Nobel lecture: When atoms behave as waves: Bose–Einstein condensation and the atom laser. *Reviews of Modern Physics*, 74(4):1131, 2002.

[59] C. J. Pethick and H. Smith. *Bose–Einstein condensation in dilute gases*. Cambridge university press, 2002.

[60] G. Cook and R. Dickerson. Understanding the chemical potential. *American Journal of Physics*, 63(8):737–742, 1995.

[61] M. Naraschewski and D. Stamper-Kurn. Analytical description of a trapped semi-ideal Bose gas at finite temperature. *Physical Review A*, 58(3):2423, 1998.

[62] A. P. Mandoki. *A single apparatus for the production of ultracold fermionic lithium and cold bosonic caesium gases*. PhD thesis, University of Nottingham, 2015.

[63] M. D. Jones. *Preparation of cold samples of caesium-133 and lithium-6 in a single apparatus for Bose-Fermi mixtures experiments*. PhD thesis, University of Nottingham, 2014.

[64] D. A. Steck. Rubidium 87 d line data, 2001.

[65] W. Demtröder. *Laser spectroscopy: basic concepts and instrumentation*. Springer Science & Business Media, 2013.

[66] D. W. Preston. Doppler-free saturated absorption: Laser spectroscopy. *American Journal of Physics*, 64(11):1432–1436, 1996.

[67] J. Appel, A. MacRae, and A. Lvovsky. A versatile digital GHz phase lock for external cavity diode lasers. *Measurement Science and Technology*, 20 (5):055302, 2009.

[68] H. Busche. *Efficient loading of a magneto-optical trap for experiments with dense ultracold Rydberg gases*. PhD thesis, Diploma thesis, University of Heidelberg, 2011.

[69] B. Höltkemeier. *2D MOT as a source of a cold atom target*. PhD thesis, Diploma thesis, Ruprecht-Karls-Universtät Heidelberg, 2011.

[70] J. Arlt, O. Marago, S. Webster, S. Hopkins, and C. Foot. A pyramidal magneto-optical trap as a source of slow atoms. *Optics communications*, 157 (1):303–309, 1998.

[71] A. Ridinger, S. Chaudhuri, T. Salez, U. Eismann, D. R. Fernandes, K. Magalhaes, D. Wilkowski, C. Salomon, and F. Chevy. Large atom number dual-species magneto-optical trap for fermionic 6 Li and 40 K atoms. *The European Physical Journal D-Atomic, Molecular, Optical and Plasma Physics*, 65(1):223–242, 2011.

[72] A. Paris-Mandoki, M. D. Jones, J. Nute, J. Wu, S. Warriar, and L. Hackermüller. Versatile cold atom source for multi-species experiments. *Review of Scientific Instruments*, 85(11):113103, 2014.

[73] Y. B. Ovchinnikov. A permanent Zeeman slower for Sr atomic clock. *The European Physical Journal Special Topics*, 163(1):95–100, 2008.

[74] E. Riis, D. S. Weiss, K. A. Moler, and S. Chu. Atom funnel for the production of a slow, high-density atomic beam. *Physical Review Letters*, 64(14):1658, 1990.

[75] J. Schoser, A. Batär, R. Löw, V. Schweikhard, A. Grabowski, Y. B. Ovchinnikov, and T. Pfau. Intense source of cold Rb atoms from a pure two-dimensional magneto-optical trap. *Physical Review A*, 66(2):023410, 2002.

[76] C. Utfeld. *Aufbau einer Hochleistungsquelle für ultrakalte Atome, Johannes Gutenberg-Universität Mainz*. PhD thesis, Diplomarbeit, 2006 86 Literaturverzeichnis, 2006.

[77] H. Busche, S. W. Ball, and P. Huillery. A high repetition rate experimental setup for quantum non-linear optics with cold Rydberg atoms. *The European Physical Journal Special Topics*, 225(15-16):2839–2861, 2016.

[78] K. Dieckmann, R. Spreeuw, M. Weidemüller, and J. Walraven. Two-dimensional magneto-optical trap as a source of slow atoms. *Physical Review A*, 58(5):3891, 1998.

[79] J. Reichel, W. Hänsel, and T. Hänsch. Atomic micromanipulation with magnetic surface traps. *Physical Review Letters*, 83(17):3398, 1999.

[80] S. Chu and C. Wieman. Laser cooling and trapping of atoms: introduction. *JOSA B*, 6(11):2020–2022, 1989.

[81] G. Reinaudi, T. Lahaye, Z. Wang, and D. Guéry-Odelin. Strong saturation absorption imaging of dense clouds of ultracold atoms. *Optics letters*, 32 (21):3143–3145, 2007.

[82] T. M. Brzozowski, M. Maczynska, M. Zawada, J. Zachorowski, and W. Gawlik. Time-of-flight measurement of the temperature of cold atoms for short trap-probe beam distances. *Journal of Optics B: Quantum and Semiclassical Optics*, 4(1):62, 2002.

[83] D. Petrov, D. Gangardt, and G. Shlyapnikov. Low-dimensional trapped gases. In *Journal de Physique IV (Proceedings)*, volume 116, pages 5–44. EDP Sciences, 2004.

[84] E. Hinds, C. Vale, and M. Boshier. Two-wire waveguide and interferometer for cold atoms. *Physical Review Letters*, 86(8):1462, 2001.

[85] M. E. Zawadzki, P. Griffin, E. Riis, and A. Arnold. Spatial interference from well-separated split condensates. *Physical Review A*, 81(4):043608, 2010.

[86] B. Fang, G. Carleo, A. Johnson, and I. Bouchoule. Quench-induced breathing mode of one-dimensional Bose gases. *Physical Review Letters*, 113(3): 035301, 2014.

[87] S. Hofferberth, I. Lesanovsky, B. Fischer, T. Schumm, and J. Schmiedmayer. Non-equilibrium coherence dynamics in one-dimensional Bose gases. *Nature*, 449(7160):324, 2007.

[88] S. Dettmer, D. Hellweg, P. Ryytty, J. Arlt, W. Ertmer, K. Sengstock, D. Petrov, G. Shlyapnikov, H. Kreutzmann, and L. Santos. Observation of phase fluctuations in elongated Bose–Einstein condensates. *Physical Review Letters*, 87(16):160406, 2001.

[89] S. M. Barnett, S. Franke-Arnold, A. S. Arnold, and C. Baxter. Coherence length for a trapped bose gas. *Journal of Physics B: Atomic, Molecular and Optical Physics*, 33(19):4177, 2000.

[90] D. S. Petrov. *Bose–Einstein condensation in low-dimensional trapped gases*. PhD thesis, Universiteit van Amsterdam [Host], 2003.

[91] H. Kreutzmann, A. Sanpera, L. Santos, M. Lewenstein, D. Hellweg, L. Cacciapuoti, M. Kottke, T. Schulte, K. Sengstock, and J. Arlt. Characterization and control of phase fluctuations in elongated Bose–Einstein condensates. *Applied Physics B: Lasers and Optics*, 76(2):165–172, 2003.

[92] T. Juffmann, S. A. Koppell, B. B. Klopfer, C. Ophus, R. M. Glaeser, and M. A. Kasevich. Multi-pass transmission electron microscopy. *Scientific Reports*, 7(1):1699, 2017.

[93] M. Stecker, H. Schefzyk, J. Fortágh, and A. Günther. A high resolution ion microscope for cold atoms. *New Journal of Physics*, 19(4):043020, 2017.

[94] J. Fortágh and C. Zimmermann. Magnetic microtraps for ultracold atoms. *Reviews of Modern Physics*, 79(1):235, 2007.

[95] R. Folman, P. Treutlein, and J. Schmiedmayer. Atom chip. 2010.

[96] C. Koller. Towards the experimental realization of hybrid quantum systems. 2012.

[97] R. Salem, Y. Japha, J. Chabé, B. Hadad, M. Keil, K. Milton, and R. Folman. Nanowire atomchip traps for sub-micron atom–surface distances. *New Journal of Physics*, 12(2):023039, 2010.

[98] J.-B. Trebbia, C. G. Alzar, R. Cornelussen, C. I. Westbrook, and I. Bouchoule. Roughness suppression via rapid current modulation on an atom chip. *Physical Review Letters*, 98(26):263201, 2007.

[99] J. Esteve, C. Aussibal, T. Schumm, C. Figl, D. Mailly, I. Bouchoule, C. I. Westbrook, and A. Aspect. Role of wire imperfections in micromagnetic traps for atoms. *Physical Review A*, 70(4):043629, 2004.

[100] Y. Kagan, E. Surkov, and G. Shlyapnikov. Evolution of a Bose-condensed gas under variations of the confining potential. *Physical Review A*, 54(3): R1753, 1996.

[101] E. W. Weisstein. Rotation matrix. 2003.

[102] C. Ryu and M. G. Boshier. Integrated coherent matter wave circuits. *New Journal of Physics*, 17(9):092002, 2015.

[103] W. Hänsel, P. Hommelhoff, T. Hänsch, and J. Reichel. Bose–Einstein condensation on a microelectronic chip. *Nature*, 413(6855):498–501, 2001.

[104] S. Ghanbari, T. D. Kieu, A. Sidorov, and P. Hannaford. Permanent magnetic lattices for ultracold atoms and quantum degenerate gases. *Journal of Physics B: Atomic, Molecular and Optical Physics*, 39(4):847, 2006.

[105] R. Gerritsma, S. Whitlock, T. Fernholz, H. Schlatter, J. Luigjes, J.-U. Thiele, J. Goedkoop, and R. Spreeuw. Lattice of microtraps for ultracold atoms based on patterned magnetic films. *Physical Review A*, 76(3):033408, 2007.

[106] S. Zhou, D. Groswasser, M. Keil, Y. Japha, and R. Folman. Robust spatial coherence 5 μm from a room-temperature atom chip. *Physical Review A*, 93 (6):063615, 2016.

[107] M. Andrews, C. Townsend, H.-J. Miesner, D. Durfee, D. Kurn, and W. Ketterle. Observation of interference between two Bose condensates. *Science*, 275(5300):637–641, 1997.

[108] F. Dalfovo, S. Giorgini, L. P. Pitaevskii, and S. Stringari. Theory of Bose–Einstein condensation in trapped gases. *Reviews of Modern Physics*, 71(3): 463, 1999.

[109] W. Hoston and L. You. Interference of two condensates. *Physical Review A*, 53(6):4254, 1996.

[110] A. Röhrl, M. Naraschewski, A. Schenzle, and H. Wallis. Transition from phase locking to the interference of independent Bose condensates: Theory versus experiment. *Physical Review Letters*, 78(22):4143, 1997.

[111] G. Wallis and E. T. Rolls. Invariant face and object recognition in the visual system. *Progress in Neurobiology*, 51(2):167–194, 1997.

[112] F. Baumgartner. Measuring the acceleration of free fall with an atom chip BEC interferometer. 2011.

[113] V. Ginzburg and L. Pitaevskii. On the theory of superfluidity. *Sov. Phys. JETP*, 7(5):858–861, 1958.

[114] C. F. Barenghi and N. G. Parker. A primer on quantum fluids. *arXiv preprint arXiv:1605.09580*, 2016.

[115] H. Boesten, C. Tsai, J. Gardner, D. Heinzen, and B. Verhaar. Observation of a shape resonance in the collision of two cold Rb 87 atoms. *Physical Review A*, 55(1):636, 1997.

[116] D. Frese. *Bose–Einstein Condensation of Rubidium: Towards Ultracold Binary Bosonic Mixtures*. PhD thesis, Dissertation, Mathematisch-Naturwissenschaftlichen Fakultät der Rheinischen Friedrich-Wilhelms-Universität Bonn, 2005.

[117] M. Egorov, B. Opanchuk, P. Drummond, B. Hall, P. Hannaford, and A. Sidorov. Measurement of s-wave scattering lengths in a two-component Bose–Einstein condensate. *Physical Review A*, 87(5):053614, 2013.

[118] G. L. Garza and F. H. M. Ortiz. Ecuaciones diferenciales parciales. 2013.

[119] T. Okino. Correlation between diffusion equation and Schrödinger equation. 2013.

[120] K. F. Riley, M. P. Hobson, and S. J. Bence. *Mathematical methods for physics and engineering: a comprehensive guide*. Cambridge university press, 2006.

[121] P. U. Suárez. An introduction to the split step Fourier method using Matlab. 2013.

[122] M. Davis, S. Morgan, and K. Burnett. Simulations of Bose fields at finite temperature. *Physical Review Letters*, 87(16):160402, 2001.

[123] P. B. Blakie and M. J. Davis. Projected Gross–Pitaevskii equation for harmonically confined Bose gases at finite temperature. *Physical Review A*, 72 (6):063608, 2005.

[124] R. Hardin and F. Tappert. Applications of the split-step Fourier method to the numerical solution of nonlinear and variable coefficient wave equations. *Siam Rev*, 15(2):423, 1973.

[125] C. Bayındır. Early detection of rogue waves by the wavelet transforms. *Physics Letters A*, 380(1):156–161, 2016.

[126] H. F. Trotter. On the product of semi-groups of operators. *Proceedings of the American Mathematical Society*, 10(4):545–551, 1959.

[127] E. Faou, L. Gauckler, and C. Lubich. Plane wave stability of the split-step Fourier method for the nonlinear Schrödinger equation. In *Forum of Mathematics, Sigma*, volume 2, page e5. Cambridge Univ Press, 2014.

[128] G. Strang. On the construction and comparison of difference schemes. *SIAM Journal on Numerical Analysis*, 5(3):506–517, 1968.

[129] R. E. Omer, E. B. Bashier, and A. I. Arbab. Numerical solutions of a system of odes based on Lie–Trotter and Strang operator-splitting methods. 2017.

[130] D. Cohen and G. Dujardin. Exponential integrators for nonlinear Schrödinger equations with white noise dispersion. 2016.

[131] T. Jahnke and C. Lubich. Error bounds for exponential operator splittings. *BIT Numerical Mathematics*, 40(4):735–744, 2000.

[132] S. MacNamara and G. Strang. Operator splitting. In *Splitting Methods in Communication, Imaging, Science, and Engineering*, pages 95–114. Springer, 2016.

[133] J. Javanainen and J. Ruostekoski. Symbolic calculation in development of algorithms: split-step methods for the Gross–Pitaevskii equation. *Journal of Physics A: Mathematical and General*, 39(12):L179, 2006.

[134] B. R. Washburn. *Dispersion and nonlinearities associated with supercontinuum generation in microstructure fibers*. 2002.

[135] F. Dalfovo, C. Minniti, S. Stringari, and L. Pitaevskii. Nonlinear dynamics of a Bose condensed gas. *Physics Letters A*, 227(3):259–264, 1997.

[136] M. Vangeleyn, P. F. Griffin, E. Riis, and A. S. Arnold. Single-laser, one beam, tetrahedral magneto-optical trap. *Optics express*, 17(16):13601–13608, 2009.

[137] M. Vangeleyn, P. F. Griffin, E. Riis, and A. S. Arnold. Laser cooling with a single laser beam and a planar diffractor. *Optics letters*, 35(20):3453–3455, 2010.

[138] C. Deans, L. Marmugi, S. Hussain, and F. Renzoni. Electromagnetic induction imaging with a radio-frequency atomic magnetometer. *Applied Physics Letters*, 108(10):103503, 2016.

[139] C. Qiang, L. Xin-Yu, G. Kui-Yi, W. Xiao-Rui, C. Dong-Min, and W. Ru-Quan. Improved atom number with a dual color magneto–optical trap. *Chinese Physics B*, 21(4):043203, 2012.

[140] A. G. Sinclair, E. Riis, and M. J. Snadden. Improved trapping in a vapor-cell magneto-optical trap with multiple laser frequencies. *JOSA B*, 11(12): 2333–2339, 1994.

[141] R. Wynands and S. Weyers. Atomic fountain clocks. *Metrologia*, 42(3):S64, 2005.